SCHLIEREN IMAGING AND FLOW ANALYSIS ON A CONE/FLARE MODEL IN THE AFRL MACH 6 LUDWIEG TUBE FACILITY

THESIS

David A. LaBuda, Second Lieutenant, USAF

AFIT-ENY-MS-19-M-226

DEPARTMENT OF THE AIR FORCE
AIR UNIVERSITY

AIR FORCE INSTITUTE OF TECHNOLOGY

Wright-Patterson Air Force Base, Ohio

DISTRIBUTION STATEMENT A.
APPROVED FOR PUBLIC RELEASE; DISTRIBUTION UNLIMITED.

The views expressed in this thesis are those of the author and do not reflect the official policy or position of the United States Air Force, Department of Defense, or the United States Government. This material is declared a work of the U.S. Government and is not subject to copyright protection in the United States.

AFIT-ENY-MS-19-M-226

SCHLIEREN IMAGING AND FLOW ANALYSIS ON A CONE/FLARE MODEL IN THE AFRL MACH 6 LUDWIEG TUBE FACILITY

THESIS

Presented to the Faculty

Department of Aeronautics and Astronautics

Graduate School of Engineering and Management

Air Force Institute of Technology

Air University

Air Education and Training Command

In Partial Fulfillment of the Requirements for the

Degree of Master of Science in Aeronautical Engineering

David A. LaBuda, BS

Second Lieutenant, USAF

March 2019

DISTRIBUTION STATEMENT A.
APPROVED FOR PUBLIC RELEASE; DISTRIBUTION UNLIMITED.

AFIT-ENY-MS-19-M-226

SCHLIEREN IMAGING AND FLOW ANALYSIS ON A CONE/FLARE MODEL IN THE AFRL MACH 6 LUDWIEG TUBE FACILITY

THESIS

David A. LaBuda, BS
Second Lieutenant, USAF

Committee Membership:

Dr. M. F. Reeder
Chair

Dr. R. B. Greendyke
Member

Lt Col J. R. Komives, PhD
Member

AFIT-ENY-MS-19-M-226

Abstract

High-speed Schlieren photography was utilized to visualize flow in the Air Force Research Laboratory Mach 6 Ludwieg tube facility. A 7° half-angle cone/flare model with variable nosetip radius and flare angle options was used in the study. Testing was performed at two driver tube pressures, generating freestream Reynolds numbers of 10.0×10^6 and 19.8×10^6 per meter. The variable-angle flare portion of the model provided a method for adjusting the intensity of the adverse pressure gradient at the cone/flare junction. As expected from existing literature, boundary layer separation along the cone frustum occurred further upstream as the magnitude of the adverse pressure gradient increased. Imaging of the four cone tip radii revealed a slightly positive angle of attack for the model. This conclusion was supported by asymmetrical heating contours observed in a prior infrared thermography study on the same model. Measurements of the bow shock angles downstream of the cone tip verified Mach 6 flow from the Ludwieg tube nozzle when analyzed using Taylor-Maccoll theory. Blunt cone tips generated laminar boundary layers along the cone frustum. These laminar boundary layers led to unstable behavior in the recirculation region at the cone/flare junction. Analysis of the instability revealed loosely cyclical behavior. Pressure data from the model surface would provide much greater insight into local boundary layer behavior. Future hypersonic vehicles will inevitably include numerous adverse pressure gradients. A full understanding of these regions is imperative to successful design and flight testing.

Table of Contents

Page

Abstract iv
Table of Contents v
List of Figures vii
List of Tables xi
I. Introduction 1
General Issue 1
Problem Statement 3
Limitations 4
Preview 5
II. Literature Review 6
Chapter Overview 6
Hypersonic Background 6
Ludwieg Tube Background 10
Schlieren Background 12
Hypersonic Cone/Flare Research 13
Summary 21
III. Methodology 22
Chapter Overview 22
Ludwieg Tube Facility 22
High Speed Schlieren 32
Summary 39
IV. Analysis and Results 40
Chapter Overview 40

Tunnel Characterization 40

Cone/Flare Schlieren Results 49

Cone Tip Observations 52

Bow Shock Measurement 59

Shock/Boundary Layer Observations 63

Recirculation Region Measurements 74

Unsteady Shock Motion Measurements 83

Summary 89

V. Conclusions and Recommendations 90

Chapter Overview 90

Summary of Results 90

Significance of Research 92

Recommendations for Future Testing 93

Appendix 94

Bibliography 118

List of Figures

Page

Figure 1. Teflon Cones [14] 9

Figure 2. Shock tube operation [15] 11

Figure 3. Schlieren Diagram [17] 13

Figure 4. Turning Angle Effect on a 2-D Wedge of Varied Angle [22] 17

Figure 5. Boundary layer behavior with an adverse pressure gradient [26] 20

Figure 6. Compressors (left) and Vacuum Pumps (right) 23

Figure 7. Driver tube section 24

Figure 8. Test section room 26

Figure 9. Autoclave door with optical access 26

Figure 10. Vacuum tanks 27

Figure 11. Typical Pressure Trace 31

Figure 12. Light source, focusing lens, aperture, and 3-inch mirror 33

Figure 13. 6-inch and concave mirrors 33

Figure 14. Schlieren System Diagram (Not Drawn to Scale) 34

Figure 15. Cone/Flare Model Assembly (5.1mm Radius Tip, 40° Flare Shown) (dimensions in inches) 35

Figure 16. Cone/Flare Model Detail (5.1mm Radius Tip, 40° Flare Shown) (dimensions in inches) 36

Figure 17. Model positioned in test section (43° base and 10.2mm tip installed) 37

Figure 18. Pitot Rake Rendering 42

Figure 19. Mach Number Contour Plot (x=815mm) 43

Figure 20. Mach Number Measurements Across the Horizontal Sting Position (x=815mm) 44

Figure 21. Measurement Noise Across the Horizontal Sting Position (x=815mm) 45

Figure 22. Pressure Trace 47

Figure 23. Startup Schlieren (2ms time steps) 48

Figure 24. Horizontal Knife Edge Example 50

Figure 25. Vertical Knife Edge Example 50

Figure 26. Horizontal versus vertical knife edge on 43° base with 0.0mm tip. 51

Figure 27. Projected edges (0.0mm tip, 200psi) 55

Figure 28. Line Intensity Plot 55

Figure 29. Sharp tips (averaged) 56

Figure 30. Blunt tips (averaged) 57

Figure 31. Separation at cone tip (0.5ms time steps) 58

Figure 32. Bow Shock Location 60

Figure 33. Flare Angle Comparison (Averaged 0.0mm tip at 400psi) 65

Figure 34. 34° base, 400psi (averaged) 66

Figure 35. 34° base, 400psi (standard deviation) 67

Figure 36. 37° base, 400psi (averaged) 68

Figure 37. 37° base, 400psi (standard deviation) 69

Figure 38. 40° base, 400psi (averaged) 70

Figure 39. 40° base, 400psi (standard deviation) 71

Figure 40. 43° base, 400psi (averaged) 72

Figure 41. 43° base, 400psi (standard deviation) 73

Figure 42. Recirculation Region Measurement Process 75

Figure 43. Nosetip Radius vs. Separation/Reattachment Locations 79

Figure 44. Nosetip Radius vs. Separation Length..... 80

Figure 45. Comparison of Nosetip Radius vs. Separation/Reattachment Locations: Schlieren versus Infrared Thermography [26] 82

Figure 46. Boundary Layer Motion (10 Frame, 0.5ms Time Steps)..... 85

Figure 47. Pixel Area Example 86

Figure 48. Pixel Intensity Versus Frame Example (34° flare, 10.2mm radius tip) 87

Figure 49. FFT Example (34° flare, 10.2mm radius tip) 87

Figure 50. 34° base, 200psi (averaged)..... 94

Figure 51. 34° base, 200psi (standard deviation)..... 95

Figure 52. 37° base, 200psi (averaged)..... 96

Figure 53. 37° base, 200psi (standard deviation)..... 97

Figure 54. 40° base, 200psi (averaged)..... 98

Figure 55. 40° base, 200psi (standard deviation)..... 99

Figure 56. 43° base, 200psi (averaged)..... 100

Figure 57. 43° base, 200psi (standard deviation)..... 101

Figure 58. 34° base, 400psi (averaged), horizontal knife edge..... 102

Figure 59. 34° base, 400psi (standard deviation), horizontal knife edge..... 103

Figure 60. 37° base, 400psi (averaged), horizontal knife edge..... 104

Figure 61. 37° base, 400psi (standard deviation), horizontal knife edge..... 105

Figure 62. 40° base, 400psi (averaged), horizontal knife edge..... 106

Figure 63. 40° base, 400psi (standard deviation), horizontal knife edge..... 107

Figure 64. 43° base, 400psi (averaged), horizontal knife edge..... 108

Figure 65. 43° base, 400psi (standard deviation), horizontal knife edge..... 109

Figure 66. 34° base, 200psi (averaged), horizontal knife edge..... 110

Figure 67. 34° base, 200psi (standard deviation), horizontal knife edge..... 111

Figure 68. 37° base, 200psi (averaged), horizontal knife edge..... 112

Figure 69. 37° base, 200psi (standard deviation), horizontal knife edge..... 113

Figure 70. 40° base, 200psi (averaged), horizontal knife edge..... 114

Figure 71. 40° base, 200psi (standard deviation), horizontal knife edge..... 115

Figure 72. 43° base, 200psi (averaged), horizontal knife edge..... 116

Figure 73. 43° base, 200psi (standard deviation), horizontal knife edge..... 117

List of Tables

Page

Table 1. Test Conditions, Assuming Isentropic Flow 30

Table 2. Schlieren Test Equipment 39

Table 3. Upper Versus Lower Bow Shock Angles 54

Table 4. Bow Shock Angles 62

Table 5. Separation and Reattachment Points 78

Table 6. Blunt Tip Shock Motion 89

LIST OF ACRONYMS

AFRL	AIR FORCE RESEARCH LABORATORY
BAM6QT	BOEING/AFOSR MACH 6 QUIET TUNNEL
CFD	COMPUTATIONAL FLUID DYNAMICS
FFT	FAST FOURIER TRANSFORMATION
PFV	PHOTRON FASTCAM VIEWER
SBLI	SHOCK-WAVE/BOUNDARY-LAYER INTERACTION
TPS	THERMAL PROTECTION SYSTEM

SCHLIEREN IMAGING AND FLOW ANALYSIS ON A CONE/FLARE MODEL IN THE AFRL MACH 6 LUDWIEG TUBE FACILITY

I. Introduction

General Issue

The field of hypersonics is an increasing area of interest for Department of Defense research and development. Advances in hypersonic technology present both offensive opportunities and defensive challenges for the United States. Shortly after taking office in March 2018, the Pentagon's chief engineer, Michael Griffin announced that the development of hypersonic capabilities would be his "highest technical priority." [1] Accelerating the development of these systems requires a renewed focus on practical research and design testing.

Thermal effects present a significant challenge to hypersonic flight. Strong shock waves and thin boundary layers contribute to extreme heat transfer to the outer surfaces of a hypersonic vehicle. Specialized materials are required to handle the severe temperatures and designs which aim to reduce heating often sacrifice aerodynamic performance. [2] One way to address the heating load is to exchange heat from the surface to a circulating liquid. Another approach is the use of ablative materials, a practice in use since the early Gemini return capsules and the X-15 program. [3] A better understanding of boundary layer and shock wave behavior in a hypersonic flow environment will allow designers of hypersonic systems to mitigate localized extreme heating regions.

Propulsion presents one of the largest challenges in powered hypersonic flight development. With current technology, rockets are the most practical propulsion source for hypersonic vehicles and missiles. Air-breathing propulsion at hypersonic speeds is tremendously challenging, as fuel does not have enough time to burn when mixed with supersonic air before exiting the combustion chamber. [4] For many envisioned hypersonic applications, altitude also becomes an issue, as oxygen becomes scarce at the edge of the atmosphere. However, rockets are not without their drawbacks either. Transporting oxidizer requires a larger and heavier vehicle. Additionally, throttling rockets is not a trivial task and mid-air refueling is impractical. [5] The effectiveness of either approach is reliant on an understanding of fundamental fluid dynamic phenomena, including shock-wave/boundary-layer interaction.

Flight tests at hypersonic speeds are extraordinarily costly in both money and time, making them impractical for many projects. Instead, development often relies on analytic simulations and scale model testing in wind tunnels. While these alternatives exist, there is much to be learned regarding hypersonic flight, and analytic methods need continual improvement. The growing availability of hypersonic wind tunnels means more opportunities for comparing simulated to experimental results and learning the intricacies of hypersonic flight. [6] Characterizing the test section of the Air Force Research Lab (AFRL) Mach 6 Ludwieg tube and utilizing the facility for fundamental research will aid the ongoing verification process.

Problem Statement

The AFRL Ludwieg tube became operational in 2017. The facility is sized to produce two roughly 100-ms periods of quasi-steady Mach 6 flow. While multiple experiments have been performed in the facility since then, further characterization of the tunnel, specifically flow quality in the test section, was required to expand the usefulness of the facility. A Pitot rake consisting of 12 pressure transducers was used to test flow stability and speed throughout the test section. This characterization was important for future tests performed in the facility, as researchers need to know what portions of the test section experience stable Mach 6 flow. Knowing the behavior of this core flow helped in determining the maximum size of models that can be tested before experiencing boundary layer effects from the tunnel wall. A high-speed Schlieren photography system was configured during the Pitot probe survey to aid in the AFRL Ludwieg tube characterization efforts. Schlieren systems provide a robust method for visualizing and verifying flow. The systems are also generally simpler than setting up heat flux or pressure measurements.

Following the survey, further testing on a cone/flare model was completed. Studying this simple geometry in a hypersonic flow environment was the primary motivation for the project. Prior testing had been performed on the model in the same facility, so the Schlieren system was set up with the goal of gaining further insight into the physics of the hypersonic flow. With the model in place, shock wave and boundary layer behavior around the four interchangeable cone tips with varied bluntness were visualized using the Schlieren system. The model was then repositioned forward in the tunnel to focus on capturing the transition between the upstream cone and the

downstream flare portion of the model using high-speed Schlieren photography. A series of runs were performed on the 16 possible flare angle/nose radius combinations at varying flow Reynolds numbers to gain a better understanding of boundary layer behavior in the presence of an adverse pressure gradient. Post-processing of the images revealed whether transition locations or recirculation regions could be identified using Schlieren photography. The high frame rate video was used to observe transient shock and boundary layer behavior over the course of the run. The success of the Schlieren system demonstrated the usefulness of Schlieren imaging as a diagnostic method in the AFRL Ludwieg tube facility.

Limitations

The AFRL Ludwieg tube was designed with a focus on configuration versatility, system reliability, and minimum turnaround time between runs. These considerations led to some compromises in how well the tunnel simulates hypersonic flight in the atmosphere. The primary discrepancy is that freestream turbulence levels are much higher in the tunnel environment than would be present in typical free-flight conditions. For the cone/flare tests, the additional turbulence meant laminar to turbulent transition occurred further upstream on the model than it would have in a quieter flow, which is generally more common in flight conditions. Turbulence in the Ludwieg tube is discussed further in Chapter II. Optical access via windows of fixed dimension limited the area of the model that could be captured in a given Schlieren image. For some run conditions, boundary layer separation occurred far enough upstream to be out of the frame. Possible

solutions problems encountered and recommendations for future testing will be discussed in Chapter V.

Preview

The following chapters will provide further details pertaining to the experiments performed. Chapter II provides theoretical background and reviews literature related to hypersonics, Ludwieg tubes, Schlieren photography, and prior cone/flare model research. Chapter III discusses the operation of the AFRL Ludwieg tube, the experimental method for performing high-speed Schlieren photography, and the post-processing steps for the Schlieren images. Chapter IV provides results for the tunnel characterization study and presents processed images from the Schlieren testing. Additionally, results relating to observed recirculation regions are compared to a previous study performed with the same cone/flare model using a different measurement technique. Chapter V presents a summary of results, significance of the research, and recommendations for future testing of the cone/flare model.

II. Literature Review

Chapter Overview

This chapter provides a background and a review of literature in subjects related to this project. The first section of this chapter is a brief overview of hypersonic concepts such as shock-wave/boundary-layer interaction, flow instabilities, and ablation. The second section covers Ludwieg tube design and advancements. The third section describes the theory behind Schlieren imaging. The fourth and final section covers prior research related to cone/flare and other simple-geometry models in hypersonic flows. The section includes descriptions of boundary layer stability investigations, laminar-to-turbulent transition, hypersonic wind tunnel details, and a prior experiment involving the same cone/flare model used for the current project.

Hypersonic Background

As discussed in Chapter I, understanding shock-wave/boundary-layer interaction (SBLI) poses a major hurdle in hypersonic research and development. As flight speed increases, shock waves move closer to the vehicle surface and the shape of the shock wave follows the vehicle shape more closely. Increasing Mach number also corresponds to thickening boundary layers. The combination of decreasing shock wave separation and increasing boundary layer thickness can lead to complicated interactions during hypersonic flight. [2] In a 2001 paper, Dolling discusses progress made in this subject from 1950 up to that time. [7] Major progress has been made due to advances in computational and measurement technology, making simulations much more realistic. However, high-velocity gas phenomena like heating in strong interaction regions and

unsteady pressure loads are difficult or even impossible to predict with current analytical methods. The subdiscipline of aerothermodynamics focuses on high-velocity gases and their heating effects.

Bertin and Cummings discuss challenges faced in hypersonic flight and how aerothermodynamics play a crucial role in analysis. [6] Current analytical and numerical methods as well as ground and flight-testing capabilities are summarized. Sustained flight at hypersonic speeds requires robust thermal protection systems (TPS), hence the focus on aerothermodynamics. The 2003 Columbia accident underscores the importance of thermal effects on reentry vehicles. Foam covering the external fuel tank struck the leading edge of the shuttle's wing. Damage from the impact allowed reentry gases to enter the structure, resulting in catastrophic failure. Flight in the hypersonic regime leads to boundary layer interactions, entropy layers, real gas effects, and a host of other phenomena which are difficult to model appropriately. Numerical methods and solutions are improving but still require extensive validation and verification. Ground testing can be performed in conventional and shock-heated wind tunnels, shock tubes, arc-heated test facilities, and ballistic free-flight ranges. These tests can be run to simulate flight under some hypersonic conditions. However, it is difficult to produce all conditions (Reynolds number, Mach number, wall temperature, freestream temperature, material chemistry, etc.) simultaneously. Flight tests can provide realistic flight parameters for verifying ground tests and computational fluid dynamics (CFD) simulations, but the tests are often cost and time prohibitive.

Laminar-to-turbulent transition in a hypersonic flow environment is a continuing area of research, and several mechanisms are thought to contribute to the behavior.

Stability theory is used to predict some transition mechanisms, often known as instability modes. The root causes of these instability modes are not fully understood, but the resulting disturbances can often be identified in flow visualization. Tollmien-Schlichting waves in a subsonic boundary layer are associated with first-mode disturbances. Mack, in the course of research into boundary layer stability theory, found additional disturbance modes. [8] Second, third, and higher modes behave like acoustic waves reflecting between the model or vehicle surface and the boundary layer sonic line. [9] Many instability modes exist, but first and second-mode disturbances are the common focus when studying instability modes. This focus is due to the earliest dominant instability mode in the boundary layer generally tripping the flow to turbulent. [10] An improvement on current understanding of laminar to turbulent transition remains vital for predicting surface temperatures and mitigating the damaging effects during flight.

Ablation effects underscore the importance of understanding transition and predicting the discussed hypersonic phenomena. Transition and SBLI regions often result in extreme localized heating. During sustained flight, the combination of heat and friction can cause material to wear away, resulting in major aerodynamic and structural integrity implications. Nachtsheim and Larson demonstrated ablation patterns on a Teflon cone model in 1971, and their results illustrate the effect of transition on heat transfer. [11] The testing provided two key takeaways, the effects of which can be seen in Figure 1. First, besides some blunting of the cone tip, the front portion of the cone displayed little material loss due to the presence of a laminar boundary layer. The midpoint of the cone showed a drastic increase in the amount of material lost. This ablation was associated with the much higher heating rates of a transitioning boundary layer environment.

Second, cross-hatch patterns were displayed on the downstream portion of the cone, where the boundary layer was fully turbulent. The cross-hatching phenomenon is still not well understood. The behavior is possibly due to dynamic instabilities such as first and second-mode disturbances in the turbulent boundary layer. Whether by gross removal of material or by patterning, this deformation is of great concern, as the shape change is likely to exacerbate dynamic instabilities if this process occurs during flight. On the other hand, if transition could be delayed, there would be tangible benefits for hypersonic vehicle design.

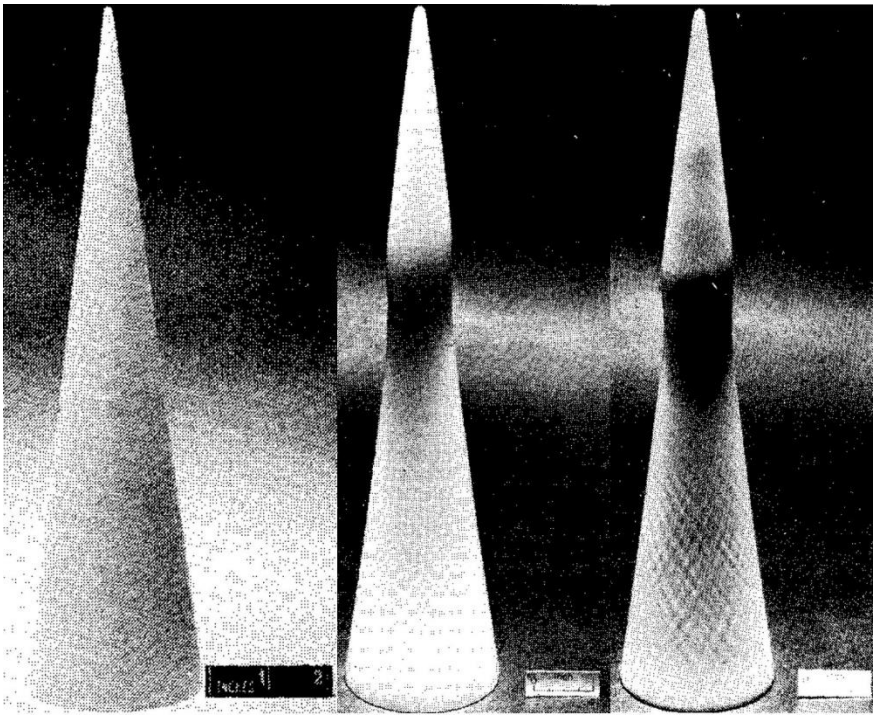

Figure 1. Teflon Cones [11]

(left, pretest shape) (middle, displaying transistion wear) (right, displaying cross-hatching)

Ludwieg Tube Background

Shock tubes are simple and comparatively low-cost devices for generating supersonic flows. The basic shock tube model consists of a constant-diameter tube with a pressurized “driver” section separated from a low-pressure region by a burst diaphragm or other fast-open device, as shown in Figure 2. When the diaphragm is burst, the sudden pressure differential induces a shock wave as natural forces try to restore equilibrium. The shock wave travels through the low-pressure chamber until it meets the end wall and is reflected as an incident shock wave. Similarly, expansion waves propagate through the high-pressure chamber before being reflected by the other end wall. The waves continue reflecting and interacting with one another until equilibrium is attained. The equilibrium process occurs quickly, resulting in a very short run time compared to conventional supersonic wind tunnels. Low construction and operating costs in addition to short downtime between runs make shock tubes valuable in a research environment. [12] A Ludwieg tube is an improvement of the basic shock tube design. The primary changes are the introduction of a converging/diverging nozzle and a large vacuum tank in the downstream section. The improvements allow flow to be accelerated to a desired Mach number, and therefore velocity, based on the sizing and geometry of the nozzle. A large vacuum tank downstream of the test section allows for longer periods of steady flow as high-pressure air from the driver tube flows into the test section to equalize pressure.

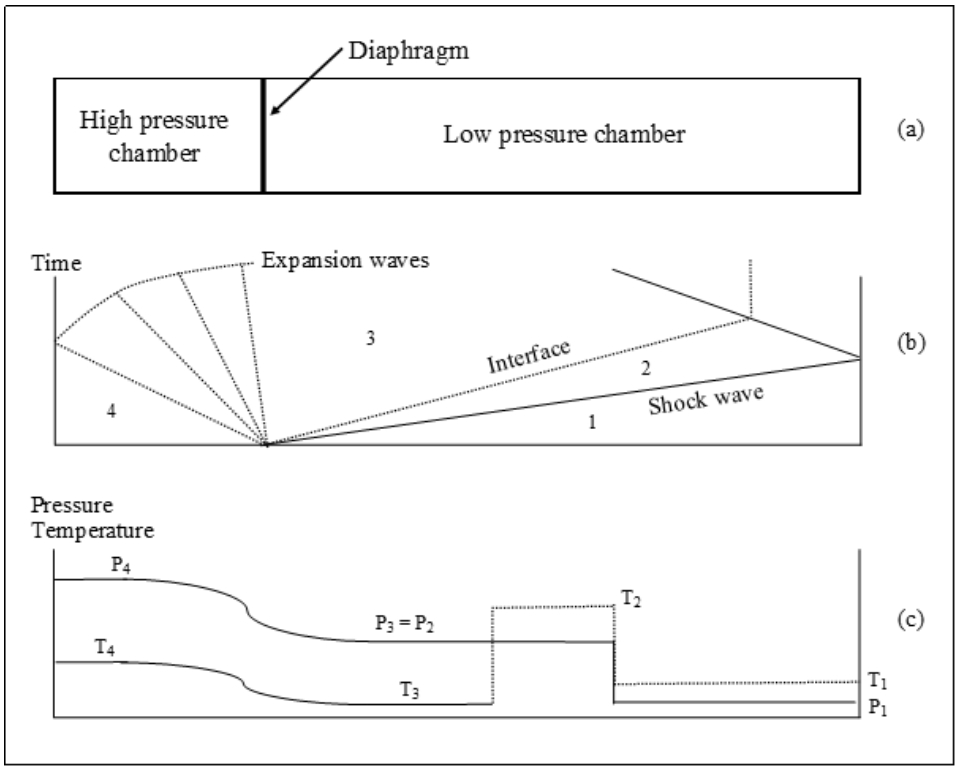

Figure 2. Shock tube operation [12]

(a): Simple shock tube (b): Wave system in a shock tube (c): Pressure and temperature at a given time

Recent trends in wind tunnel design include the construction of "quiet" tunnels to better simulate flight conditions. Quiet tunnels are built to maintain a laminar flow by bleeding off the boundary layer before it grows enough to trip to turbulent flow. Modern hypersonic quiet tunnels were pioneered by Steven Schneider of Purdue University. Based on testing, Purdue's quiet tunnel is able to maintain laminar Mach 6 flow with one-tenth to one-thirteenth of the noise in other high-speed wind tunnels. [13] In addition to bleeding off some of the boundary layer, the surface inside the wind tunnel must maintain a smooth mirror finish as small bits of roughness can trip a laminar flow to turbulent. These tunnels provide unique experimental opportunities. However, researchers must

determine whether the additional complexity and cost associated with a quiet tunnel is justified for a given project.

Schlieren Background

Schlieren photography is used to visualize spatial variations in density in a flow environment. Shock waves cause sharp density gradients and are therefore easily visible on a properly exposed Schlieren image. While several variations of Schlieren systems exist, a two-mirror Z-type system, diagramed in Figure 3, is most commonly used in wind tunnel testing if sufficient optical access is available. In a Z-type system, light from a bright lamp or arc is focused to a point and passed through a pinhole aperture or slit. The light diverges from the pinhole to a concave mirror. The light reflected from the concave mirror is collimated, meaning all light rays are parallel as they pass through the test area. The aperture must be located at the concave mirror's focal point for the reflection to be properly collimated. Another concave mirror captures the collimated light and focuses it to a point. A knife edge is placed at the second mirror's focal point. If density gradients are present in the test section, the parallel light rays will be refracted and will no longer pass through the second mirror's focal point. The knife edge cuts the refracted rays off, resulting in an image with light and dark spots corresponding to changes in density. With the advent of high-speed cameras, it is common to use Schlieren systems to characterize temporal changes in high-speed flows. [14]

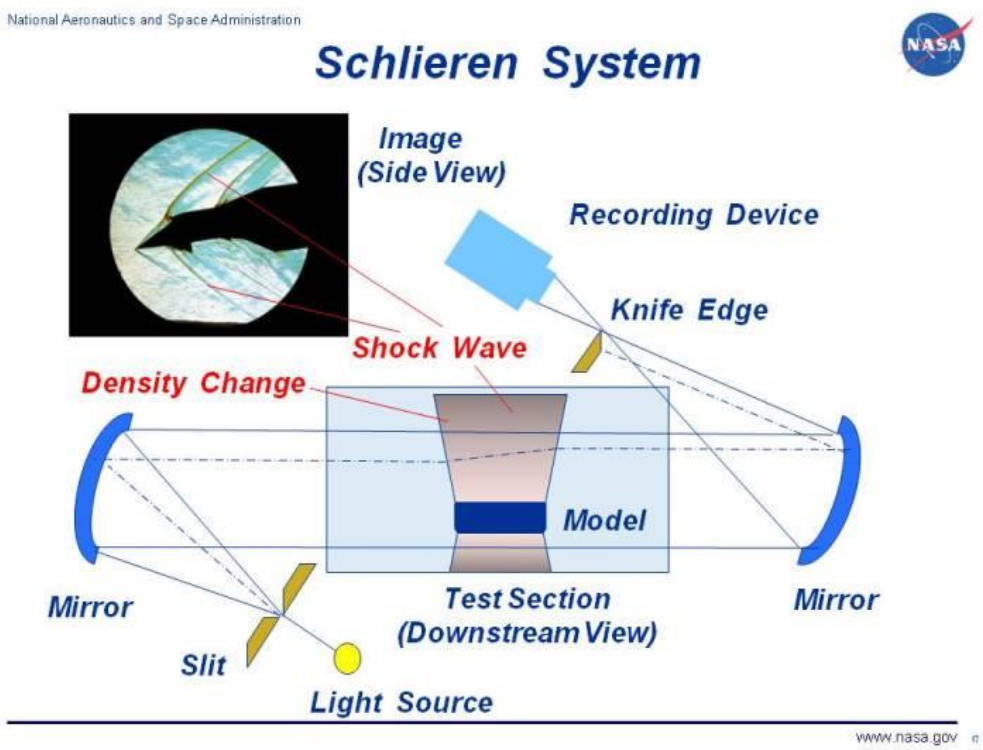

Figure 3. Schlieren Diagram [14]

Hypersonic Cone/Flare Research

In 1989, Stetson et al. discuss laminar boundary layer stability on a 7° half-angle, water-cooled cone at Mach 8. [15] The cone consisted of an uncooled 13-8 stainless steel nose and a cooled 6061-T6 aluminum frustum separated by a Micarta thermal insulator. Temperature measurements were taken using a hot-wire anemometer. Results from the cooled-surface test were compared to the uncooled test to study the effects of wall temperature on laminar boundary layer stability. The cooled surface was found to stabilize first-mode disturbances while destabilizing second-mode disturbances, an outcome predicted by linear stability theory. Cooling the surface had little effect on the second-mode disturbance frequencies but maximum disturbance growth rates increased

up to 50% from the uncooled case. Approximate laminar-to-turbulent transition Reynolds numbers decreased from 4.8×10^6 for the uncooled surface to 3.2×10^6 for the cooled surface. The researchers used hot-wire anemometry, which yielded good insight despite its intrusiveness.

In 1966, Wilson examined boundary layer behavior on cones at hypersonic speeds. [16] He expanded on a momentum-integral method previously used to calculate laminar boundary layer growth to include some effects of turbulent flow. Studies revealed that blunting the cone nose had a significant effect when calculating local Mach number and local shear stress due to the presence of a laminar boundary layer. Laminar flow led to lower cone drag coefficients with a sharp increase in drag when the flow tripped to turbulent. Wilson's more robust version of the momentum-integral method was shown to accurately compensate for the bluntness change with support from experimental data. Numerical and experimental results showed increased Reynolds numbers bring the onset of transition closer to the nose of the cone. Early analytical methods like the momentum-integral led to the advent of more powerful CFD simulations.

In 2006, Hader and Fasel described CFD investigations into laminar-to-turbulent transition performed on a flared cone at Mach 6. [10] Turbulence in hypersonic boundary layers generates additional shear stress and heat transfer on a vehicle's surface. These aero-thermal loads are responsible for some of the most difficult challenges related to hypersonic flight. TPS solutions drastically increase weight, cost, and complexity of hypersonic vehicle structures. Simulations focused on unstable frequency bands and identified the azimuthal wave number which was associated with the strongest turbulent growth rate. Instabilities created resonance patterns which led to high skin friction and

streamwise streaks on the cone surface. These streaks were areas of high heat transfer. The simulations backed up results observed when a flared cone of the same geometry was tested in the Boeing/AFOSR Mach 6 Quiet Tunnel (BAM6QT).

Another recently constructed Mach 6 tunnel in Beijing, China was used by Zhang et al. to study transition on a flared cone at zero angle of attack. [17] The authors describe the facility as a quiet tunnel. Pressure transducers measured amplitudes and frequencies of second-mode waves. Pulsed Schlieren diagnostic and Rayleigh scattering techniques were used to visualize the second-mode disturbances. The combination of pressure measurements and flow visualization provides a clearer picture of how the boundary layer develops and eventually transitions to fully turbulent flow. The study found that second-mode wave structures can grow until nonlinear interactions decrease the wave amplitudes. This dampening causes the structures to merge, leading to a quiet zone before the transition to turbulence. The authors state that the transition caused by second-mode waves was found to be different from that caused by first-mode transition.

Li et al. discuss instabilities in boundary layer second-mode disturbances. [18] Instability is the mechanism which brings about turbulent transition and can play an important role in understanding boundary layer behavior. Second-mode disturbances generally lead to the highest amplification rates with 2D or axisymmetric perturbations. This phenomenon is most commonly evident in axisymmetric bodies (such as flared cones) at zero angle of attack experiencing hypersonic flow. Computations performed in the study confirmed subharmonic modes dominate at small amplitudes. However, for a Mach 6 cone configuration, updated computation methods revealed that primarily focusing on subharmonic modes may be a poor assumption. The results showed “a strong

fundamental secondary instability can exist for a range of initial amplitudes of the most amplified second mode disturbance," emphasizing the importance of accurately modeling second-mode behavior.

Holden et al. performed shock/boundary layer interaction studies on a 7° half-angle cone/40° flare model and a hollow cylinder/36° flare model. [19] Prior to the tests, previous comparisons between predicted and experimental results were summarized. Researchers found a drastic breakdown in simulated results when attempting to predict turbulent flow behavior upstream of shock-wave/boundary-layer interaction regions. Additional wind tunnel testing would provide better data to improve computational methods, which are less refined in simulations above Mach 5. The models in the study were tested at a wide variety of Reynolds numbers at Mach numbers ranging from 5 to 10. Schlieren and laser interferometry flow measurements were performed, and surface pressure and heat transfer measurements were recorded to gain a better understanding of boundary layer behavior with a focus on the recirculation region at the cone/flare junction. Figure 4 shows how the area of the recirculation region grows as wedge angle and therefore adverse pressure gradient are increased. Flow Mach number and Reynolds number from the test were unspecified. Results from the model testing were presented in a format to be used in future CFD code validation studies.

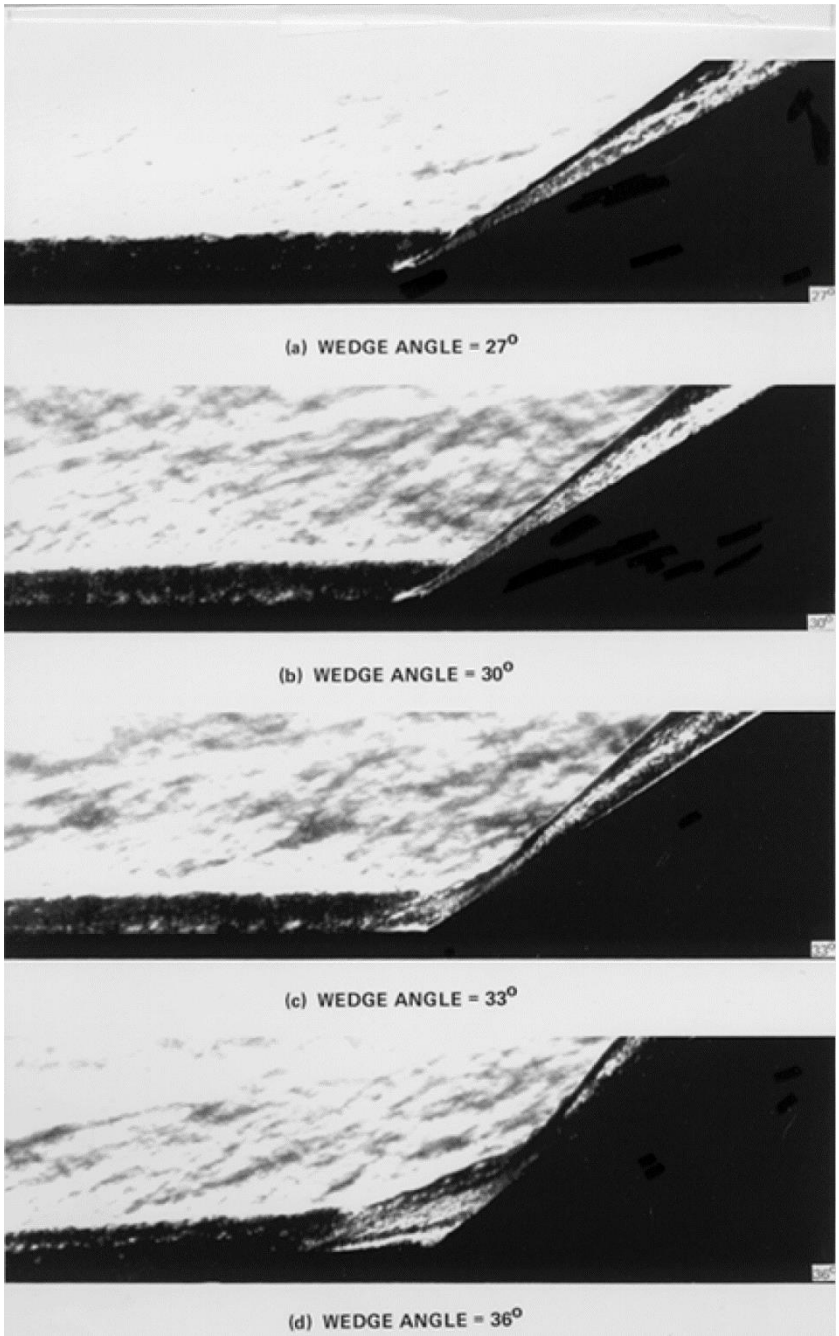

Figure 4. Turning Angle Effect on a 2-D Wedge of Varied Angle [19]

Borg and Kimmel studied crossflow instability with a 2:1 elliptic cone in the BAM6QT Mach-6 quiet tunnel. [20] Freestream noise levels and angle of attack (pitching) were varied to understand the effect on crossflow instability which was

measured with an infrared camera and pressure sensors. Stationary and travelling crossflow instabilities were only observed in the quiet freestream tests. For the quiet flow case, when angle of attack was changed from 0° to 2°, transition Reynolds number increased up to 30%. In general, increasing pitch suppressed stationary and travelling crossflow instabilities. Transition was observed using pressure sensor data for the noisy flow case. Power spectra results suggested that crossflow instability had some effect on transition in noisy flow.

Jewell et al. discuss startup process simulations for the design of a Mach 6 quiet Ludwieg tube at the University of Notre Dame. [21] A viscous, two-dimensional axisymmetric version of the Eilmer3 code was used for the simulation. Four valve-opening speeds ranging from 0 to 120ms were used. Instant opening time is ideal, though not realistic with current valve designs. Additionally, three different positions for the shutter valve were simulated. Results showed positioning the valve closer to the nozzle throat, at the nozzle contraction exit, produced the steadiest core flow with the shortest startup time. This position also allows for a smaller diameter valve, drastically reducing the cost. As expected, faster opening times produced steadier flows downstream of the nozzle. Overall, the simulation showed good flow uniformity for the tested design and predicted that the desired Mach number and pressure will be achievable.

High speed Schlieren and PLIF visualization were performed by Kimmel et al. as part of the initial performance investigations for the AFRL Ludwieg tube. [22] Schlieren images could be recorded quickly enough to capture startup behavior and the associated shocks. These images helped characterize tunnel noise and interpret pressure sensor measurements. Video was recorded at a very high frame rate to capture high-frequency

disturbances and derive frequency spectra for a 2.59-MPa test. After characterization, Schlieren and 10-Hz Kr PLIF were used to obtain images of bow shocks on a blunt cone. Excellent agreement regarding the bow shock shape was found when the measurements were compared to CFD simulations for the same cone geometry.

Running et al. used the AFRL Ludwieg tube to study shock-wave/boundary-layer interaction on a cone/flare model at Mach 6. [23] Tests were performed on a 7° half-angle cone with 16 different flare angle/bluntness geometry combinations. Based on analysis, the two sharper nosetips generated turbulent boundary layers while the two blunter nosetips generated laminar boundary layers. Infrared thermography measurements revealed the state of the boundary layer on the upstream portion of the model. A rapid jump in heat transfer, characterized by Stanton-number, can be used to indicate transition location. In general, Stanton-number is the dimensionless ratio of heat flux to the thermal capacity of a material or fluid. Additionally, Stanton-number contours and profiles were calculated for the downstream portion of the cone/flare. The downstream calculations revealed the effects of freestream Reynolds number, flare angle, and nosetip bluntness on boundary layer behavior. Increasing flare angle and/or cone tip bluntness increased the length of the separation region. Increasing freestream Reynolds number was found to decrease the separation length. It was determined that changing flare angle and/or freestream Reynolds number effected peak heating levels and the heating slopes more than changing cone tip bluntness. In addition, some asymmetry was noted on the model. It was suggested by the authors that this finding merited further investigation.

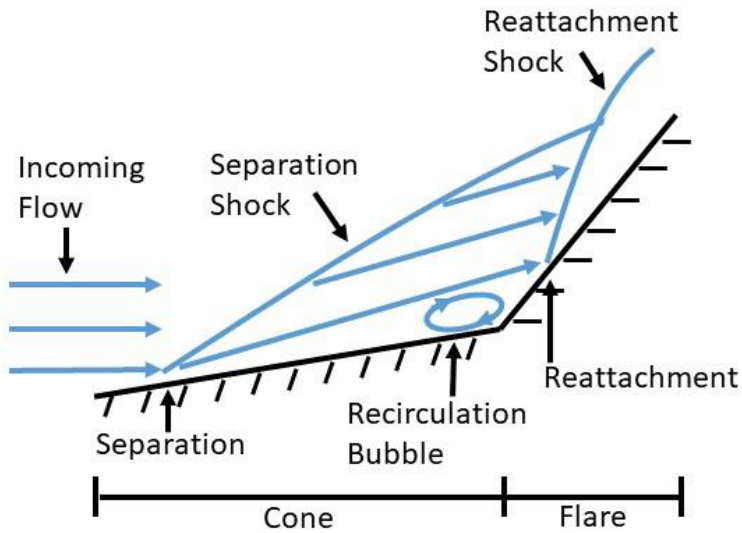

Figure 5. Boundary layer behavior with an adverse pressure gradient [23]

The flare is responsible for an adverse pressure gradient along the cone frustum which leads to the separation illustrated in Figure 5. The subsonic boundary layer transfers higher pressure induced by the turning angle of the flare upstream to the cone frustum. This pressure causes the boundary layer to separate ahead of the cone/flare junction. The separated boundary layer is directed by the incoming flow back toward the flare, where it reattaches. Reattachment causes another shock ahead of a thin, high-pressure boundary layer. This non-ideal boundary layer is responsible for high aerodynamic heating in the region. Testing the combination of 16 flare angle/bluntness geometries at varying freestream Reynolds numbers revealed several patterns. For laminar boundary layers, increasing nosetip bluntness caused the separation location to move further upstream while reattachment moved further downstream. Increasing bluntness also generated higher peak heating levels. This result is expected because more surface area is subjected to a turbulent boundary layer with a blunt nosetip. Turbulent

boundary layers did not appear to react to increasing nosetip bluntness. Increasing the flare angle resulted in a larger separation region as separation moved upstream and reattachment moved downstream. Finally, increasing the Reynolds number for laminar boundary layers moved separation downstream. Observations could not be made for turbulent separation or reattachment for either case with the collected data. Visualizing flow on the cone/flare model with high-speed Schlieren will provide a clearer look into how variations in nosetip bluntness, flare angle, and freestream Reynolds number will affect the separation region.

Summary

The provided overview of hypersonic concepts underscores the importance of experimental hypersonic testing. Ludwieg tube facilities are simple and effective means of performing hypersonic flow experiments. High-speed Schlieren photography is a non-intrusive method for flow visualization that can be used to quickly observe hypersonic flow patterns and transient phenomena. The testing herein is intended to provide further insight into shock-wave/boundary-layer interactions and unstable boundary layer behavior.

III. Methodology

Chapter Overview

This chapter covers the procedures involved in characterizing the AFRL Ludwieg tube, capturing the Schlieren images, and post-processing the high-speed videos. The first section provides a detailed description of the Ludwieg tube facility including the supporting equipment, control methods, and the data acquisition system. The second section describes the Schlieren setup used to image the cone/flare model. This section includes details of the equipment used and post-processing methodology.

Ludwieg Tube Facility

The AFRL Ludwieg tube is designed to produce hypersonic flow conditions with a short turnaround time between tests. A Mach 6 nozzle is currently installed upstream of the test section. Reynolds number per unit length may be adjusted based on the driver tube static pressure and/or the stagnation temperature settings. Turnaround time is usually limited to the driver tube charging rate. For example, a full pressure, 580 psia run, requires about 12 minutes to prepare. Low-pressure runs require less charge time and are usually limited by vacuum pumping time. The lowest operating stagnation pressure used for the testing herein was 200psia. A full description of the tunnel operation is presented in the AFRL Ludwieg tube initial performance report by Kimmel et al. [24]

The driver tube is supplied by two Sauer compressors which produce 50 SCFM at 580 psi. Air in the test section is evacuated by two Leybold vacuum pumps with a maximum pumping rate of 444 CFM each. The compressors and vacuum pumps, shown in Figure 6, are paired to prevent downtime in the event of maintenance or failure. It is

imperative that at least one compressor is running whenever the inlet feed heater is active, as the element can quickly overheat without a supply of fresh air. The compressors must periodically shut down to drain built up condensation. Startup for the compressors is staggered to prevent an overlap where both compressors drain condensate at the same time. [24]

Figure 6. Compressors (left) and Vacuum Pumps (right)

When the Ludwieg tube is in operational mode the compressors run continuously, eliminating the need for an accumulator tank. Additionally, the run scheme reduces compressor startup/shutdown cycles and prevents the maximum system pressure from surpassing the rating of the driver tube. A 1-inch schedule-40 stainless steel line with a series of three 2-inch ball-valves is used to fill the driver tube. The valve system is necessary for the compressors to run continuously as pressure can be vented outside when the driver tube is charged to the desired pressure. The feed heater is an 18kW Sylvania resistance heater which preheats the driver tube air to 450°F while charging. [24]

The driver tube itself is built from 9.75-inch inside diameter 304 stainless steel pipe. Due to space constraints the tube is built in two parallel 35ft sections connected by a 180° bend. This configuration is known as a “reflexed driver tube” and has been used in past Ludwieg tube designs. The bend is shown in Figure 7. An unsteady CFD simulation revealed that the bend would not contribute to undesired wave reflections. During the two 100ms periods of quasi-steady flow, the driver tube air that enters the test section is supplied by the straight 30ft section of tube closest to the nozzle. This phenomenon ensures the flow during the useful period is uncontaminated by the bend. The driver tube is wrapped with blanket resistance heaters over the entire length, maintaining the tube at 450°F to prevent thermal losses. Uniform heating prevents the need for varying driver tube diameter and minimizes convection losses. [24]

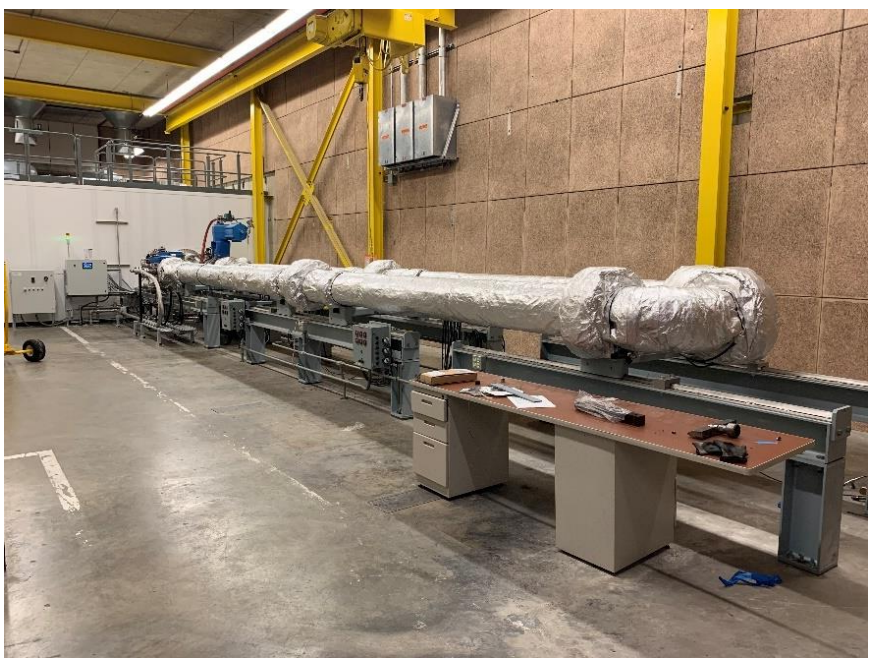

Figure 7. Driver tube section

The Mach 6 nozzle consists of three sections. The throat is built out of 316 stainless steel and the two downstream sections are built out of 6061-T6 aluminum. Initial nozzle design was a product of the method of characteristics and verified with Reynolds-averaged viscous computational fluid dynamics. The final design required compensation for a growing boundary layer on the nozzle surface with viscous corrections. The adjustment resulted in an area ratio 23% larger than the initial inviscid design. Throat diameter is 3.71 inches and nozzle exit diameter is 30 inches, creating an area ratio of 65.4. Upstream of the nozzle is a 10-inch length of 10-inch diameter pipe, providing a straight lead-in for the throat contraction. The overall length of the nozzle is 117 inches. [24]

The test section of the Ludwieg tube is located directly downstream of the nozzle exit. It is built out of 50-inch diameter carbon steel pipe. Access is available via three circular hatches, one on either side and one at the top of the test section. The side doors can accommodate up to 12-inch diameter optical access windows while the top hatch can house up to a 4-inch diameter window. For the Schlieren tests, 12-inch fused silica windows were installed. A climate-controlled room, with most of the space dedicated to working around the east hatch, was built around the test section. The exterior of the room is shown in Figure 8. For ease of access, the east hatch is an autoclave door, operated with a pneumatic locking system, as shown in Figure 9. A 4ft by 8ft Thor Labs optical table is aligned with the east hatch. The west side has a 3ft by 4ft table due to space constraints. The tables provide a solid, vibrationally dampened mounting surface for optical equipment. Dampening is important because the vibrations induced by the Ludwieg tube transfer into the concrete floor of the building. [24]

Figure 8. Test section room

Figure 9. Autoclave door with optical access

Downstream from the test section is a 44-inch diameter capture cone which directs flow to the diffuser. The diffuser is a 127-inch long, 29.5-inch inside diameter straight pipe with a 6° converging inlet cone and a 4° diverging exit cone. A safety vent is included between the test section and the diffuser inlet. The vent houses two 12-inch flapper valves which will open if the pressure in the test section rises above atmospheric pressure. A Y-junction connects both valves to a 22-inch exhaust which ducts bypass air outdoors. The diffuser outlet is connected to two 2000-gallon receiver tanks with a 30-inch diameter flex coupler, shown in Figure 10. One tank is positioned in line with the diffuser outlet. It is protected from debris impacts by a removable internal doubler. The vacuum pumps pull from both receiver tanks via six-inch diameter schedule-40 stainless steel pipe. [24]

Figure 10. Vacuum tanks

The AFRL Ludwieg tube primarily uses a fast valve to start runs. The tunnel is also set up to use a ball valve or a diaphragm. These methods are rarely used, as the fast valve produces the cleanest runs because it opens faster than a ball valve and no downtime is required to replace a burst diaphragm. The fast valve consists of a large aluminum plug which is held in the closed position by driver tube pressure applied to the back of the plug. When a run is commanded, pressure behind the plug is evacuated. Pressure at the front of the valve forces it into the open position. A stiff nylon cushion is placed at the back of the plug to avoid metal-to-metal contact when the valve slams backwards during operation. The nylon cushion has proven reliable for hundreds of runs without showing degradation or damage to the fast valve plug.

The tunnel in operated remotely in a noise-insulated control room through the use of a programmable logic controller which communicates via an Ethernet cable. The system allows the tunnel to be charged, discharged, and fired from the control room. Diagnostic information is also relayed to the controller. A 16-channel Gantner data acquisition system captures tunnel process data such as driver tube, nozzle, and test section pressures. Measurement data goes through a separate HMB Genesis system with 48 channels. This system can handle instruments with higher bandwidth and sampling rate requirements. [24]

For the purposes of the testing herein, Reynolds number per unit length is useful for describing flow conditions. The flow Reynolds number can be calculated using Equation 1 and known conditions in the driver tube: set temperature (T_0) and pressure (P_0). The initial expansion in the driver tube after the fast-valve opens means stagnation temperature (T_1) and pressure (P_1) are slightly lower before expansion through the

nozzle. Stagnation temperature can be found from the isentropic expansion relation and a given stagnation pressure, as shown in Equation 2. The stagnation pressure is based on average pressure sensor data at the beginning of a run. The stagnation air density (ρ_1) can be calculated from stagnation temperature and pressure using the ideal gas law, presented in Equation 3. Freestream (test section) temperature (T_∞) and density (ρ_∞) can then be found using isentropic relations and freestream Mach number, as shown in Equations 4 and 5. Freestream velocity (V_∞) and dynamic viscosity (μ_∞) are based on the resulting freestream temperature. The tests were performed at driver tube pressures of 200psia and 400psia. Relevant conditions are summarized in Table 1.

$$Re_\infty/_L = \frac{V_\infty \rho_\infty}{\mu_\infty} \tag{1}$$

Where:

V_∞ = Freestream velocity
ρ_∞ = Freestream density
μ_∞ = Freestream dynamic viscosity

$$T_1 = T_0 \left(\frac{P_1}{P_0}\right)^{1-1/\gamma} \tag{2}$$

Where:

T_1 = Stagnation temperature
T_0 = Driver tube temperature
P_1 = Stagnation pressure
P_0 = Driver tube pressure
γ = Ratio of specific heats

$$\rho_1 = \frac{P_1}{RT_1} \tag{3}$$

Where:

P_1 = Stagnation density
P_1 = Stagnation pressure
R = Specific gas constant
T_1 = Stagnation temperature

$$T_\infty = T_1\left(1 + \frac{\gamma - 1}{2} M_\infty^2\right)^{-1} \tag{4}$$

Where:

T_∞ = Freestream temperature
T_1 = Stagnation temperature
γ = Ratio of specific heats
M_∞ = Freestream Mach number

$$\rho_\infty = \rho_1\left(1 + \frac{\gamma - 1}{2} M_\infty^2\right)^{-1/\gamma - 1} \tag{5}$$

Where:

ρ_∞ = Freestream density
ρ_1 = Stagnation density
γ = Ratio of specific heats
M_∞ = Freestream Mach number

Table 1. Test Conditions, Assuming Isentropic Flow

Set Pressure (psia)	**P_1 (kPa)**	**T_1 (K)**	**M_∞**	**T_∞ (K)**	**V_∞ (m/s)**	**ρ_∞ (kg/m^3)**	**μ_∞ (kg*m^{-1}*s^{-1})**	**Re_∞/L (m^{-1})**
200	1240	490.3	6.1	58.1	917	0.0425	$3.757\cdot10^{-6}$	$10.4\cdot10^{6}$
400	2450	488.6	6.1	58.9	915	0.0844	$3.742\cdot10^{-6}$	$20.6\cdot10^{6}$

Figure 11 shows a typical pressure trace from the AFRL Ludwieg tube. The figure shows raw voltage output from the pressure transducer as a function of time. This signal can be directly converted to pressure using unique calibration data for each sensor. Conversion is unnecessary, as the quantity of interest for describing core flow is the net change along the y-axis as time progresses. During a run, a trigger signal is sent to the data acquisition system when an upstream pressure transducer detects the normal starting shock which originates from the opening of the fast-valve. The sharp rise in pressure as the starting shock passes the transducer that supplied the data in Figure 11 is visible at 0ms on the graph. The 0ms point also coincides with the input of the trigger signal. After

the normal shock passes, pressure rises quickly as the core flow nominally reaches Mach 6. The first period of quasi-steady flow lasts from about 25ms until 125ms. After the first shock reflection, pressure, and therefore Mach number of the flow, drops slightly then remains quasi-steady for another period lasting about 100ms. After the second quasi-steady flow period and the next shock reflection, pressure drops again, and the tunnel no longer produces useful flow.

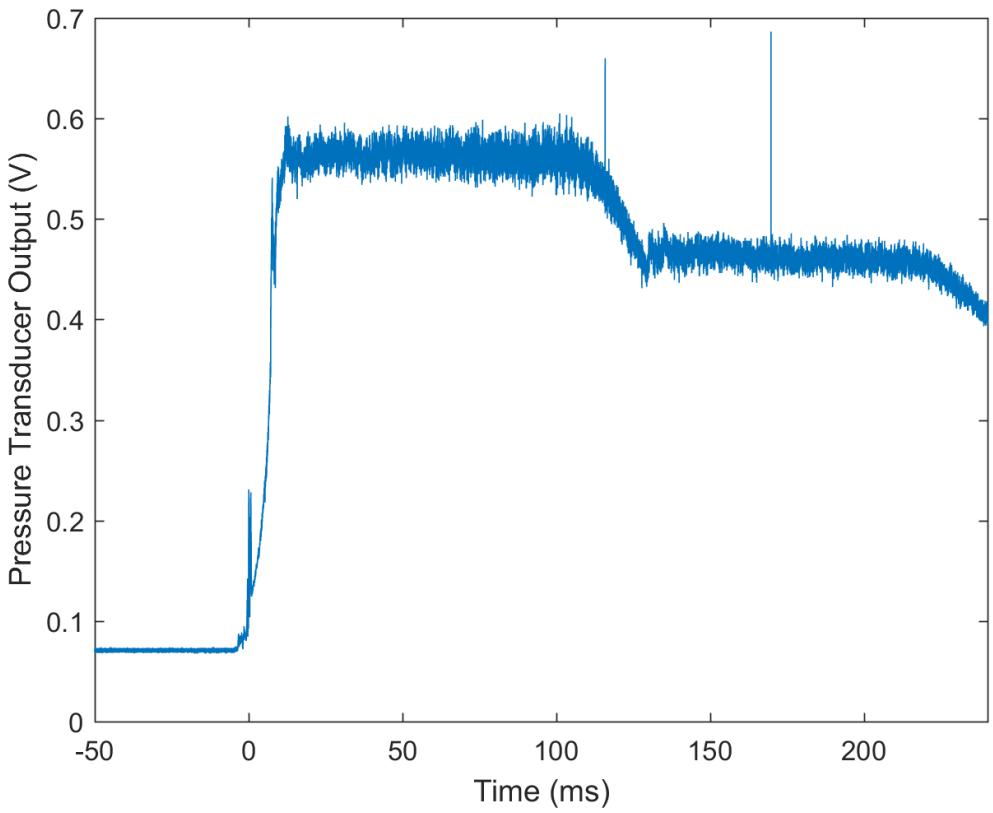

Figure 11. Typical Pressure Trace

High Speed Schlieren

The Schlieren setup was based on a two-mirror Z-type system. Two large concave mirrors, 31.8cm in diameter, were used to collimate and refocus the light. The shallow curvature of the mirrors gave each of them a focal distance of 1.92 meters. A long focal distance improves sensitivity in two-mirror Schlieren systems. Due to limited space on the light source side of the system, a 3-inch and a 6-inch flat mirror were used to redirect the light beam to attain the required focal distance. On the camera side of the system, a single 6-inch flat mirror was sufficient to redirect the light. A focusing lens was positioned 9/16 of an inch from the lens on the Newport 66921 light source. After the focusing lens, a rectangular aperture spaced 15/16 of an inch from the lens restricted the beam to a pinhole before diverging toward the large concave mirror. Due to space constraints and available flat mirrors, some of the beam was cut off before passing through the test section. As a result, the collimated beam was not the full 31.8cm diameter, limiting area captured in the image. A razor blade served as the knife edge used to cut off the light beam. The modular nature of the optical equipment meant switching between horizontal and vertical cutoff configurations could be performed quickly, without disturbing the rest of the system. Figure 12 shows the light-source side of the system, except for the flat 6-inch mirror. Figure 13 shows the location of the flat 6-inch mirror relative to the large concave mirror. The sheet of cardboard was used as a divider to redirect warm air from the light source cooling fan. Without the divider in place, the heated air passed directly though the Schlieren frame, adding noise to the image. An overview diagram of the Schlieren system is provided in Figure 14.

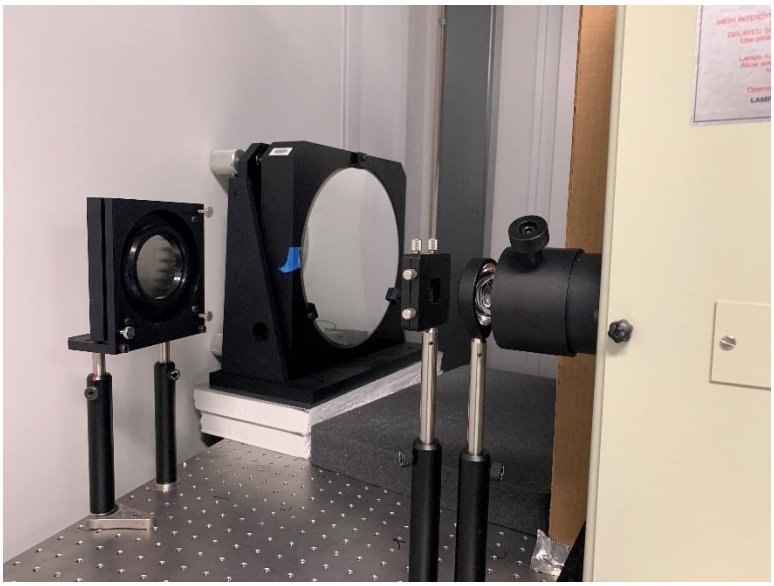

Figure 12. Light source, focusing lens, aperture, and 3-inch mirror

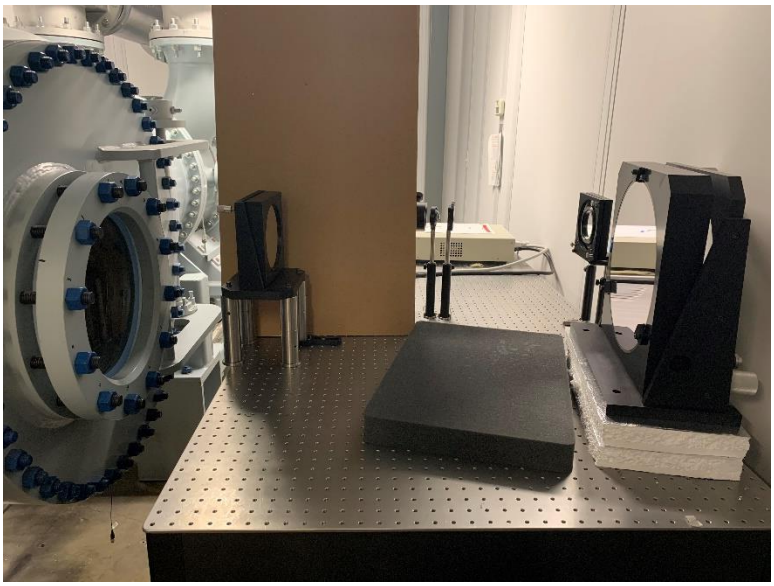

Figure 13. 6-inch and concave mirrors

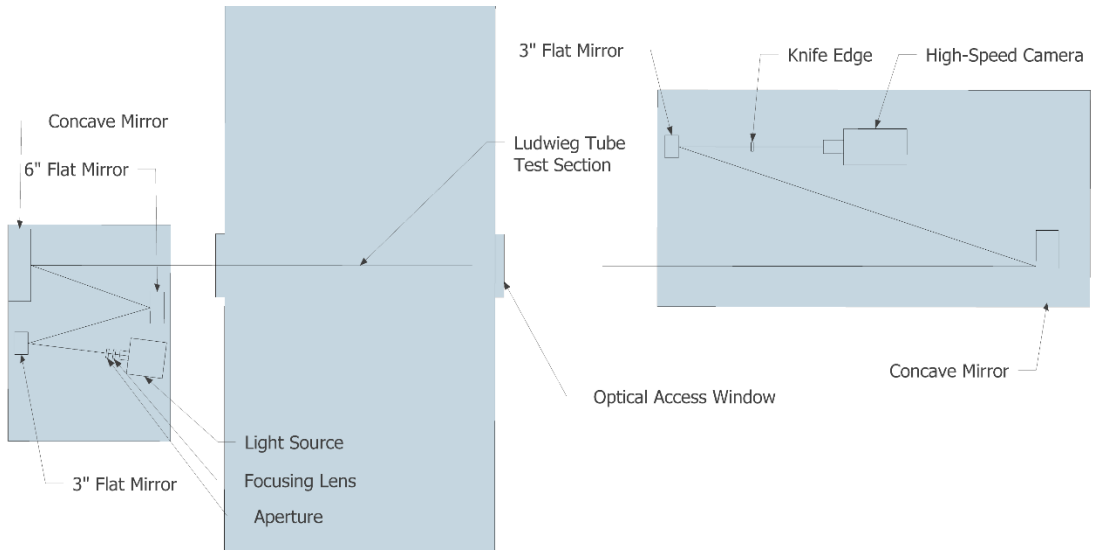

Figure 14. Schlieren System Diagram (Not Drawn to Scale)

The modular 6061-T6 aluminum cone/flare model used for testing, diagramed in Figure 15 and Figure 16, was the same one used by Running et al., as discussed in Chapter II. [23] The model consists of four base flares with angles of 34°, 37°, 40°, and 43°. A single 7° half-angle circular cone section bolts to the flare bases. With the sharp tip installed, the cone section is 610mm long. Length decreases slightly with blunter nose tips. The flare section is 76mm long for all four flare angles. When swapping flare angles between runs, the cone had to be unbolted and transferred to the new base. The font portion of the cone has a threaded end to allow different nose tip configurations to be attached. Four tips with nose radii of 10.2mm, 5.1mm, 0.5mm, and 0.0mm were used in testing. The 10.2mm and 5.1mm tips are characterized as “blunt.” The model was positioned in the test section at nominally 0° pitch and yaw relative to the freestream. Figure 17 shows the 43° base with 10.2mm radius tip installed at the rearward sting position in the Ludwieg tube test section.

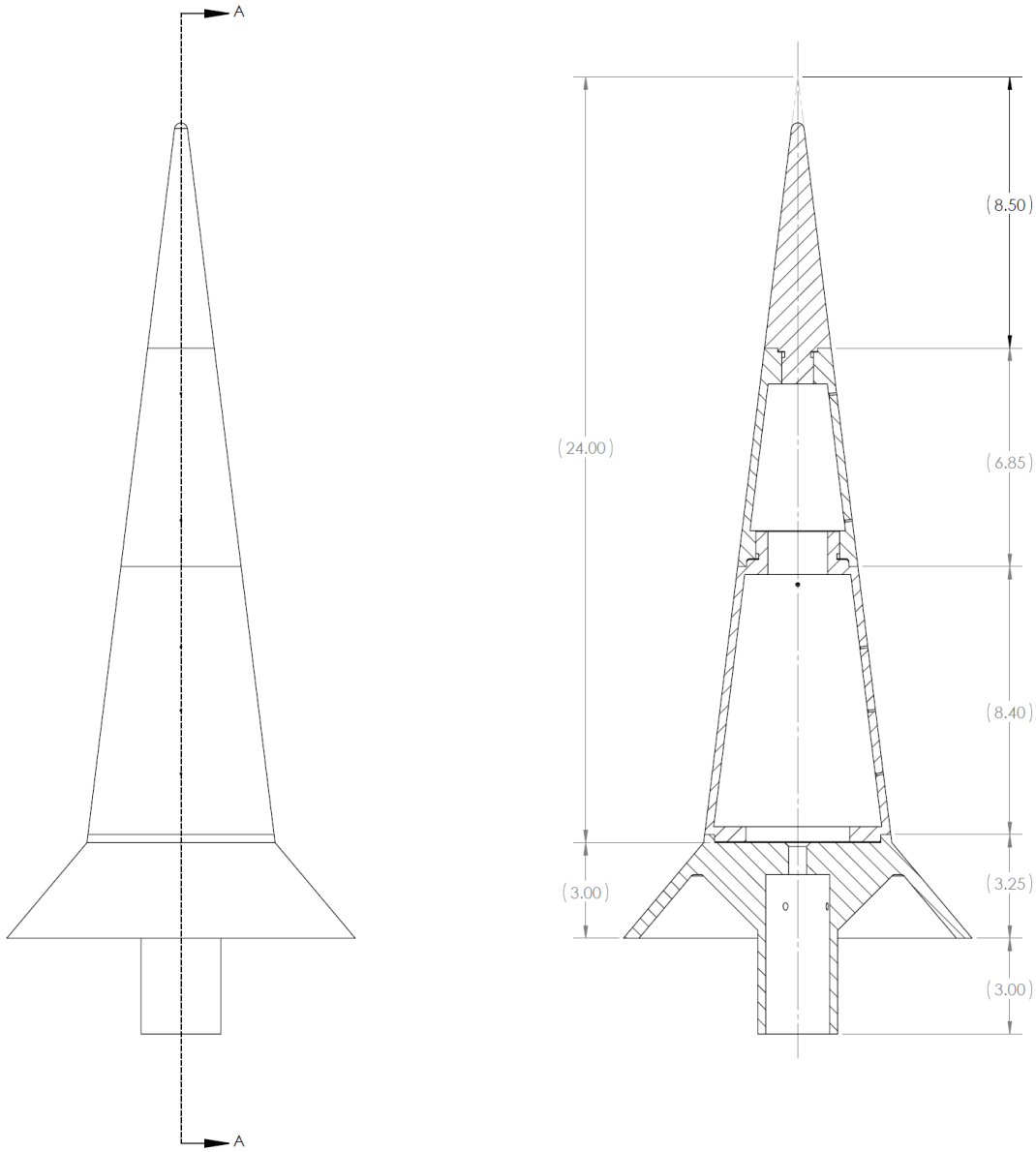

Figure 15. Cone/Flare Model Assembly (5.1mm Radius Tip, 40° Flare Shown) (dimensions in inches)

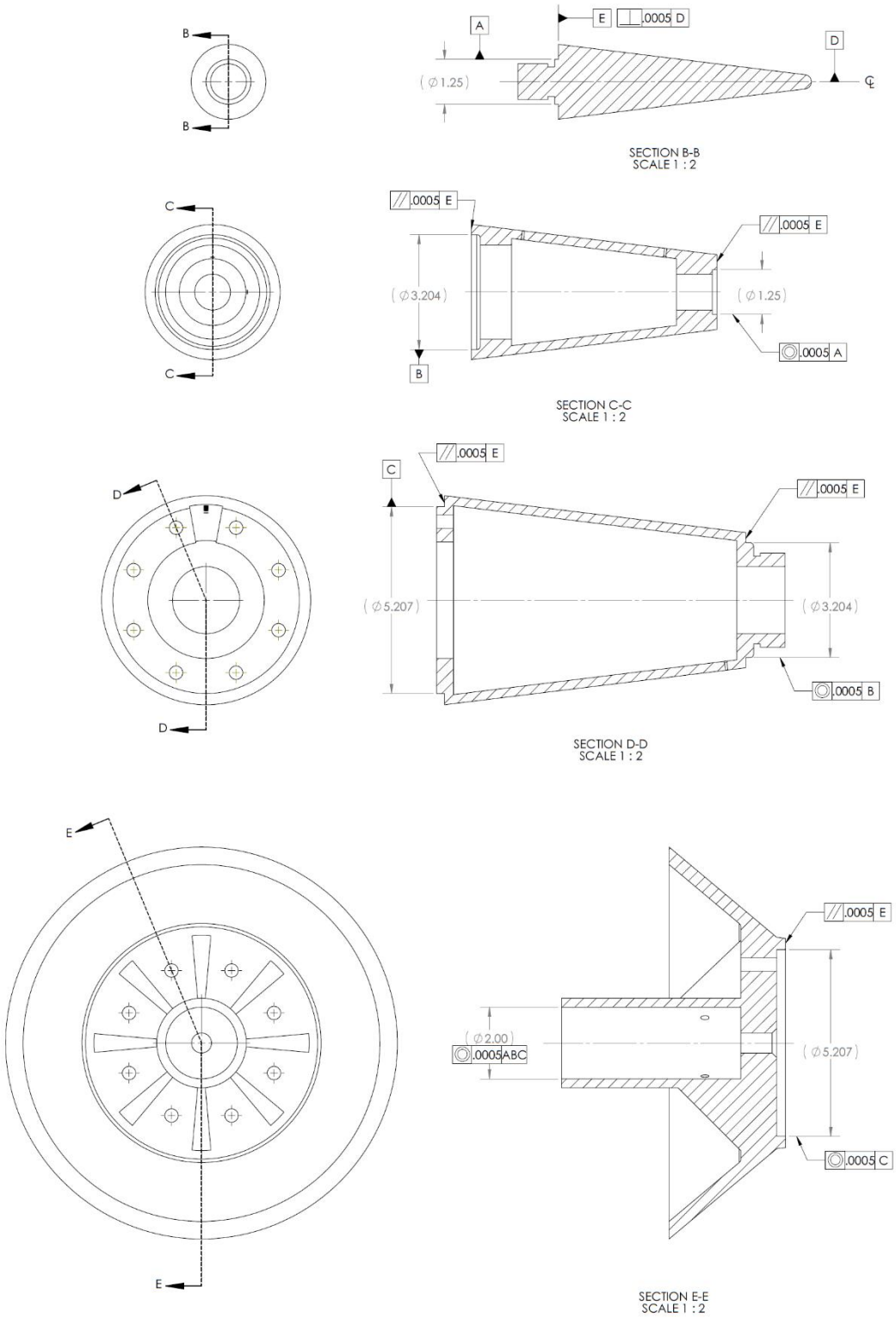

Figure 16. Cone/Flare Model Detail (5.1mm Radius Tip, 40° Flare Shown) (dimensions in inches)

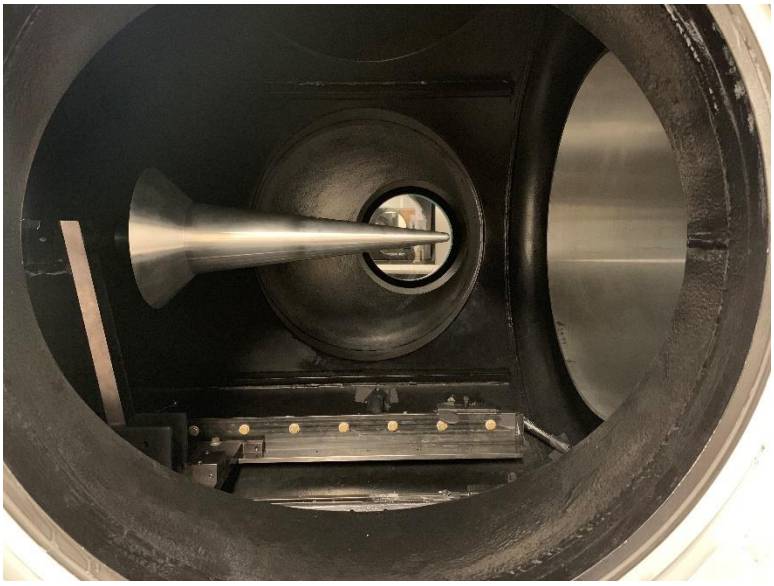

Figure 17. Model positioned in test section (43° base and 10.2mm tip installed)

A Photron Fastcam SA-Z high-speed camera with a Nikon 80-200mm telephoto lens captured the images. The Fastcam provides multiple input/output options including an external trigger. A BNC cable linked the camera to the tunnel's data acquisition system, allowing the camera to be triggered by the initial shock during a run. The camera was controlled with Photron's Fastcam Viewer (PFV) software. After a series of trial runs to find optimal settings, the camera was set to record 20,000 frames per second at 1,024 x 1,024 pixels with a shutter speed of 1/998000 seconds. Under those conditions, the camera's on-board storage allowed for one second of video to be recorded. This constraint was not a limiting factor considering the approximately 200ms run time of the Ludwieg Tube. The PFV software was setup with a custom manual trigger setting, saving 250ms before the trigger and 750ms after the trigger. Recording before the trigger point was necessary, as the trigger signal would occasionally come after the starting shock if

the initial test section vacuum was not low enough. After each run, the frames were cropped to only include startup and the first 100ms period of quasi-steady flow. In order to reduce storage space, the image was also cropped to only include the relevant portion of the frame. PFV allows the user to set custom measurements for the image. For the cone/flare tests, an aluminum block of known length was held against the cone frustum. Inputting the block length in PFV's measurement tool led to a direct calibration of the image to real-world dimensions.

Post-processing was mostly performed with ImageJ, an open platform image processing and analysis program. Before importing the video files to ImageJ, the startup and shutdown portions of each video were cropped in PFV so that only the steady-flow portions were included. The videos were imported as stacks of images ranging from 150 to 1500 frames depending on the useable runtime of each test. Built-in tools in ImageJ were used to compile single images from each stack showing the average intensity of each pixel and the standard deviation of pixel intensity during the run. The calibration of length-per-pixel carried over from PFV, so measurements could be performed on the compiled images using ImageJ's built-in measurement tools. This function enabled shock angle and recirculation region locations to be quantified. The standard deviation of image intensity during a run was used to identify regions of high fluctuations, namely, shock waves and turbulent boundary layers. Identifying these regions allowed for assessment of turbulence development and shock motion. ImageJ also includes tools for tracking the time history of image intensity, which was used to characterize shock and boundary layer oscillation frequency.

Table 2. Schlieren Test Equipment

Schlieren Test Equipment	
Light Source	
Model:	Newport 66921
Serial Number:	30012
Bulb:	SXB10004
Light Source Power Supply	
Model:	Oriel OPS-A1000
Serial Number:	80412
High Speed Camera	
Model:	Photron Fastcam SA-Z
Serial Number:	10202416196
Lens:	Nikon Nikkor 80-200mm 1:2.8D

Summary

The design and operation of the AFRL Ludwieg tube facility was described in the first section. This description included driver tube and test section sizing, fast-valve operation, control methods, and data acquisition equipment. Freestream Reynolds number calculation and a breakdown of a typical run pressure trace were discussed. The second section described the setup of the Schlieren system used during the testing herein. Geometry and construction of the tested cone/flare model were also covered.

IV. Analysis and Results

Chapter Overview

Results and analysis from the tunnel characterization study and the Schlieren testing are presented in this chapter. The first section covers a brief description of the tunnel characterization testing equipment, overview of the findings, and Schlieren imaging of a Pitot probe used in the survey. The bulk of the chapter focuses on the high-speed Schlieren imaging of the variable-geometry cone/flare model. First, observations of the four different cone tips of varying radius are presented along with symmetry measurements of the upper and lower bow shocks. In addition, downstream measurements of the bow shock angles are used to verify Mach 6 flow from the Ludwieg tube nozzle. Next, observations of the shock-wave/boundary-layer interaction region at the cone/flare junction are presented for all tested model geometries. Analysis is performed on the boundary layer separation and reattachment points measured based on the SBLI observations for varying geometries and flow conditions. These results are compared to those of a previous study on the same model in the AFRL Ludwieg tube facility. Finally, analysis is performed on unsteady shock motion that was present with laminar upstream boundary layers.

Tunnel Characterization

The Schlieren system was setup while AFRL engineers were performing tunnel characterization using a Pitot probe rake. The 30-inch diameter rake, shown in Figure 18, housed twelve Kulite pressure transducers spaced 1.275 inches apart to allow for sampling across the diameter of the test section. To characterize the core flow from the

Ludwieg tube, the rake was rotated in 45-degree increments until a 360-degree flow profile could be generated from interpolation during post-processing of the data. The survey was performed at multiple positions downstream of the nozzle, over the length of travel allowed by the sting base. Data collection was limited due to reliability issues with the pressure transducers. As a result of sensor failure, data points for generating an accurate contour plot were only collected at the rearmost sting position in the Ludwieg tube test section. At this sting position, the leading tip of each Pitot probe was 815mm downstream of the nozzle exit plane. This direction is considered the x-axis of the test section. The notable takeaway from the tunnel characterization analysis is that the nominal Mach 6 core flow cross section is about 400mm to 470mm in diameter at the x=815mm position. The 43° flare, the widest base for the cone/flare model tested in the next section, is roughly 280mm in diameter. Considering a core flow diameter of 400mm, the 43° flare blocks about 49% of the core flow cross section.

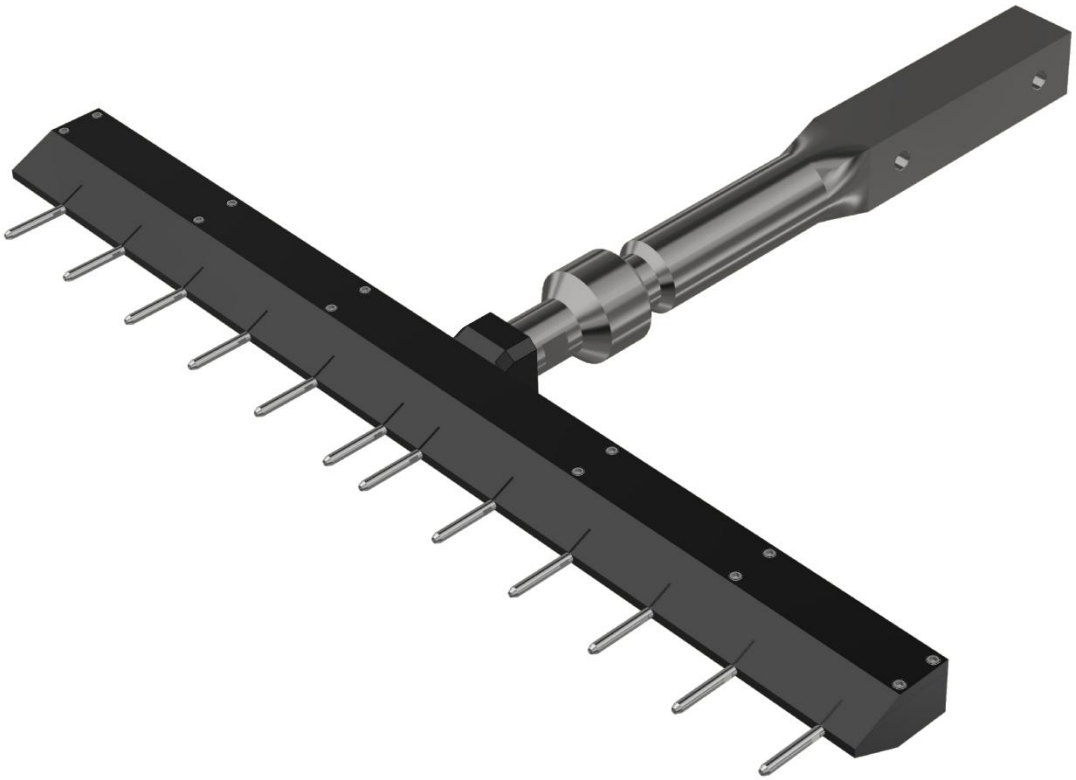

Figure 18. Pitot Rake Rendering

Raw pressure measurements were converted to Mach number using a MATLAB script developed by AFRL engineers. Static pressure data was taken from a pressure transducer located at the nozzle entrance. The script was used to produce Figure 19 through Figure 21, provided by AFRL engineers. An internal AFRL report provides further detail and analysis of the collected data. Measurements from 52 runs at varying driver tube pressures were used to characterize flow at the x=815mm position. Figure 19 provides a contour plot of the cross-section Mach numbers interpolated between Pitot probe data points, which are represented by red asterisks. The y and z axes represent the horizontal and vertical axes of the test section, respectively. A dashed circle is plotted at r=200mm to represent the conservative estimate of the core flow region. The average

Mach number in this region was calculated at 6.14 based on the Pitot probe measurements. A lower Mach number region (dark blue) in the northwest quadrant of the core region appears to mirror a higher Mach number region (light blue) in the southeast quadrant of the core region. Due to underrepresented regions caused by failed sensors, it is unclear if this phenomenon is a true representation of flow inside the test section, or a function of interpolating across a large region.

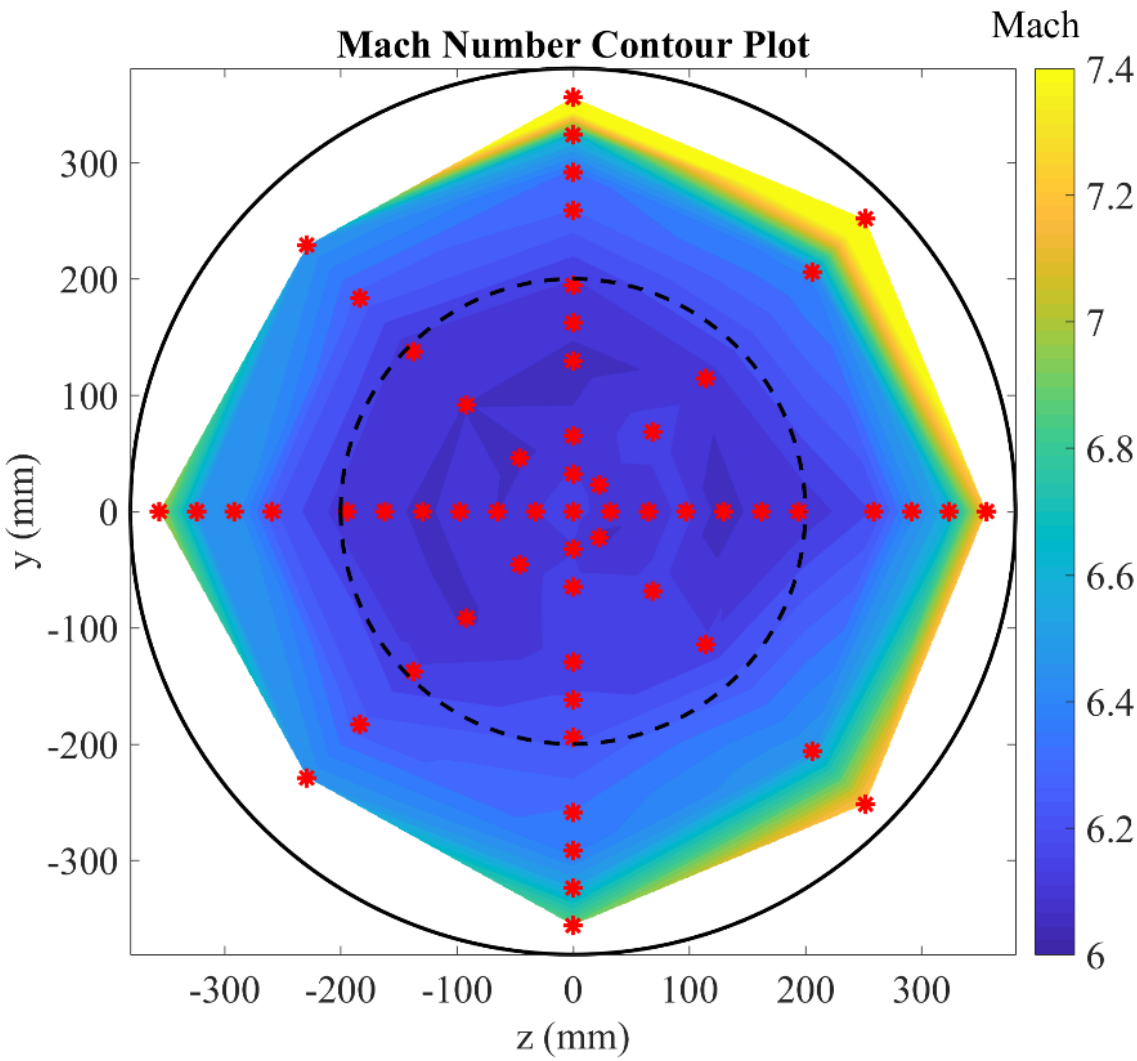

Figure 19. Mach Number Contour Plot (x=815mm)

Figure 20 shows individual Mach number measurements across the Pitot rake at the horizontal position. The horizontal position includes data from the 0º and 180° rake orientations, as the Pitot probes were staggered to provide maximum resolution. Average Mach numbers for each sensor location are represented by circles. This figure clearly shows the consistent average Mach number across the 200mm radius core flow region. A horizontal line is plotted at a Mach number of 6.14 to represent the core flow average.

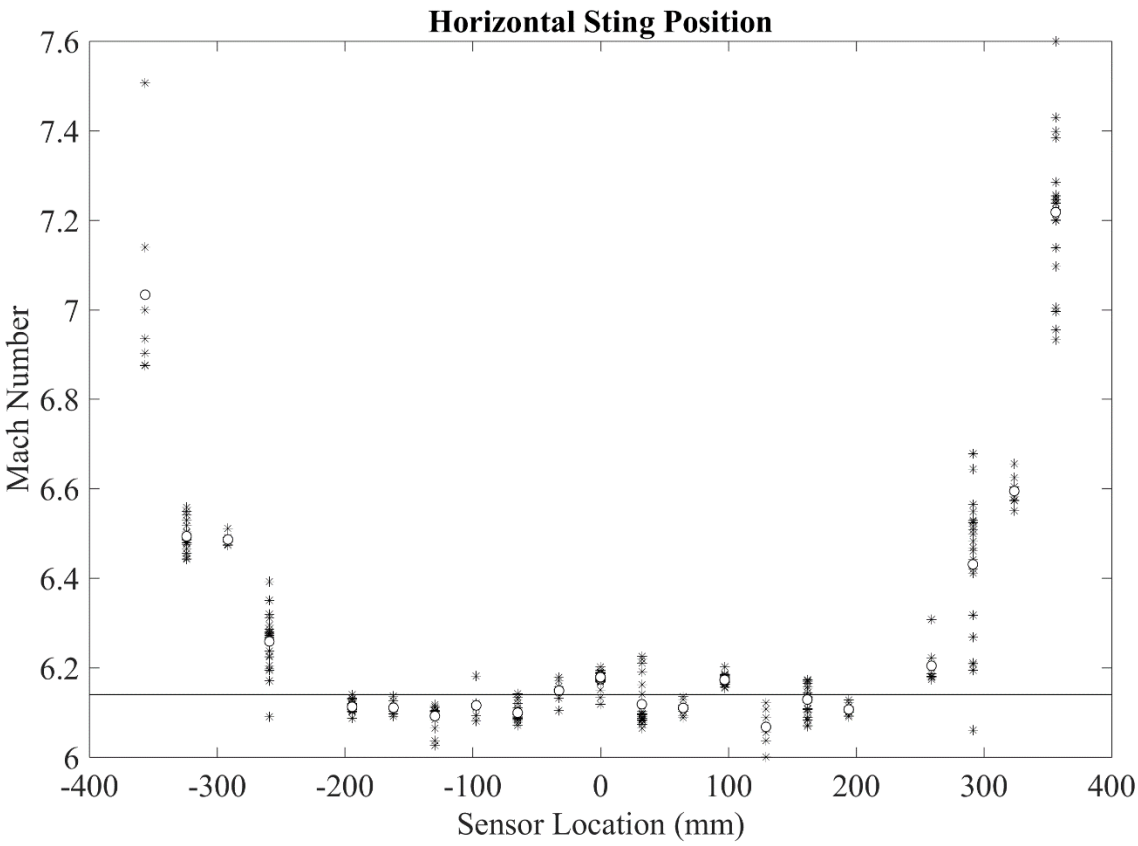

Figure 20. Mach Number Measurements Across the Horizontal Sting Position (x=815mm)

Similarly, Figure 21 shows measurement noise from the data collected across the Pitot rake at the horizontal orientation. Average noise percentages for each sensor position are represented by red diamonds. Inside the 200mm radius core region, average percent noise remains low, with a maximum value under two percent. Outside the core flow region, noise percentage increases as flow becomes turbulent at the perimeter of the test section.

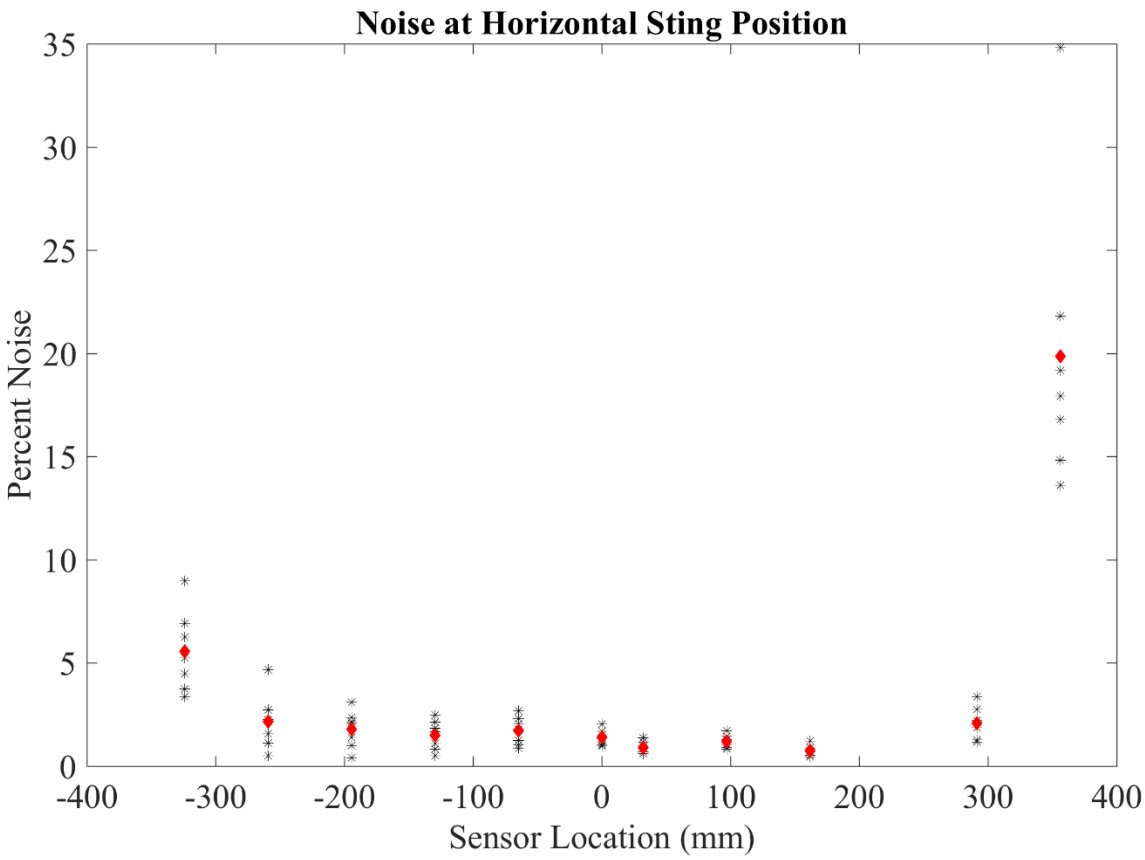

Figure 21. Measurement Noise Across the Horizontal Sting Position (x=815mm)

A series of Schlieren images were collected when the sting was set to its maximum upstream position with the rake set vertical. This positioning placed the Pitot probes at the center of the test-section viewing window. Pressure data saved by the Ludwieg tube data acquisition and video recorded by the high-speed camera used in the Schlieren system recorded the time the trigger signal was sent at tunnel startup. The presence of the trigger point allowed for Schlieren images to be synced to pressure data from the Pitot rake. Figure 22 shows the pressure trace from the B screen Kulite high temperature pressure transducer shown in Figure 23. Frame A in Figure 22 shows the entire run, from startup until shutdown. Frame B shows the same pressure data with a focus on the startup period, just after the trigger signal. Figure 23 shows Schlieren frames synchronized to the lettered points in the previous figure. For this run, the normal startup shock is not visible. However, after the normal shock passes and flow from the driver tube begins, bow shocks are seen off the Pitot probes. The normal shock induced by the flat face of the Pitot rake can also be seen to the left of each frame. As pressure increases, contrast between the pre-shock and post-shock regions increases as the shock waves themselves become darker. This increasing contrast indicates strengthening pressure gradients.

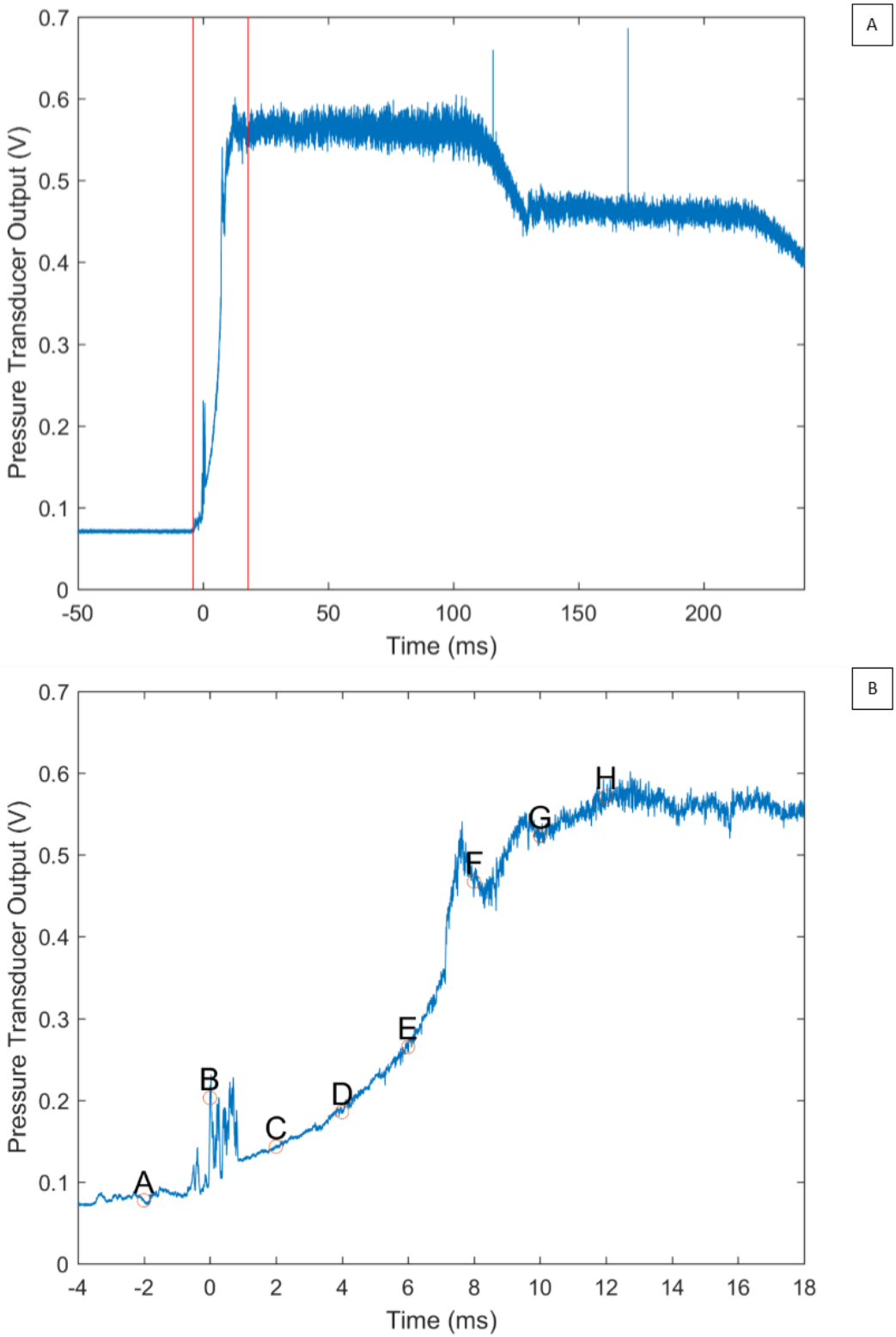

Figure 22. Pressure Trace

(Top): Full Run, Vertical Lines are Limits of Frame B (Bottom): Points During Startup

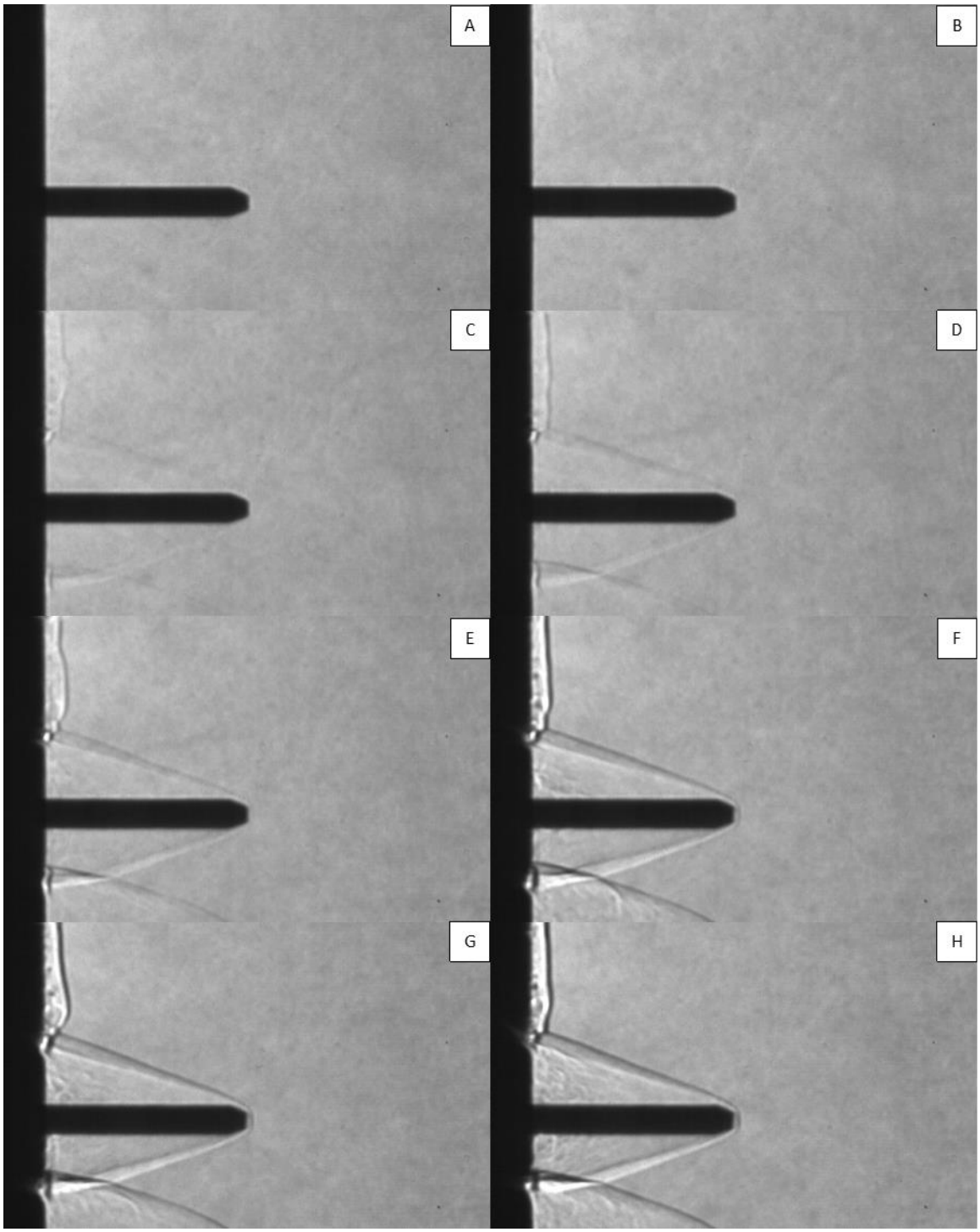

Figure 23. Startup Schlieren (2ms time steps)

Cone/Flare Schlieren Results

Identical runs were performed on the cone/flare model with the Schlieren knife edge set vertical and horizontal. Generally, when setting up a Schlieren system, the knife edge should be oriented so that it is parallel with the plane of interest to show the most relevant information. For the cone/flare model testing, a horizontal configuration provided better results for analysis because it was nearer to parallel with the frustum of the 7° half-angle cone. The horizontal knife edge runs showed sharper contrast in the boundary layer, shock, and recirculation regions than the vertical knife edge runs, as demonstrated in Figure 24. Additionally, the horizontal runs showed less optical distortion than the vertical runs. Figure 25 shows an example of the distortion observed with the vertical knife edge configuration. The circular cross-section of the flared base caused light to refract and effectively wrap around the silhouette of the flare, obscuring the edge of the model. This distortion meant the vertical knife edge runs were not useful for measuring the recirculation region. However, they may have some utility for visualizing the region of flow on the flare portion of the model. The refraction would not have been present in a wide wedge-shaped model. Runs with the 40° and 43° flares were cut short due to blockage issues. In order to capture the cone/flare transition in frame, the model was placed in the maximum forward position allowed by the sting. The wide flares were close enough to the nozzle exit to prevent a full 100ms steady-flow period. This phenomenon is known as “unstart.” The unstart was likely due to a combination of the larger physical diameter of the wide flares and larger resulting bow shock diameter. Useful runtimes for the 40° and 43° flares averaged about 25ms.

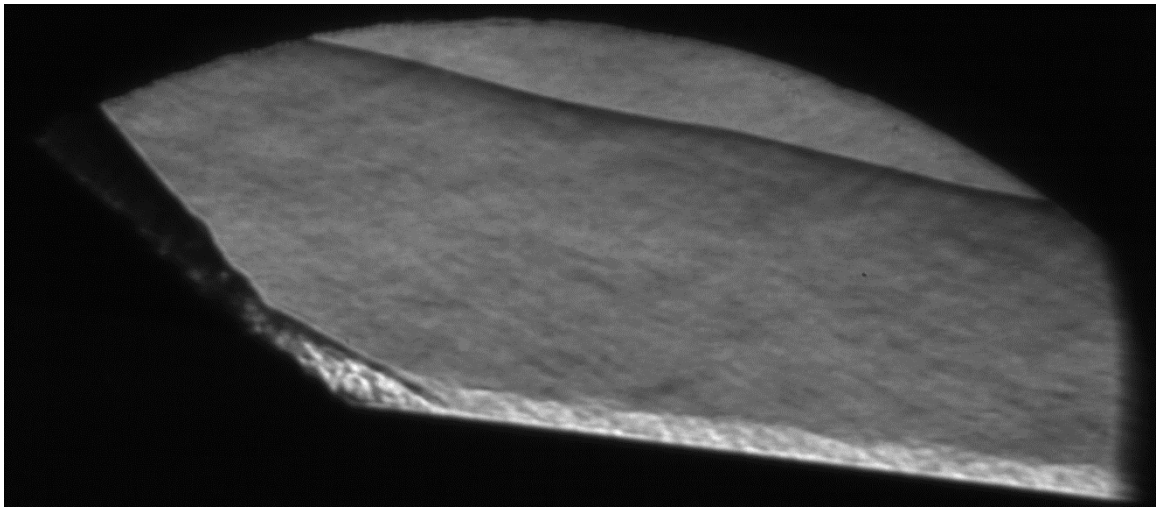

Figure 24. Horizontal Knife Edge Example

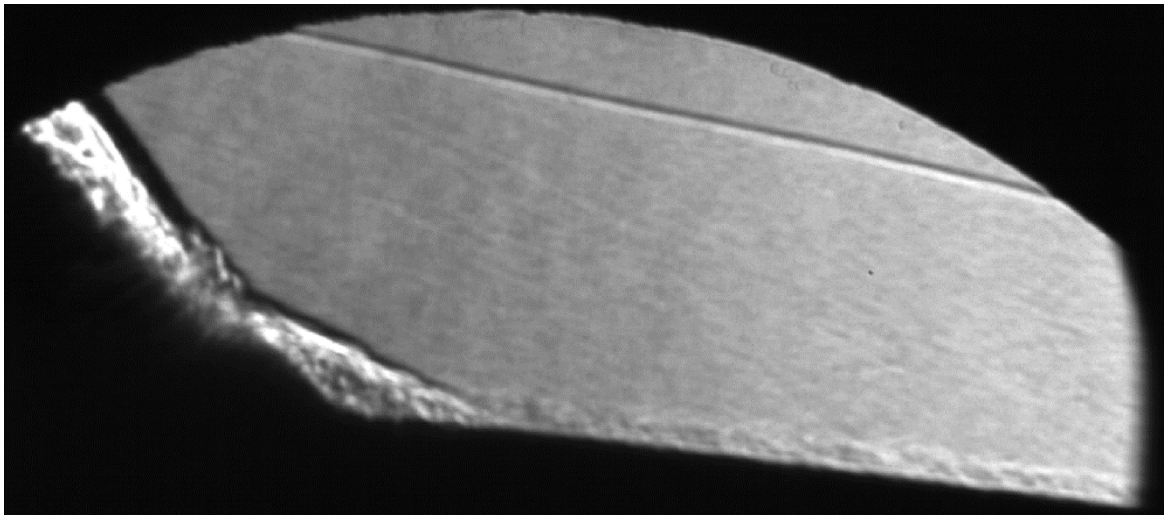

Figure 25. Vertical Knife Edge Example

Advantages of the horizontal knife edge and the implications of the distortion with the vertical knife edge are demonstrated in Figure 26. The bow shock, boundary layer, and recirculation region are clearly defined in the first image. These structures are still present in the second image. However, they are less clear, and the reattachment point is obscured by the optical distortion. The vertical knife edge provides more fidelity in the

reattachment shock and boundary layer region that grows along the flared portion of the model because the flare is closer to vertical than the frustum.

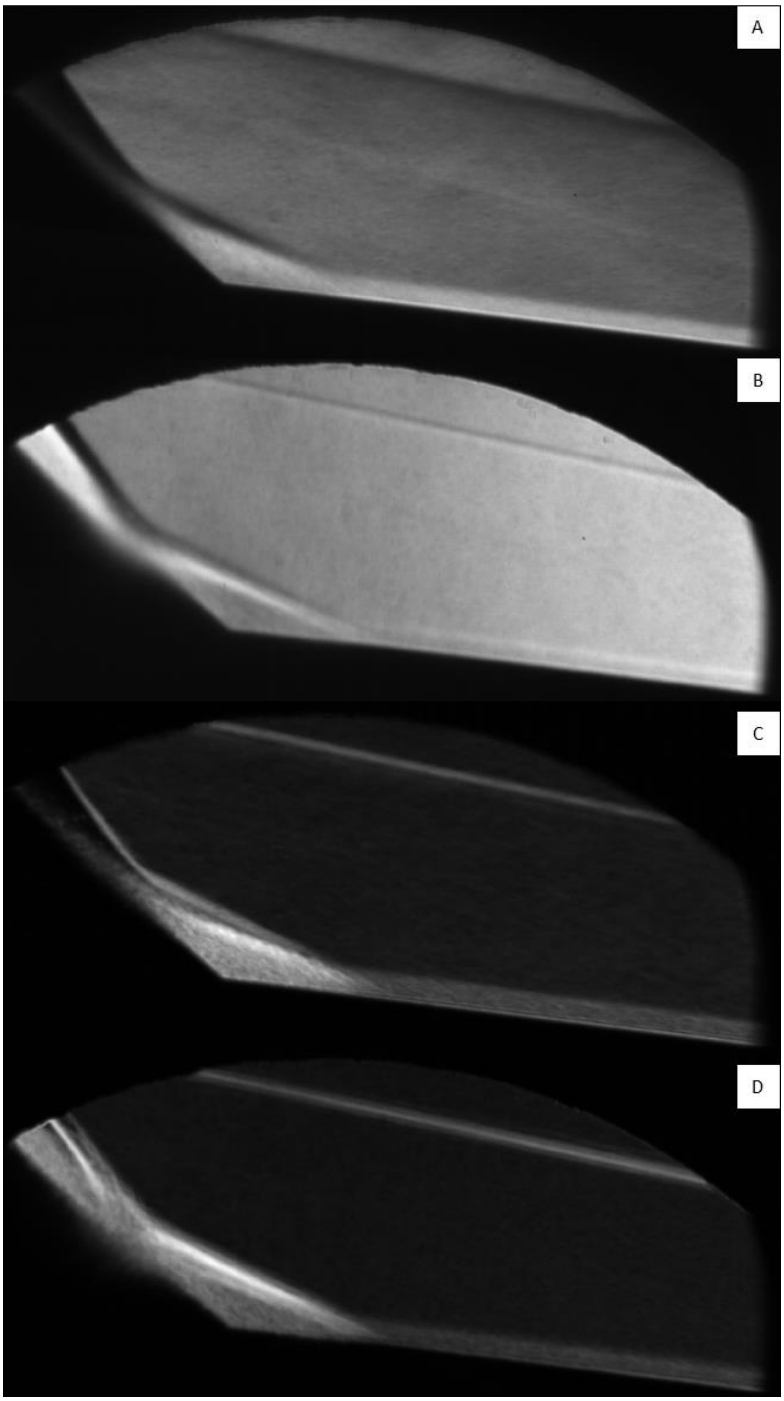

Figure 26. Horizontal versus vertical knife edge on 43° base with 0.0mm tip.
(A): Averaged, horizontal (B): Averaged, vertical (C): Std dev, horizontal (D): Std dev, vertical

Cone Tip Observations

The model was positioned so that the cone tip would be in line with the Ludwieg tube viewing windows. Averaged Schlieren images show clearly defined bow shocks off the four tip configurations. The blunt tips in Figure 30 show especially strong shocks due to flow stagnation at the tip centerline causing normal shocks ahead of the centerline of the body. The normal portion of these shocks generated a strong entropy layer which continued to the cone/flare junction in many cases. Boundary layers are too thin to be visible in the limited frame area meaning any laminar-to-turbulent transition which may be present cannot be identified with the Schlieren system as it was configured. Conclusions about the general boundary layer state for each configuration (turbulent for sharp tips and laminar for blunt tips) are therefore drawn from the research performed by Running et al., who were able to capture much more of the model surface area in their infrared thermography testing. [23] The cone tip runs were performed with a horizontal knife edge. This configuration is responsible for the apparent dark/light inversion in the post-shock regions above and below the cone. For these runs, the primary difference between the 200psi and 400psi stagnation pressures is the contrast between regions. The higher contrast for the 400psi runs indicates a greater change in density across the bow shocks.

For runs with the sharp tips installed, the model was observed rising relative to the camera about 0.5mm between the resting state and in fully developed Mach 6 flow. The consistent positive rise would indicate the model was installed at a slightly positive angle of attack. The movement was allowed by the machining tolerances between the flare base and the Ludwieg tube sting. At 760mm overall length for the cone/flare model,

a tip rise of 0.5mm means a positive change in angle of attack of 0.038 degrees. This small change is well within the 0.1° error range of the methods used for measuring shock angles and can therefore be considered negligible for many circumstances.

Using the averaged images in ImageJ, lines were projected along the upper and lower cone surfaces and their corresponding bow shocks. Figure 27 provides an example of the projected lines. This technique was used to ensure the origins of the upper and lower bow shock measurements started at the same point. A line intensity plot from ImageJ of the vertical line in Figure 27 is shown in Figure 28. Intersections between the vertical line and shock waves/model edges are marked with black asterisks. Plotting line intensity was the most precise method available for locating the boundaries of regions of interest. Distance in the plot (x-axis) is measured in pixels from the bottom of the image. Region boundaries (asterisks) were marked at the midpoint of steep y-axis slopes, which correspond to sharp changes in pixel brightness. The line intensity plots aided in locating suitable starting points for the line projections. It is worth noting the angle measurement tool in ImageJ has a measurement error of about 0.1 degree.

Measurement results are presented in Table 3. For this table, the measured angles are between the shock and the corresponding cone face, not the cone centerline. Lower bow shock angles were only recorded for the 200psi runs. There was not enough contrast between the black cone silhouette and the dark boundary layer on the underside of the cone at 400psi to confidently determine the location of the cone surface. The dark boundary layer is due to the light/dark inversion from the horizontal knife edge brought about by the density gradient. The sharper contrasts induced by higher stagnation pressures meant the upper boundary layers got brighter while the lower boundary layers

got darker. Based on the measurements obtained from the 200psi runs, the average difference between the upper and lower shock angles is 0.39 degrees. At a positive angle of attack, upper bow shock angles are expected to increase, while lower bow shock angles are expected to decrease. Based on this trend, the angle of attack of the cone/flare model can be estimated at half of the difference between angles, or about 0.20 degrees. The effects of this non-zero angle of attack were observed by Running et al. during infrared thermography testing. [23] They found asymmetric heating contours on the upper and lower surfaces of the cone frustum. Analysis of the level of asymmetry revealed the variations in pitch and yaw of the model, relative to the freestream, were within ± 1° of normal orientation. [23] The severity of the impact of having a non-zero angle of attack depends on the type of testing being performed and the goal of the research.

Table 3. Upper Versus Lower Bow Shock Angles

Tip Radius (mm)	Stagnation Pressure (psi)	Upper Shock Angle (°)	Lower Shock Angle (°)	Difference (°)
0.0	200	5.98	5.53	0.45
	400	5.85		
0.5	200	5.91	5.59	0.32
	400	5.71		
	Average:	5.86	5.56	0.39

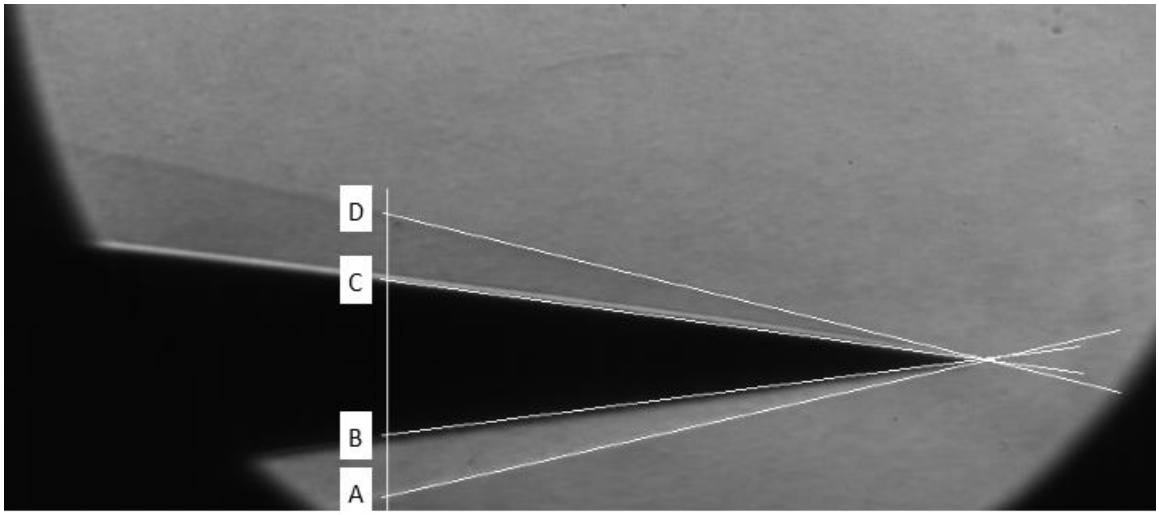

Figure 27. Projected edges (0.0mm tip, 200psi)

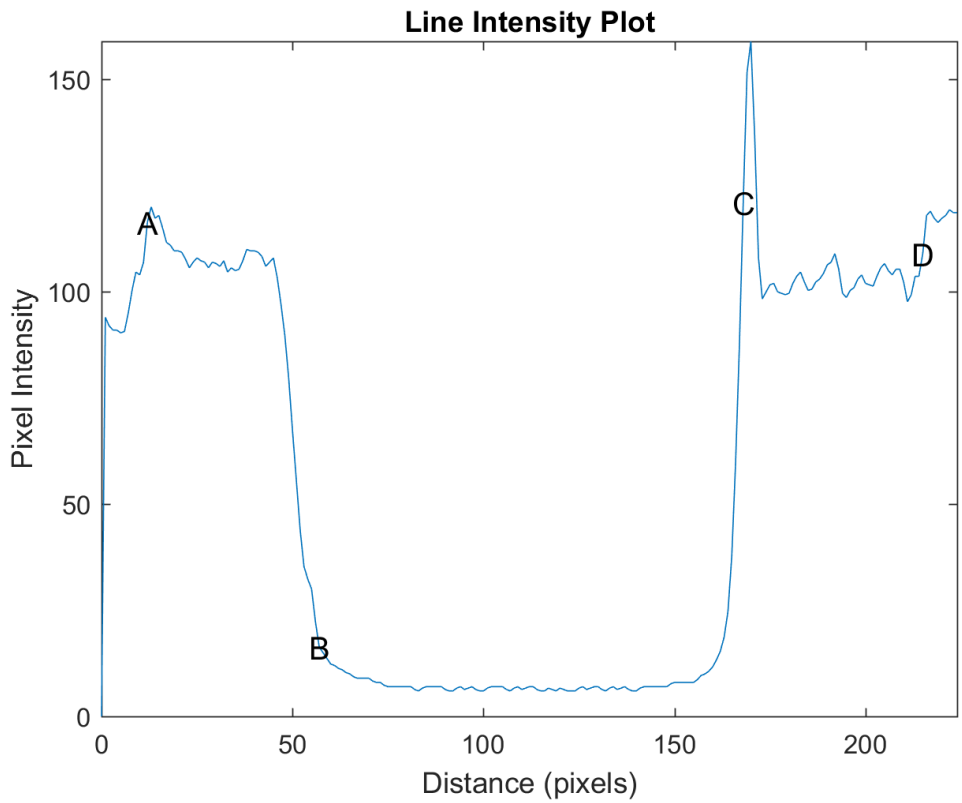

Figure 28. Line Intensity Plot

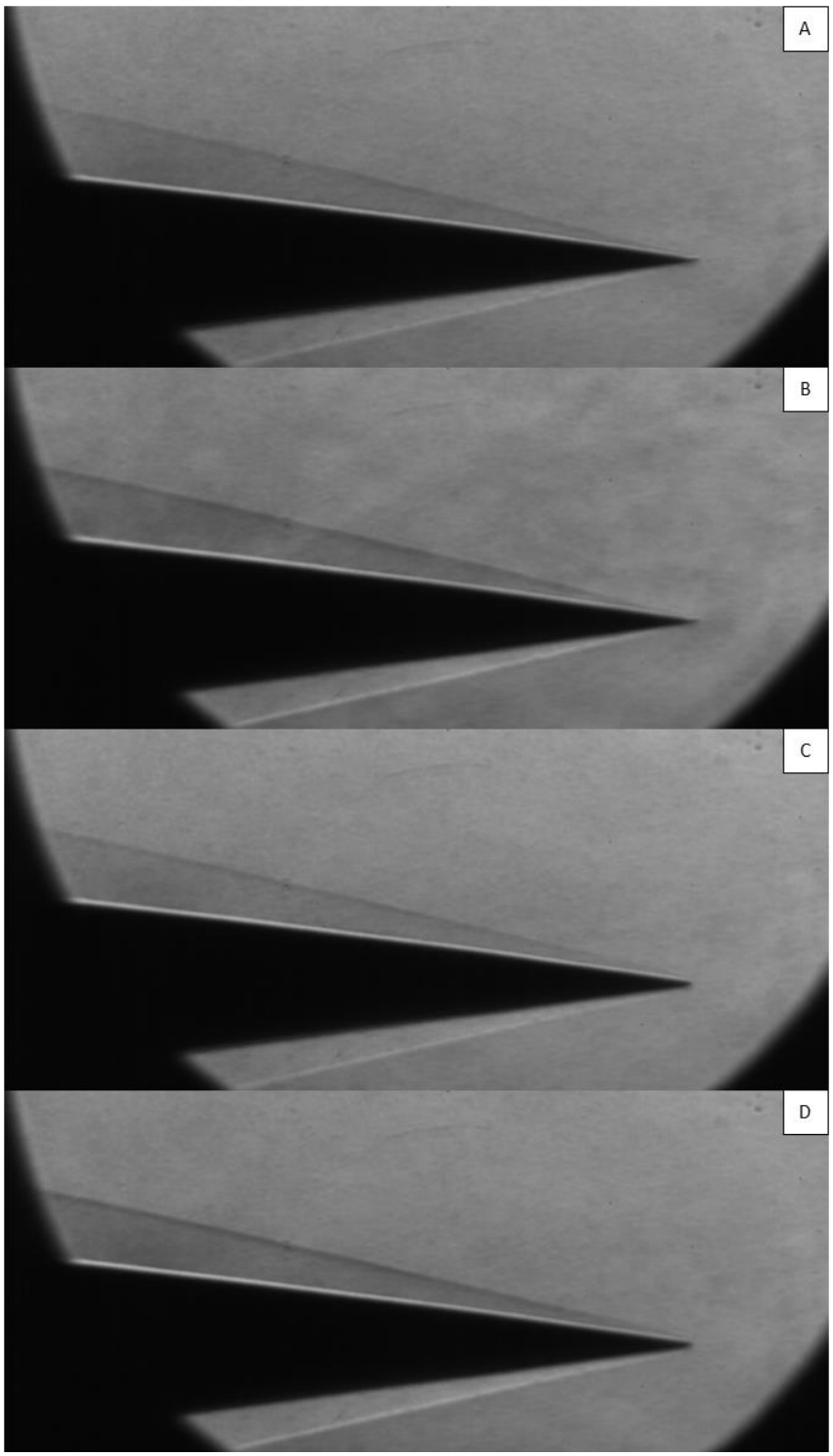

Figure 29. Sharp tips (averaged)

(A): Sharp tip, 200psi (B): Sharp tip, 400psi (C): 0.5mm tip, 200psi (D): 0.5mm tip, 400psi

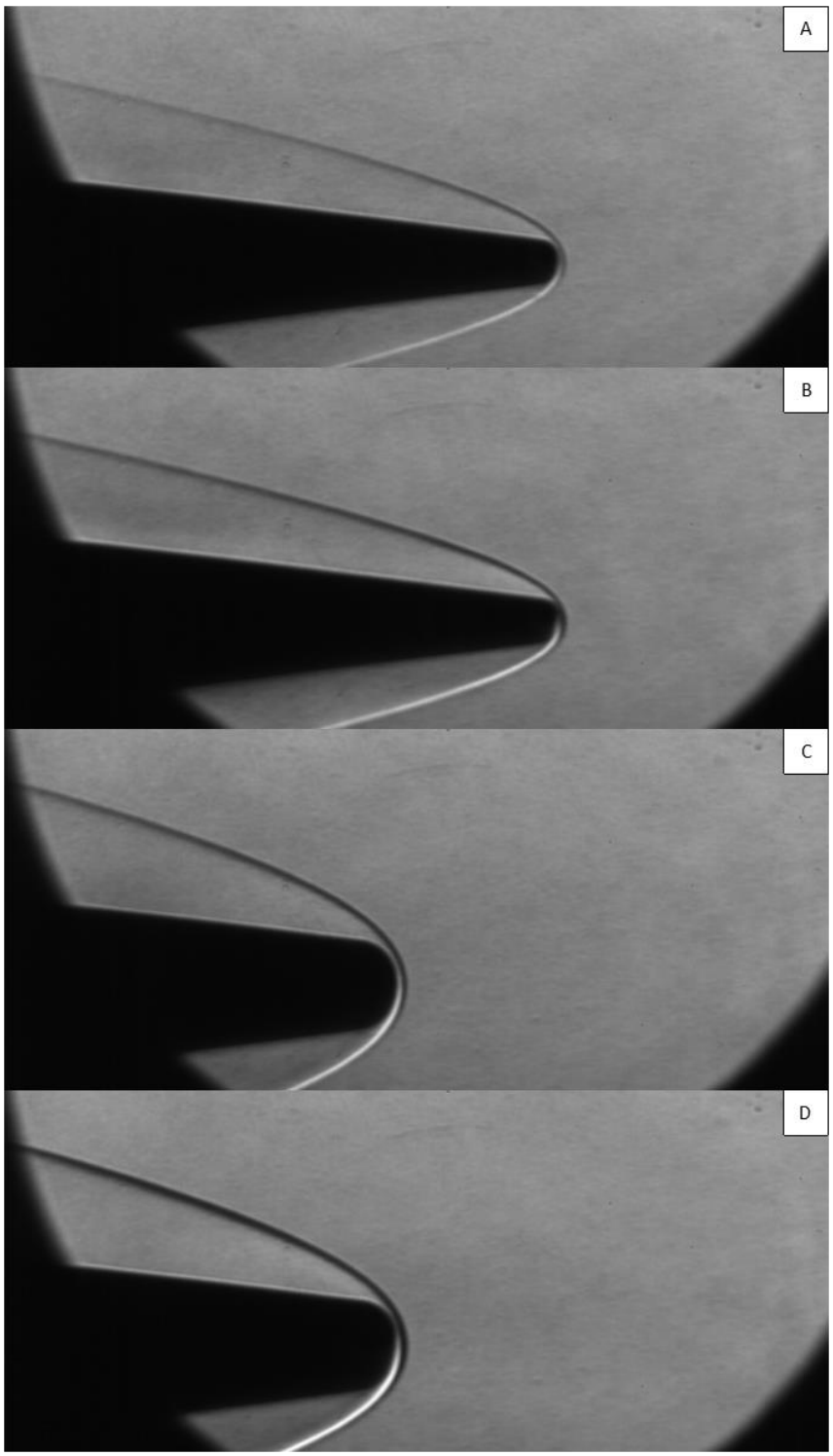

Figure 30. Blunt tips (averaged)

(A): 5.1mm tip, 200psi (B): 5.1mm tip, 400psi (C): 10.2mm tip, 200psi (D): 10.2mm tip, 400psi

The cone tips in Figure 29 and Figure 30 were tested on the 34° flare base. With this base, steady behavior was present over the entire 100ms quasi-steady flow period. The blunt 5.1mm and 10.2mm tips were tested on the 43° flare base as well. Separation was visible only with the 5.1mm radius tip, shown in Figure 31. On five different occasions during the 100ms quasi-steady flow period, the separation moves upstream enough to be visible in the frame, eventually reaching the cone tip. The separation shock can be seen interacting with the bow shock in frames C through H. After frame H, the separation moves back downstream and out of the frame.

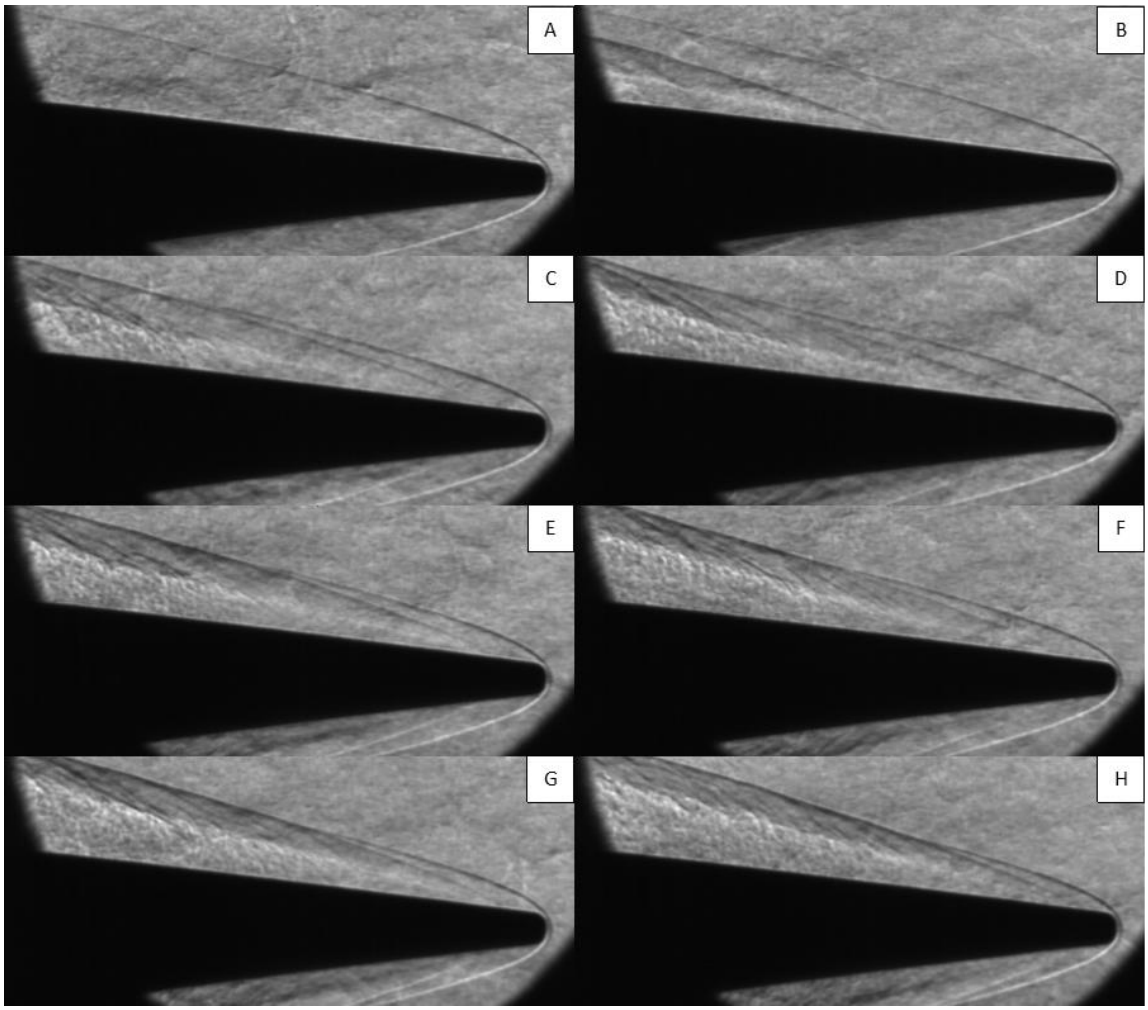

Figure 31. Separation at cone tip (0.5ms time steps)

Bow Shock Measurement

With the model positioned so that the cone/flare junction was centered on the viewing window, a portion of the oblique bow shock was captured at the top of the Schlieren image frame, as shown in Figure 32. The visible bow shocks presented an opportunity to compare analytical predictions to experimental results. Angle measurements were performed in the ImageJ software on the averaged images for the 400psi runs with a horizontal knife edge. This set of runs served as the baseline for all analysis performed due to the high contrast between flow regions. The high-speed camera was confirmed to be level relative to the model within the 0.1° angle measurement error of the ImageJ measuring tool by confirming the cone frustrum could be measured at 7°. A Taylor-Maccoll solution application was used to predict the bow shock angle from a 7° half-angle cone in a Mach 6.0 and 6.1 flow. [25] The Taylor-Maccoll equation is an indirect method for finding the oblique bow shock angle for a cone in a given freestream Mach number. The method uses an ordinary differential equation, shown is Equation 6, which is solved numerically for the given freestream Mach number and an assumed shock angle for an inviscid, irrotational flow.

$$\frac{\gamma-1}{2}\left[V_{max}^2 - V_r^2 - \left(\frac{dV_r}{d\theta}\right)^2\right]\left[2V_r + \frac{dV_r}{d\theta}cot\theta + \frac{d^2V_r}{d\theta^2}\right] - \frac{dV_r}{d\theta}\left[V_r\frac{dV_r}{d\theta} + \frac{dV_r}{d\theta}\left(\frac{d^2V_r}{d\theta^2}\right)\right] = 0 \tag{6}$$

Where:

γ = Ratio of specific heats
V_{max} = Maximum theoretical velocity
V_r = Radial component of velocity
θ = Shock wave angle

The Taylor-Maccoll equation needs to be solved incrementally using a solution technique like the Runge-Kutta method to work toward a solution for the cone angle. As the method is indirect, the chosen shock angle needs to be adjusted until the solution provides the desired cone angle. The theory assumes the cone geometry incorporates a sharp tip and has an infinite length. [26] Assuming a freestream Mach number of 6.0 and a 7° half-angle cone, Taylor-Maccoll theory predicts a bow shock angle of 11.94° relative to the freestream. This result agrees strongly with the measured angles summarized in Table 4. For the sharp cone tips at all flare angles, the measured difference for the bow shock angle was less than one tenth of a degree. Varying gamma, the ratio of specific heats, from room temperature to driver tube temperature had a negligible effect on the predicted bow shock angles.

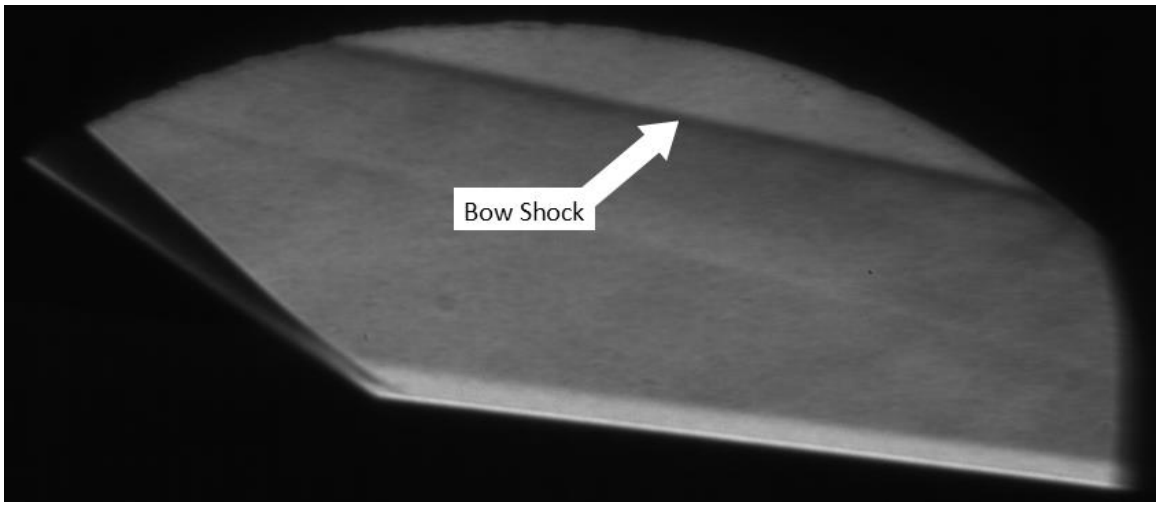

Figure 32. Bow Shock Location

A normal shock will be present at the nose of a cone with a blunt tip in a hypersonic flow due to a subsonic boundary layer behind the shock. The presence of the normal shock, and therefore a substantial entropy layer, means the following oblique portion of the shock will have a different angle from what is predicted by Taylor-Maccoll

theory. When the 5.1mm radius tip was attached to the cone/flare model, the measured oblique portion of the bow shock angle was between 0.48 and 0.89 degrees shallower than predicted. This discrepancy is demonstrated by the inaccurate Mach number predictions in the gray cells in Table 4. The radial distance between the model surface and the bow shock also increased with the blunt tip due to the presence of the normal shock. Normal shock angles are closer to perpendicular to the freestream than oblique shock angles. In the case of the cone, this angle means the shock travels radially outwards before being turned to an oblique angle by the incoming freestream flow. This behavior is visible when comparing Figure 29 and Figure 30 above. The net result is a bow shock with a greater radial diameter downstream with the blunt cone tips. The bow shock diameter was large enough for the 10.2mm radius tip that the shock was not visible in the Schlieren frame. Based on the measured bow shock angle of the 5.1mm tip compared to the predicted value, one would expect the bow shock angle to be even shallower for the 10.2mm tip.

The Taylor-Maccoll equation could also be used to back out a Mach number corresponding to a provided cone half-angle and measured bow-shock angle. The resulting Mach numbers were calculated in the same Taylor-Maccoll solver used previously and are presented in the right column of Table 4. The 0.0mm radius tip is the truest to the assumptions made in Taylor-Maccoll theory and therefore provides the most accurate results. For the 0.0mm radius tip cases, the solutions are very close to expected, with an average Mach number of 6.0. As previously stated, corresponding Mach values are higher for the 5.1mm radius tip cases because a flatter bow shock would normally indicate a higher freestream Mach number with a sharp cone tip. Based on the tunnel

characterization study, using a freestream Mach number of 6.1 results in a predicted bow shock angle of 11.82°, which is further from the measured average than the Mach 6.0 prediction. However, the difference in angles is effectively within the 0.1° measurement error of the ImageJ angle measurement tool. Additionally, the observed slight positive angle of attack of the cone/flare model may be responsible for measured bow shock angles trending slightly larger than expected for a true Mach 6.1 core flow.

Table 4. Bow Shock Angles

(Greyed cells corresponding to the blunt cone tip are not representative for Taylor-Maccoll theory)

Flare Angle (°)	Tip Radius (mm)	Bow-Shock Angle (°)	Difference from M=6.0 (°)	Corresponding Mach Number
34	**0.0**	11.86	-0.08	6.07
	0.5	11.91	-0.03	6.02
	5.1	11.46	-0.48	6.4
37	**0.0**	12.00	0.06	5.95
	0.5	11.94	0	6.00
	5.1	11.23	-0.71	6.69
40	**0.0**	11.95	0.01	5.99
	0.5	11.99	0.05	5.95
	5.1	11.37	-0.57	6.54
43	**0.0**	11.95	0.01	5.99
	0.5	12.02	0.08	5.93
	5.1	11.05	-0.89	6.90
Taylor-Maccoll (M=6.0, γ=1.4)		**11.94**		
Taylor-Maccoll (M=6.1, γ=1.4)		**11.82**	-0.12	

Shock/Boundary Layer Observations

The primary objective for the Schlieren testing was to document shock and boundary layer behavior at the cone/flare junction on the model. Varying the radius of the cone tip provided a method for adjusting the boundary layer over the model. Similarly, varying the flare angle provided a way to adjust the intensity of the adverse pressure gradient at the cone/flare junction. The effects of changing the flare angle are demonstrated in Figure 33. Increasing the flare angle increases the adverse pressure gradient, resulting in a larger separation region at the junction while maintaining a constant cone tip radius. Boundary layer thickness and bow shock location remain largely unchanged.

Figure 34 through Figure 41 compare average intensity and standard deviation when varying cone tips at a constant flare angle and stagnation pressure. Note that stagnation pressures of 200psi and 400psi generate freestream Reynolds numbers of $10.0 \cdot 10^6$ and $19.8 \cdot 10^6$ per meter, respectively. Tests in these figures were performed with a horizontal knife edge. Figure 50 through Figure 73 in the appendix show similar comparisons with different stagnation pressures and knife edge configurations. Average intensity images present the strength of the density gradient between regions. Standard deviation images highlight regions with a high degree of movement with lighter pixels. For this set of tests, the light areas correspond to shocks and regions with highly turbulent flow such as turbulent boundary layers and inside the recirculation regions.

Figure 34 and Figure 35 show averaged intensities and standard deviation for the 34° flare respectively. Recirculation region area clearly grows as tip bluntness is increased. The standard deviation images for the blunt tips highlight the separation shock

locations, whereas the shock locations are obscured in the noise of the averaged images. For the 37° flare, the recirculation region grows in Figure 36 and Figure 37 relative to the images for the 34° flare. Movement of the separation shock increases for the 10.2mm radius tip run based on the increased bright area in the recirculation region in frame D of Figure 37. Separation boundaries for the sharp tip runs remain clearly defined in Figure 38 and Figure 39, which show the 40° flare. However, recirculation regions for the blunt tip runs become more obscure as light and dark regions develop for the averaged and standard deviation images. Figure 40 and Figure 41 continue this trend with images of the 43° flare. The recirculation region for the 10.2mm tip is barely defined with a broad region of high standard deviation obscuring the average location of the separation shock.

The standard deviation function in ImageJ uses a variable range which is based on the magnitude of the highest calculated standard deviation in the image. The background of the standard deviation images darkens as flare angle is increased despite the level of noise in the flow remaining consistent. This change indicates an increasing maximum standard deviation as the range between light and dark values grows, thereby decreasing resolution. Overall standard deviation of the 40° and 43° flare runs is also exacerbated by the short run times caused by unstart issues.

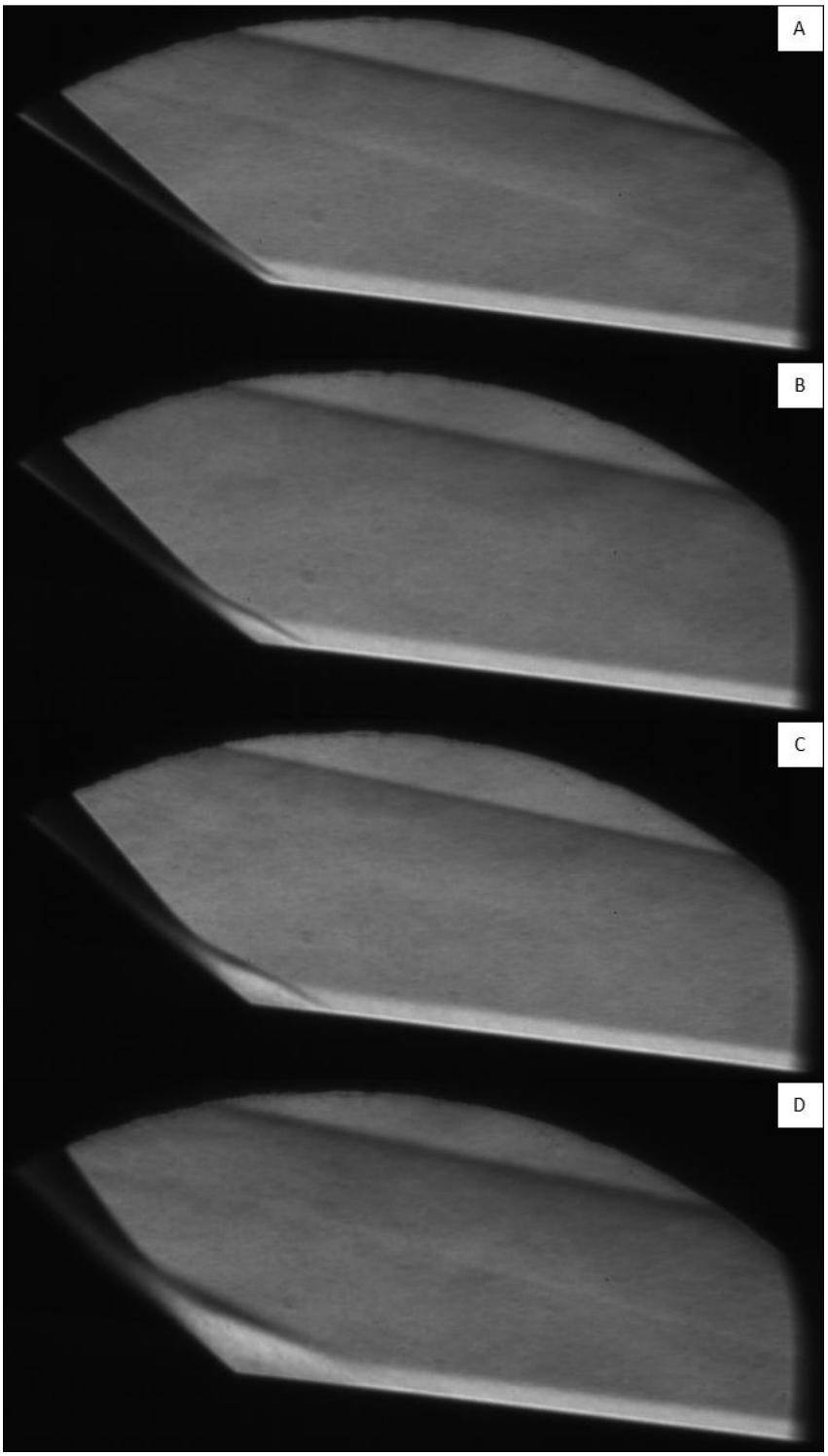

Figure 33. Flare Angle Comparison (Averaged 0.0mm tip at 400psi)

(A): 34° flare (B): 37° flare (C): 40° flare (D): 43° flare

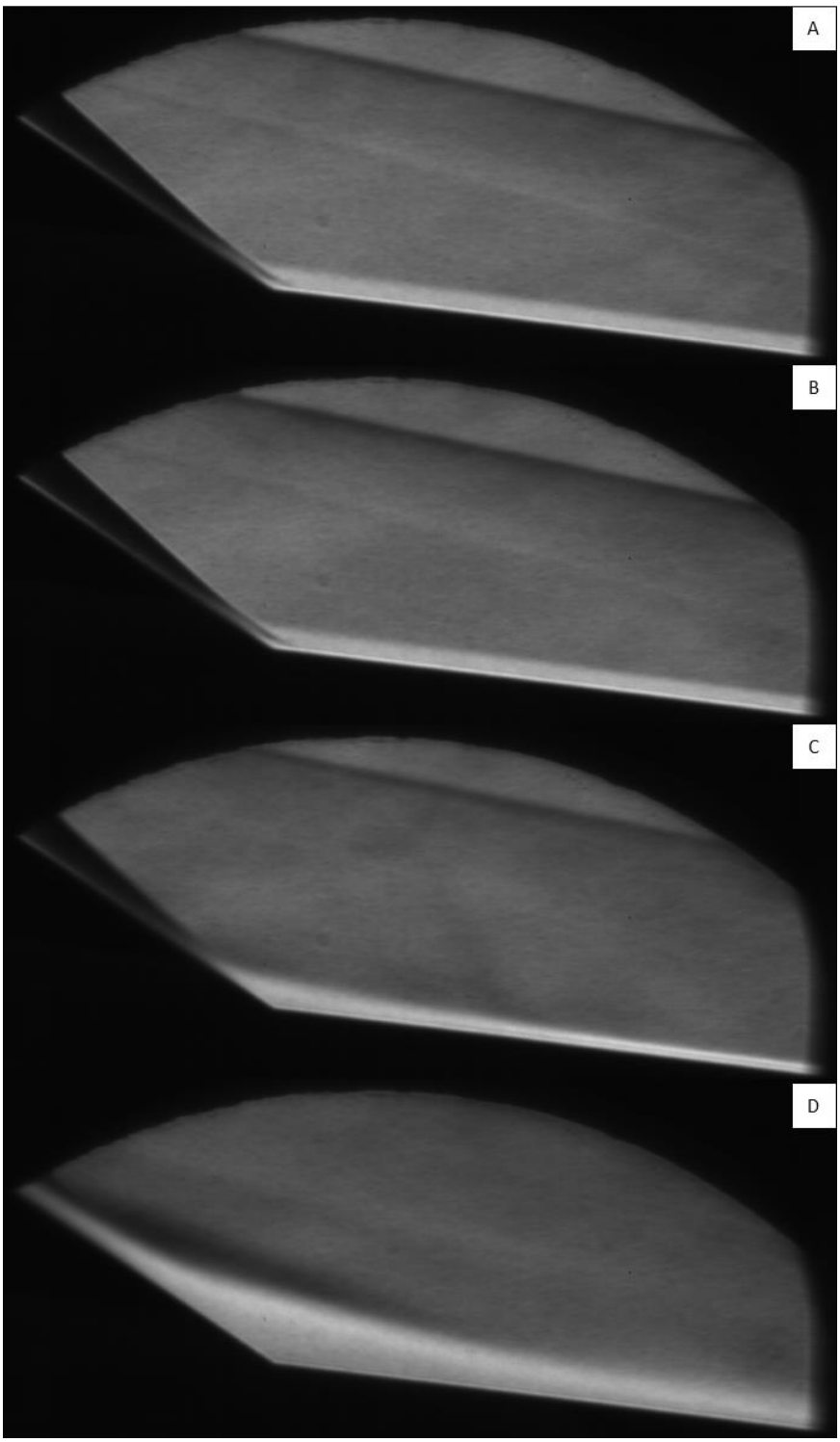

Figure 34. 34° base, 400psi (averaged)

(A): sharp tip (B): 0.5mm tip (C): 5.1mm tip (D): 10.2mm tip

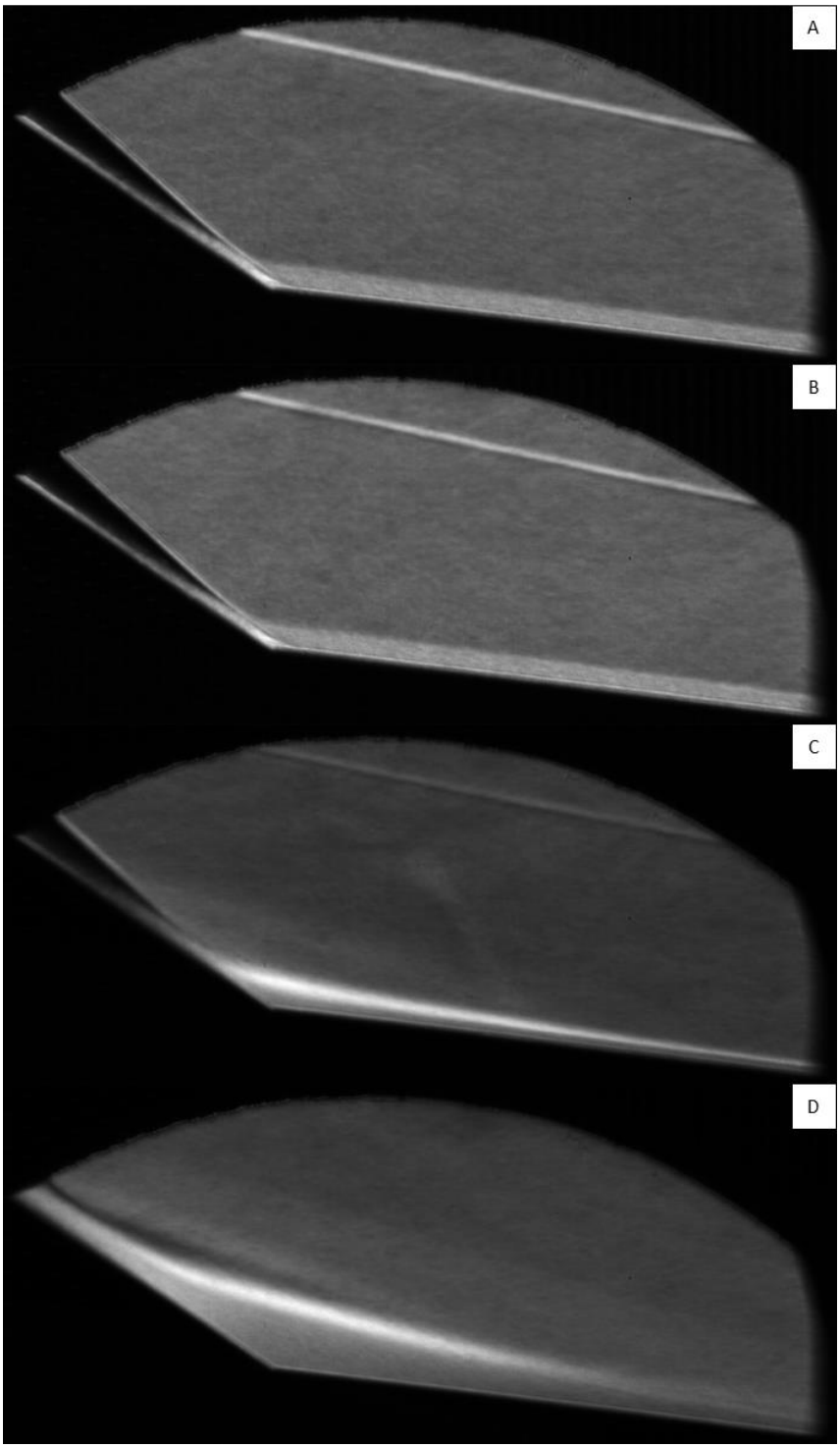

Figure 35. 34° base, 400psi (standard deviation)

(A): sharp tip (B): 0.5mm tip (C): 5.1mm tip (D): 10.2mm tip

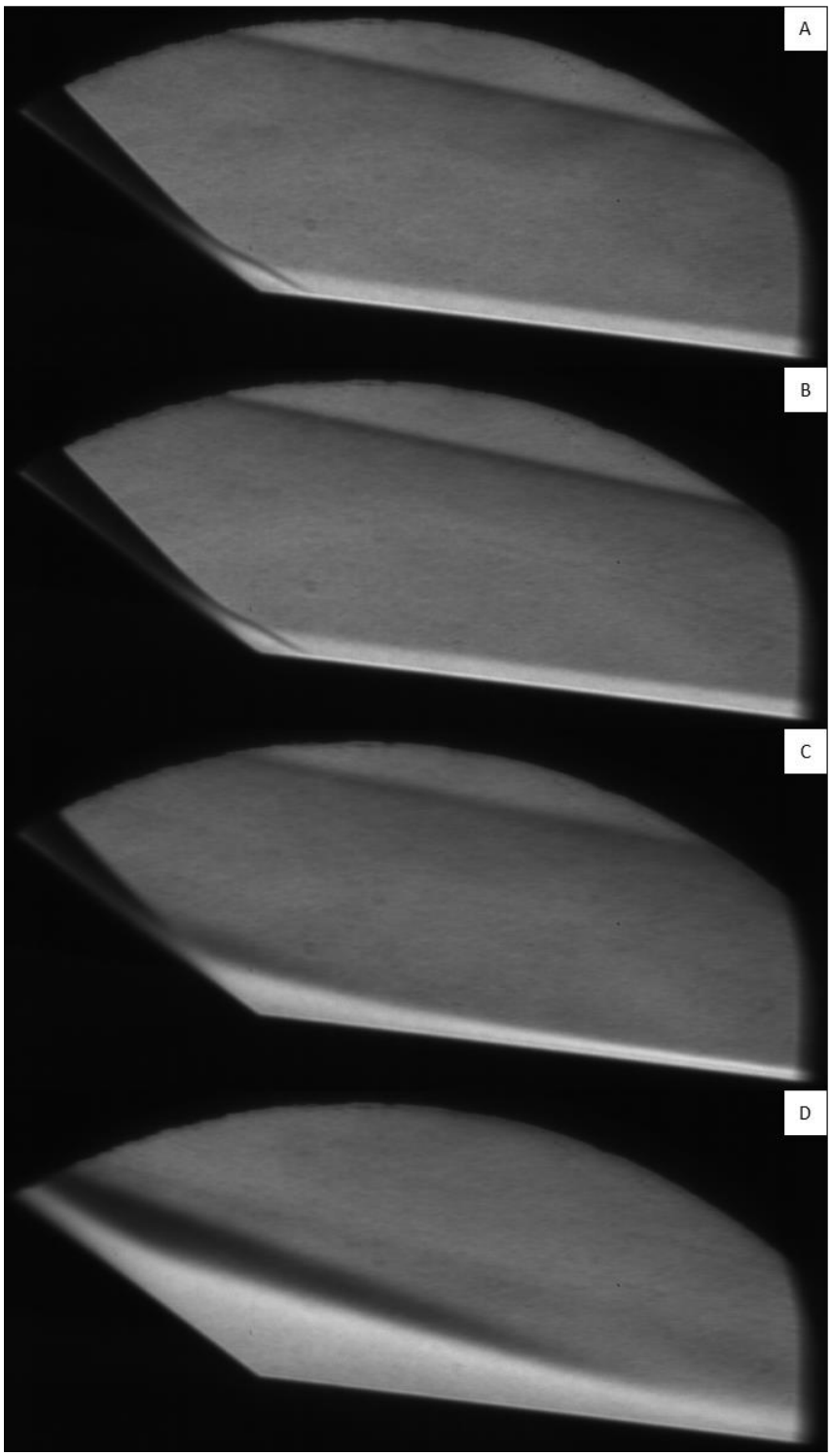

Figure 36. 37° base, 400psi (averaged)

(A): sharp tip (B): 0.5mm tip (C): 5.1mm tip (D): 10.2mm tip

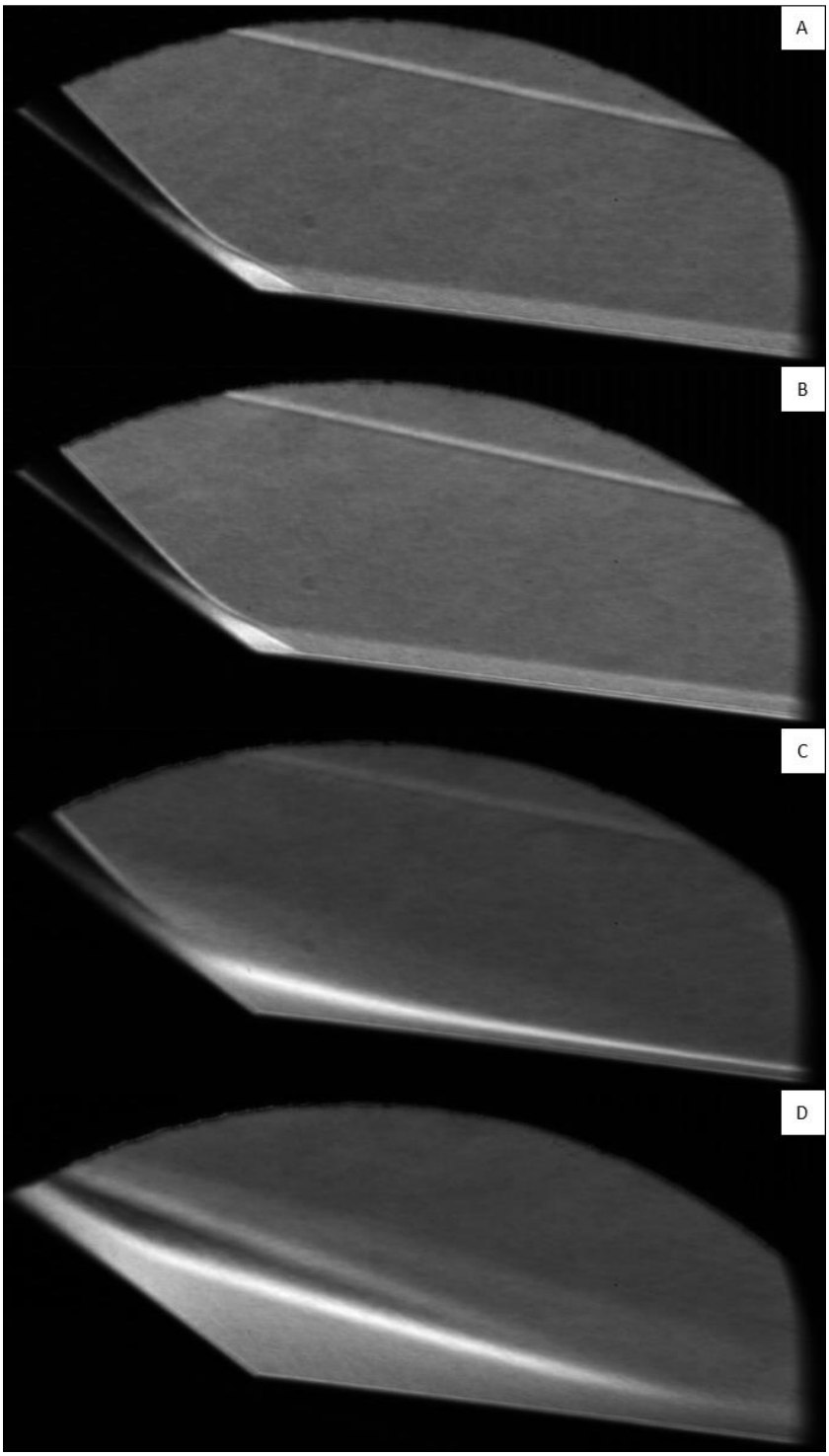

Figure 37. 37° base, 400psi (standard deviation)

(A): sharp tip (B): 0.5mm tip (C): 5.1mm tip (D): 10.2mm tip

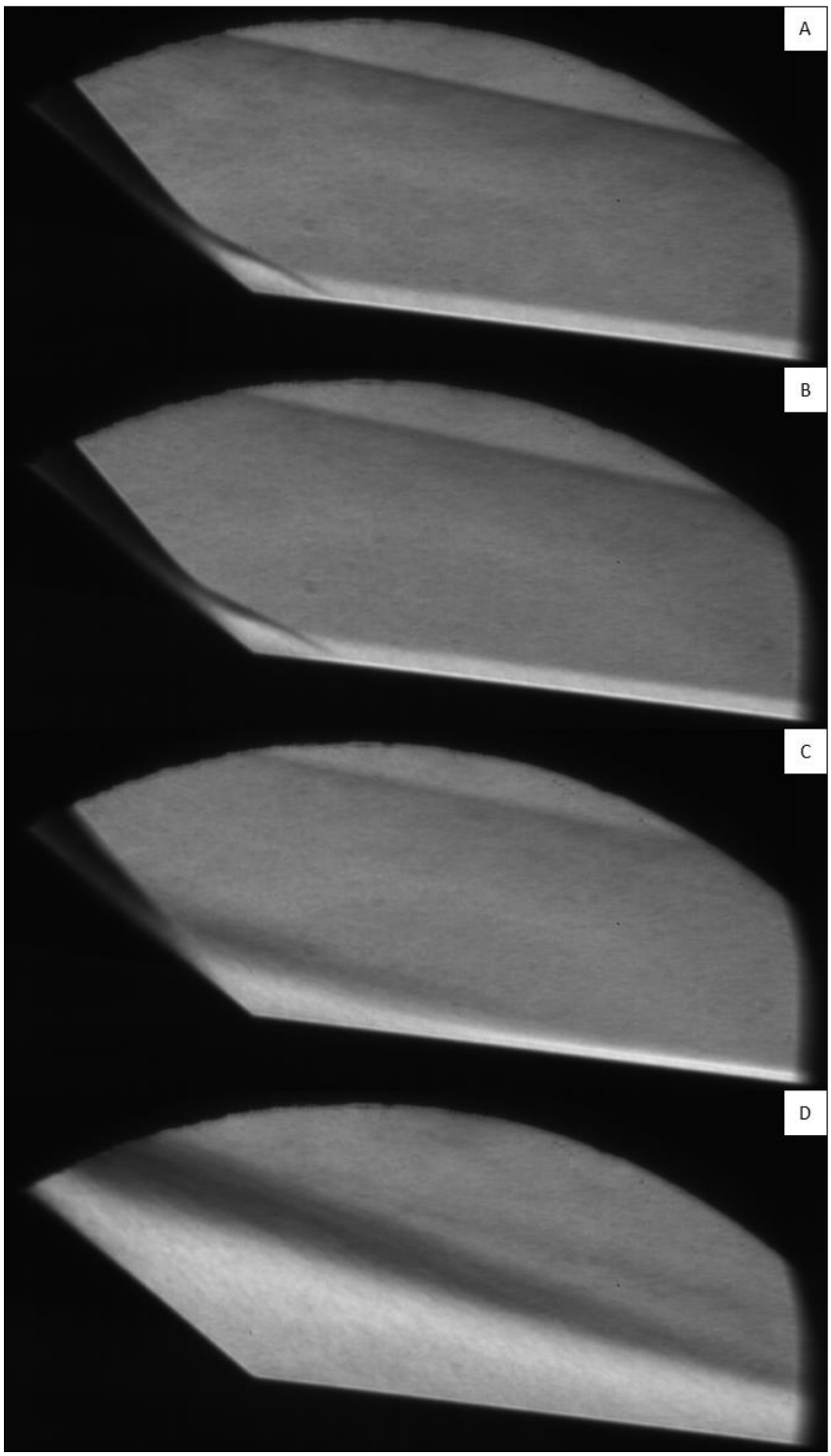

Figure 38. 40° base, 400psi (averaged)

(A): sharp tip (B): 0.5mm tip (C): 5.1mm tip (D): 10.2mm tip

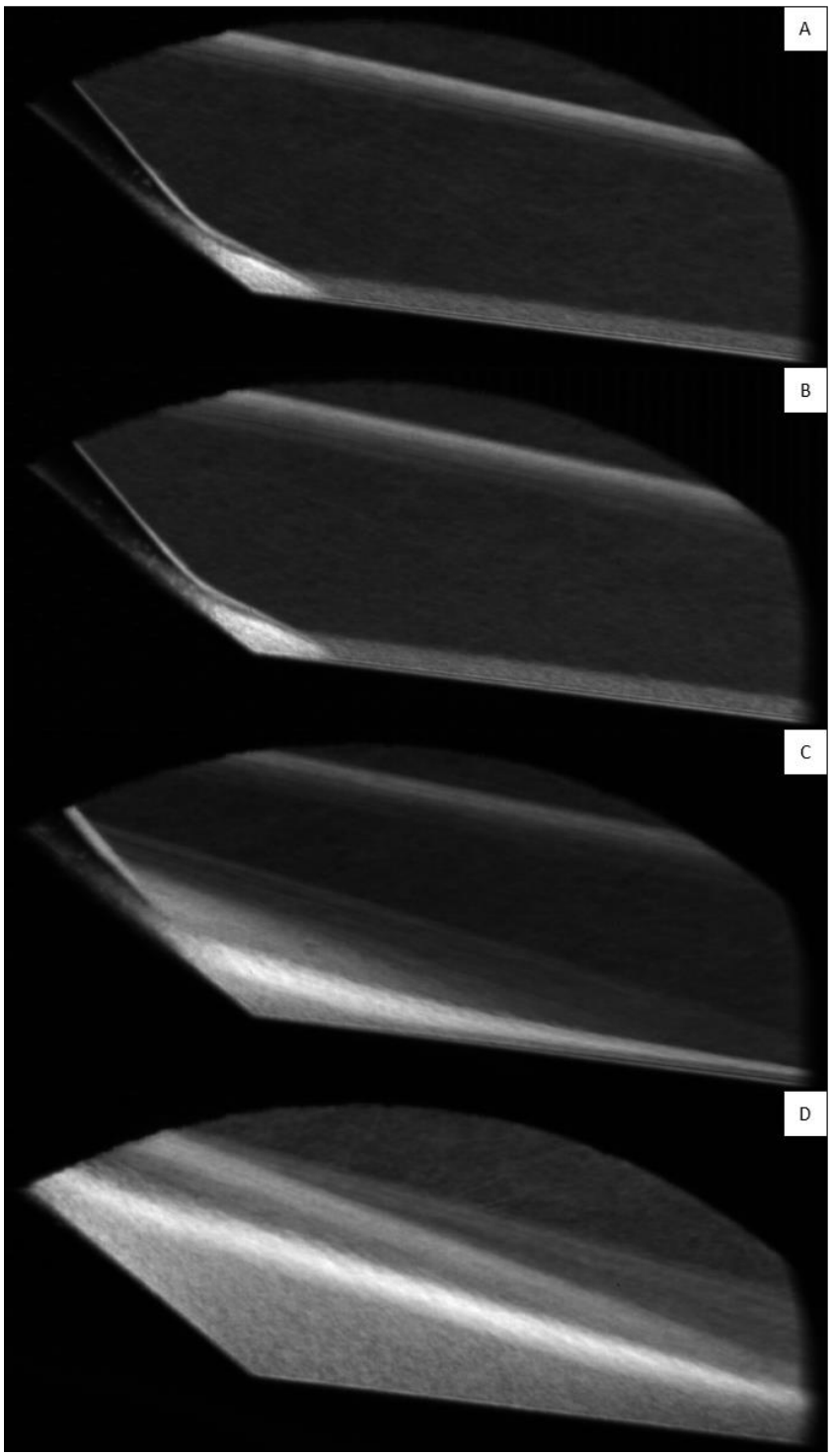

Figure 39. 40° base, 400psi (standard deviation)

(A): sharp tip (B): 0.5mm tip (C): 5.1mm tip (D): 10.2mm tip

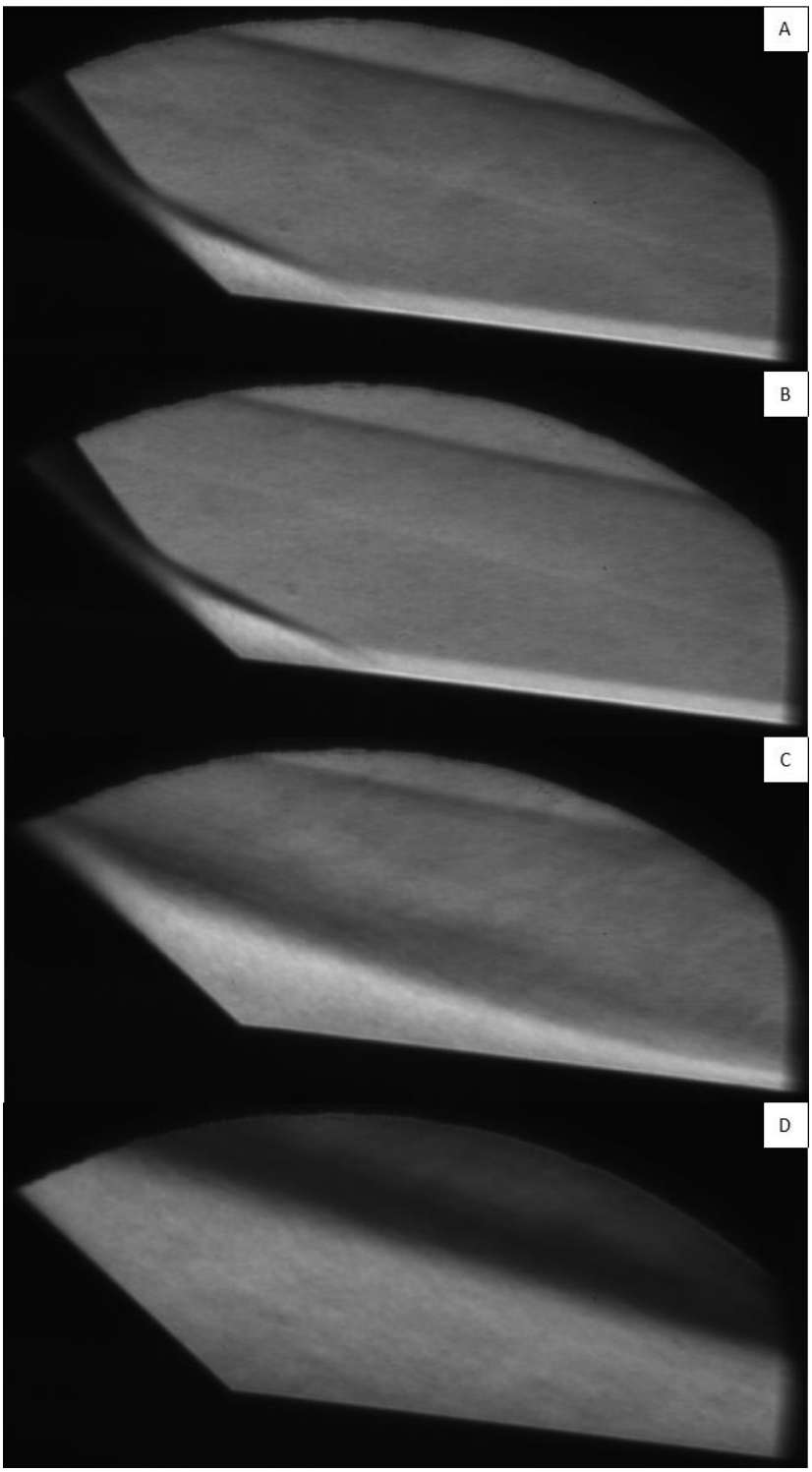

Figure 40. 43° base, 400psi (averaged)

(A): sharp tip (B): 0.5mm tip (C): 5.1mm tip (D): 10.2mm tip

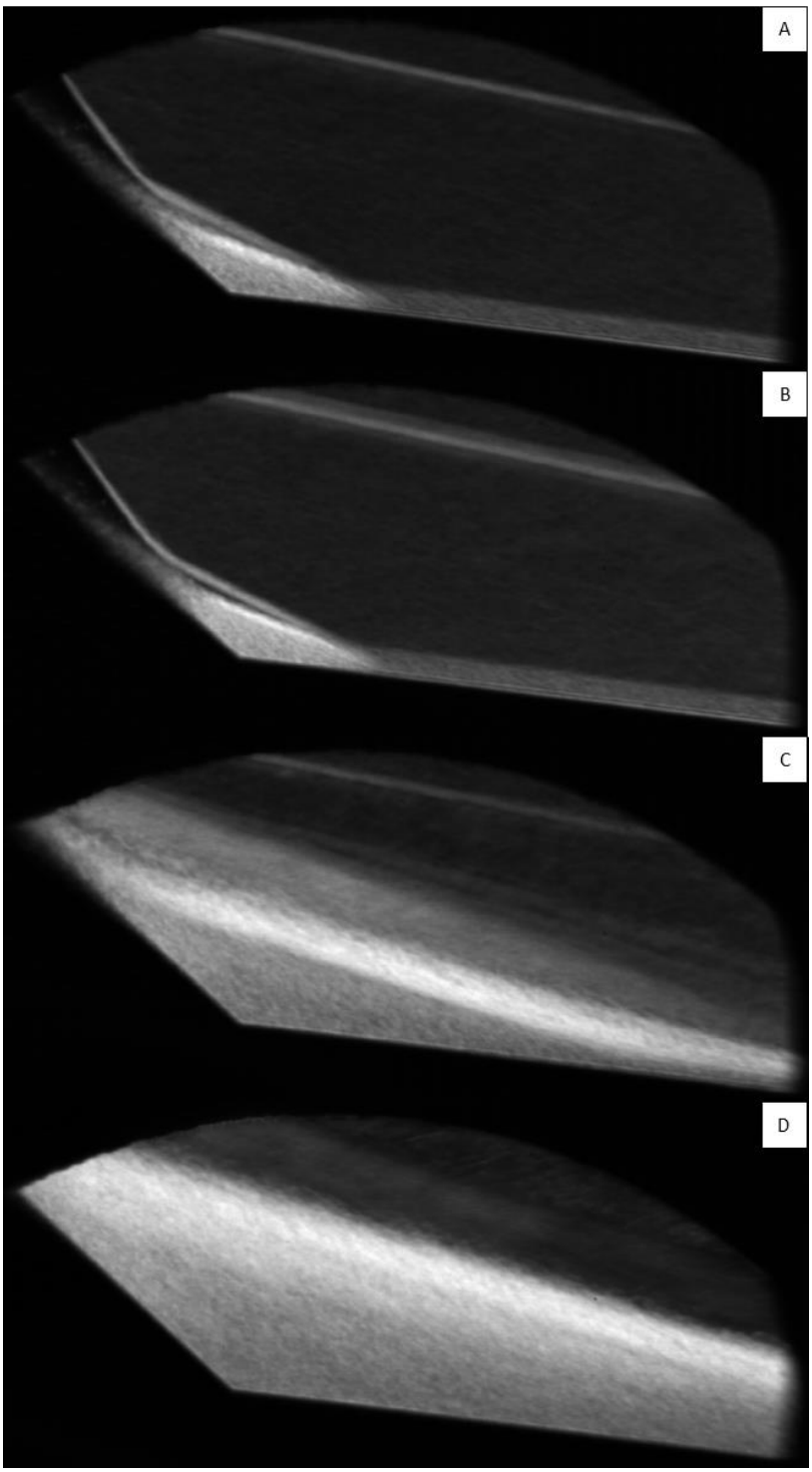

Figure 41. 43° base, 400psi (standard deviation)

(A): sharp tip (B): 0.5mm tip (C): 5.1mm tip (D): 10.2mm tip

Recirculation Region Measurements

ImageJ post-processing software was used to measure separation and reattachment points. Standard deviation images from each run were used because bright pixel regions corresponded to shock wave and boundary layer locations. An edge finder operation was performed in ImageJ to analytically determine borders of shock and boundary layer regions. After finding the edges, lines were projected along the recirculation region boundary and the cone/flare surfaces. The edge finding tool did not highlight a clear separation shock location for the blunt tip runs because of the large region of high standard deviation. For cases without a distinct separation shock edge, the separation line was projected between the upper and lower extents of the high standard deviation region. The built-in measurement function was used to find the distance between the cone/flare junction and the points where the projected recirculation boundary intersected the model surface. While the output provided a pixel count, the pixel-to-distance calibration from PFV was utilized to convert the results to real-world dimensions. Figure 42 shows an example of the process, from the base standard deviation image, to finding edges, to projecting lines for regions of interest.

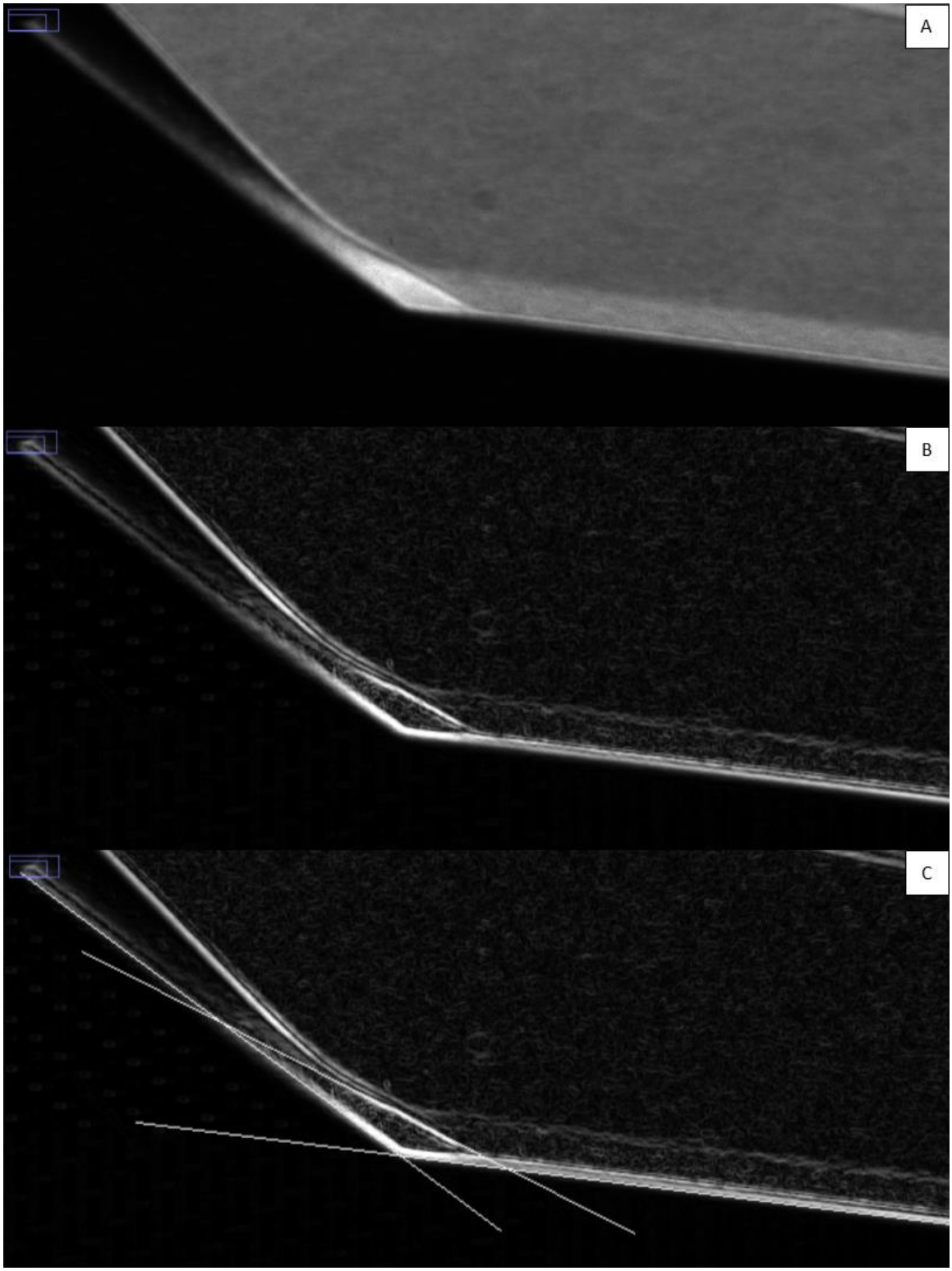

Figure 42. Recirculation Region Measurement Process

(A): Standard Deviation Image (B): Post 'Find Edges' (C): Projecting Regions of interest

Error was quantified by first projecting lines along the upper and lower bounds of the high standard deviation region, which indicated the presence of the separation shock. The distance between the two projected lines' intersection points with the cone and flare surfaces was measured parallel to the respective surface. This measured distance is quantified as the measurement error for each separation and reattachment point.

The horizontal knife edge, 400psi runs were used for analysis because they resulted in the sharpest contrast between regions of interest. Reattachment points were visible in the captured frame for every flare/tip combination. Due to the size of the recirculation region, separation locations for blunt tip cases were not clearly defined and many occurred upstream, out of the available frame. As previously mentioned, the blunt tips generated a large entropy layer that, in turn, produced a relatively large density gradient which obscured the laminar boundary layer. The combination of the changing state of the boundary layer and the unstable recirculation region size resulted in a large standard deviation for the images from blunt tip runs. This large standard deviation is particularly evident in Figure 39 and Figure 41. Therefore, the obtained separation locations for the 5.1mm and 10.2mm tips are not as precise as the values for the sharper tips. This issue is quantified by the larger error values for the blunt tip data. Despite the lower precision, the data points are still plotted on Figure 43 to show general trends as the geometry of the model is changed. Negative values on the charts and table represent separation points (upstream of the cone/flare junction) and positive values represent reattachment points (downstream of the cone/flare junction.) The horizontal bars on the chart represent the measurement error for each point. Table 5 shows all measured separation and reattachment points. Cells with asterisks indicate the point of interest

occurred out of the frame. These measurements were extrapolated by projecting lines for the separation region and model edge. Extrapolation means the values are not as precise, but they are included to show trends in recirculation region behavior. Error calculations were not performed for the extrapolated points.

As expected from prior research, separation generally occurs further upstream of the cone/flare junction for blunt tips compared to sharp tips with the same flare angle. The delayed separation associated with the sharp tips is primarily due to the extra momentum of the turbulent boundary layer, which helps keep the boundary layer flow attached to the cone surface. Also, as expected based on prior research and observations, separation occurs farther upstream from the cone/flare junction as flare angle is increased. [23] This earlier separation is due to the strengthened adverse pressure gradient. Reattachment points follow the same trends as the separation points. For conditions where separation occurs further upstream of the cone/flare junction, reattachment occurs further downstream. Figure 44 shows recirculation region length following the cone/flare surface. Some data points for the blunt tips are missing, as extrapolated measurements were not included on either plot. As expected, increasing adverse pressure gradient and increasing cone tip radius both increase the length of the recirculation region.

Table 5. Separation and Reattachment Points

Flare Angle (°)	Tip Radius (mm)	Stagnation Pressure (psi)	Separation ± error (mm)	Reattachment ± error (mm)	Separation Length (mm)
34	0	200	-8.9±1.2	16.7±1.7	25.6
		400	-5.8±0.6	13.6±1.0	19.3
	0.5	200	-8.2±0.7	16.7±1.3	24.9
		400	-7.6±0.7	11.8±1.6	19.3
	5.1	200	-161.9*	23.6±3.7	185.5*
		400	-128.3±25.6	12.5±3.8	140.9
	10.2	200	-151.0*	41.6±10.2	192.6*
		400	-120.1±12.2	45.8±3.8	165.9
37	0	200	-13.3±0.7	31.1±4.0	44.5
		400	-12.2±0.7	35.1±2.1	47.4
	0.5	200	-12.5±0.9	34.5±4.8	46.9
		400	-13.3±0.8	33.8±2.3	47.1
	5.1	200	-173.9*	27.6±5.2	201.5*
		400	-86.7±13.3	23.4±4.7	110.1
	10.2	200	-165.2*	53.8±5.6	219.1*
		400	-129.0±9.6	56.3±6.7	185.3
40	0	200	-20.0±1.7	31.4±2.0	51.4
		400	-22.5±1.1	32.5±3.4	54.9
	0.5	200	-19.8±1.2	36.3±4.7	56.0
		400	-21.6±1.0	37.1±3.7	58.7
	5.1	200	-132.6*	29.6±6.8	162.1*
		400	-87.0±15.7	30.0±7.0	117.0
	10.2	200	-188.6*	72.7±7.6	261.3*
		400	-174.8*	74.1±7.5	248.9*
43	0	200	-35.4±1.1	42.0±5.2	77.4
		400	-40.0±3.3	43.8±9.2	83.8
	0.5	200	-31.8±1.9	41.6±6.7	73.4
		400	-36.5±1.6	42.6±7.3	79.1
	5.1	200	-185.1*	63.2±11.0	248.3*
		400	-139.9*	58.7±8.7	198.6*
	10.2	200	-275.8*	93.2±10.5	369.0*
		400	-224.0*	87.2±8.9	311.1*

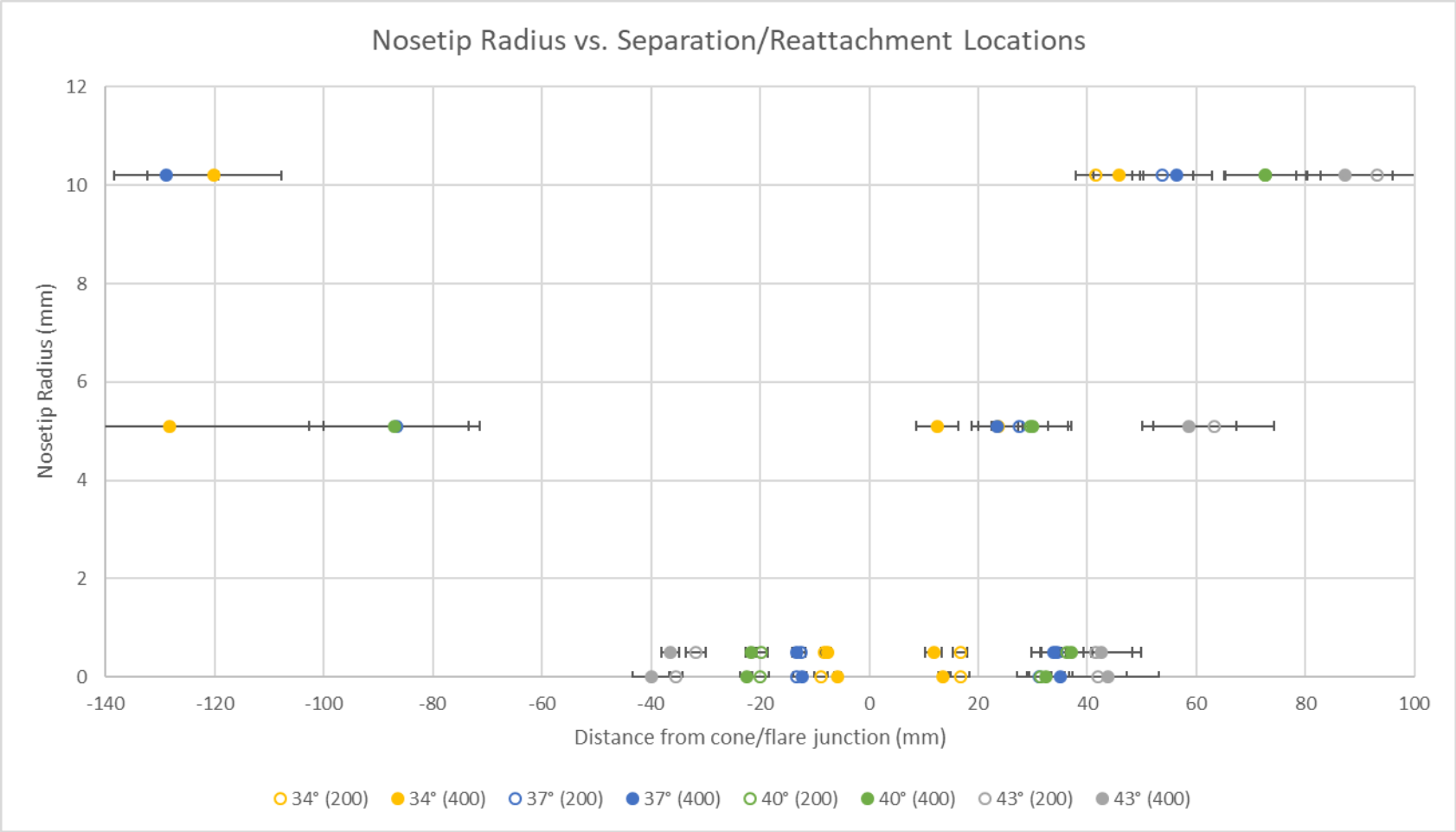

Figure 43. Nosetip Radius vs. Separation/Reattachment Locations

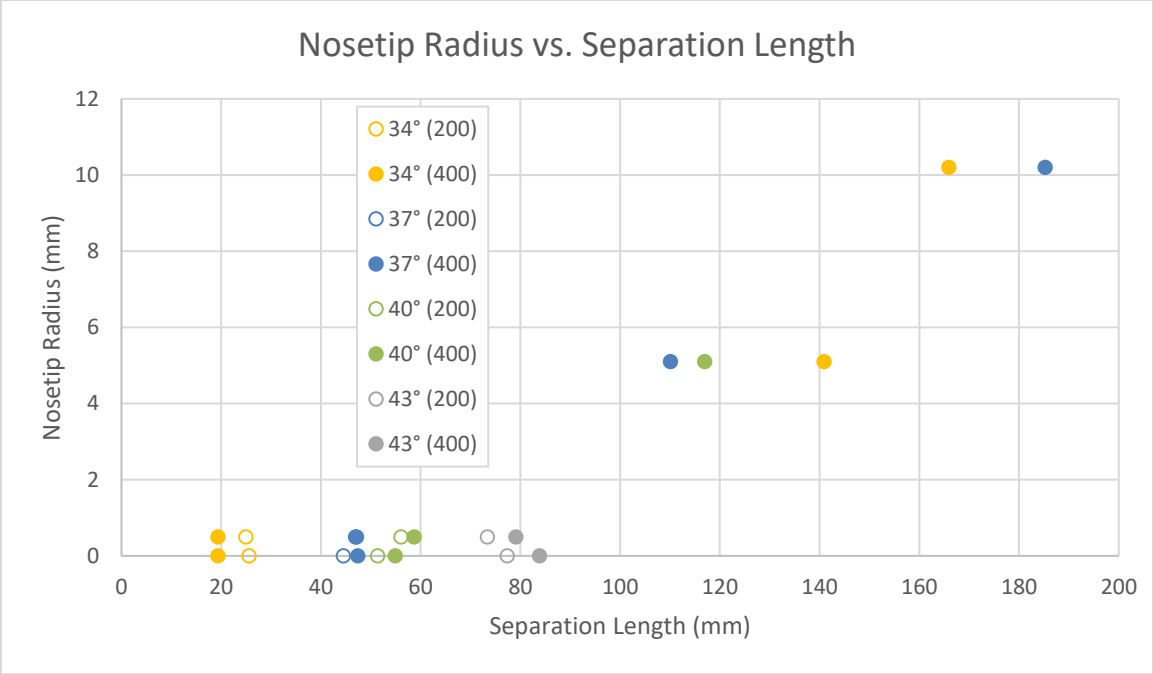

Figure 44. Nosetip Radius vs. Separation Length

Figure 45 compares separation and reattachment points measured during the Schlieren testing and from the prior test on the same cone/flare model in the AFRL Ludwieg tube. Running et al. used infrared thermography to measure surface temperatures of the model during runs with the same 200psi and 400psi stagnation pressures. [23] To reduce clutter on the figure, only the 400psi (Re=20.6x10^6 /m) data from each test is plotted. Different boundary layer behavior (laminar, transitional, or turbulent) corresponds to different rates of surface heating, creating contrast between flow regions. By nature, cumulative heating effects measured via infrared thermography are averaged during the run. In contrast, the Schlieren images show transient behavior for the length of each frame (1/20,000 second, in the case of these tests). Averaging

techniques were applied to the high-speed Schlieren images during post-processing to offer a more direct comparison.

Both forms of testing display similar trends. As adverse pressure gradient increases, the overall separation length increases as well. Differences between the 0.0mm and 0.5mm radius sharp tips were virtually negligible, with both tips generating turbulent boundary layers. For both tests, the 10.2mm tip led to larger recirculation regions than the 5.1mm radius tip. The Schlieren testing results showed greater changes in reattachment points when varying flare angle compared to the infrared thermography tests. The infrared thermography did not return enough separation points to make a similar comparison to Schlieren separation points. In general, the Schlieren testing showed reattachment occurring further downstream of the cone/flare junction compared to the infrared thermography tests with the same cone/flare geometry. In contrast, the limited data points available from the infrared thermography tests showed separation occurring further upstream of the cone/flare junction compared to the available points from Schlieren testing. Neither form of testing led to precise measurement of separation points from the blunt tip tests. The high level of shock motion, as discussed in the next section, is most likely to blame for lack of fidelity in separation points.

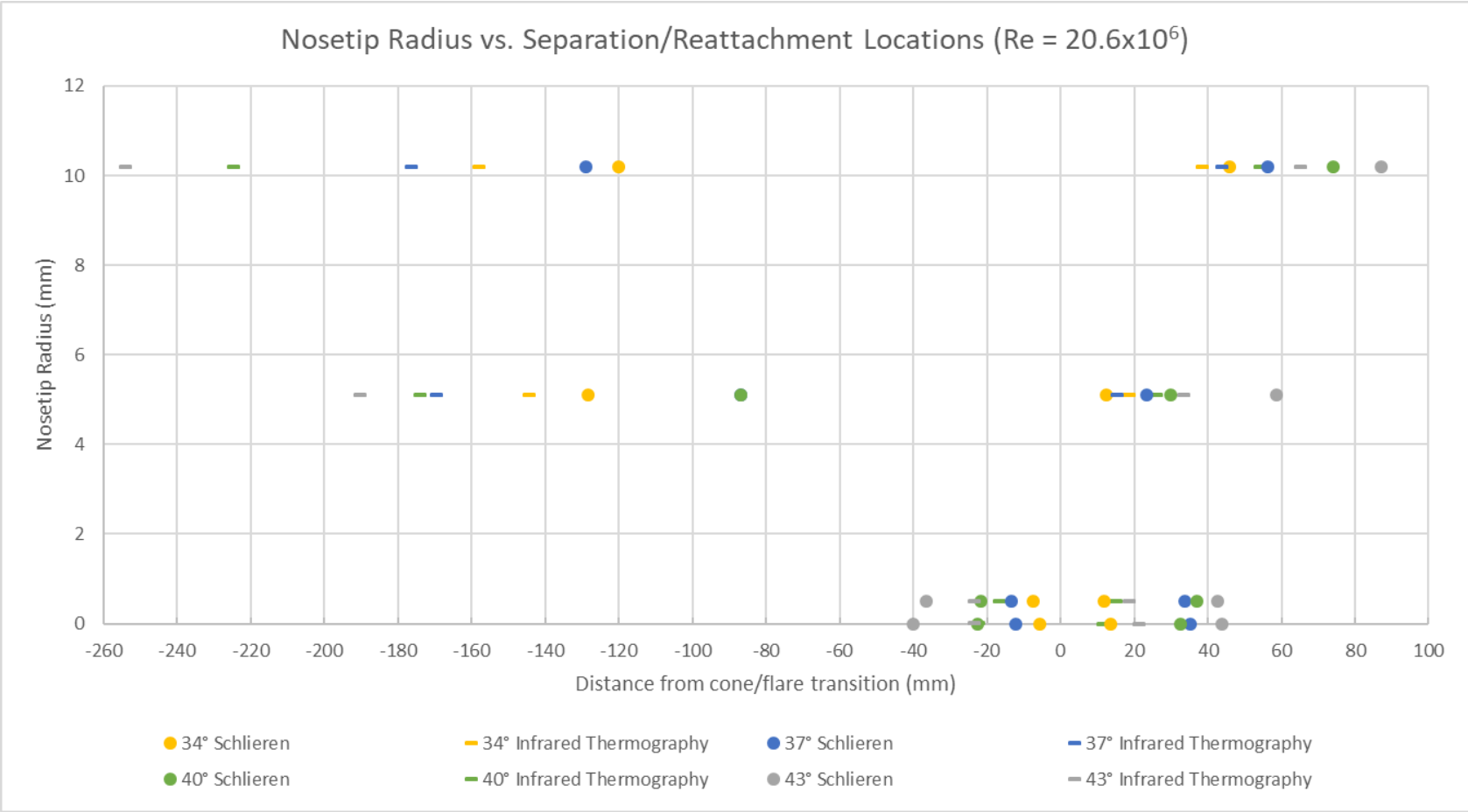

Figure 45. Comparison of Nosetip Radius vs. Separation/Reattachment Locations: Schlieren versus Infrared Thermography [23]

Unsteady Shock Motion Measurements

Unsteady boundary layer behavior was observed when the cone/flare model was fitted with the blunt 5.1mm and 10.2mm radius tips at all flare angles. The high level of motion was unexpected based on the infrared thermography tests performed by Running et al. [23] The 355Hz frame rate of the infrared camera used in testing was likely too slow to capture the unsteady motion. At the 20,000Hz setting, the frame rate of the high-speed camera used for Schlieren imaging was optimal for tracking the unsteady shock motion. This unsteady SBLI behavior has been observed in prior research. Dolling and Murphy measured wall pressure fluctuations in a compression ramp in a Mach 3 flow. [27] The study revealed large pressure fluctuations in the interaction region, particularly near the separation and reattachment points. Pressure fluctuations are likely responsible for the unsteady shock motion captured in the Schlieren images.

As shown in Figure 46, the separation shock tends to be transient and moves upstream and downstream along the cone frustum. This movement is possibly due to the turbulence intensity variations in the boundary layer. Over the course of the run, the boundary layer appears to be tripping between laminar and turbulent upstream, mostly out of the frame. The changes of the boundary layer thickness at the right edge of each frame likely indicates changes in the boundary layer state. This variation in the boundary layer effects the separation location and the overall size of the recirculation region. A large recirculation region generally coincided with a thick boundary layer just upstream of the separation location. The boundary layer would become thin as the recirculation region collapsed. Over the course of the videos, there appear to be periods where the growth and collapse of the recirculation region are cyclical, possibly following an

oscillation frequency. Two methods of obtaining the oscillation frequency of the recirculation region were performed.

First, a qualitative approach of counting frames was performed. Each video was progressed frame-by-frame until a separation shock appeared and reached a maximum radial distance from the cone/flare junction. The timestamp was recorded, and the video was progressed until the previous separation region collapsed and a new separation shock formed. For example, in Figure 46, the separation shock reaches its maximum distance around frame C and has collapsed by frame F. A new separation shock then appears and reaches a maximum distance around frame H. Measuring time intervals was only possible with the 34° and 37° flares due to unstart preventing adequate runtimes with the 40° and 43° flares. Measured time intervals were averaged, and a standard deviation was calculated. The intervals were also converted to frequencies to offer a direct comparison to results calculated by using a second approach.

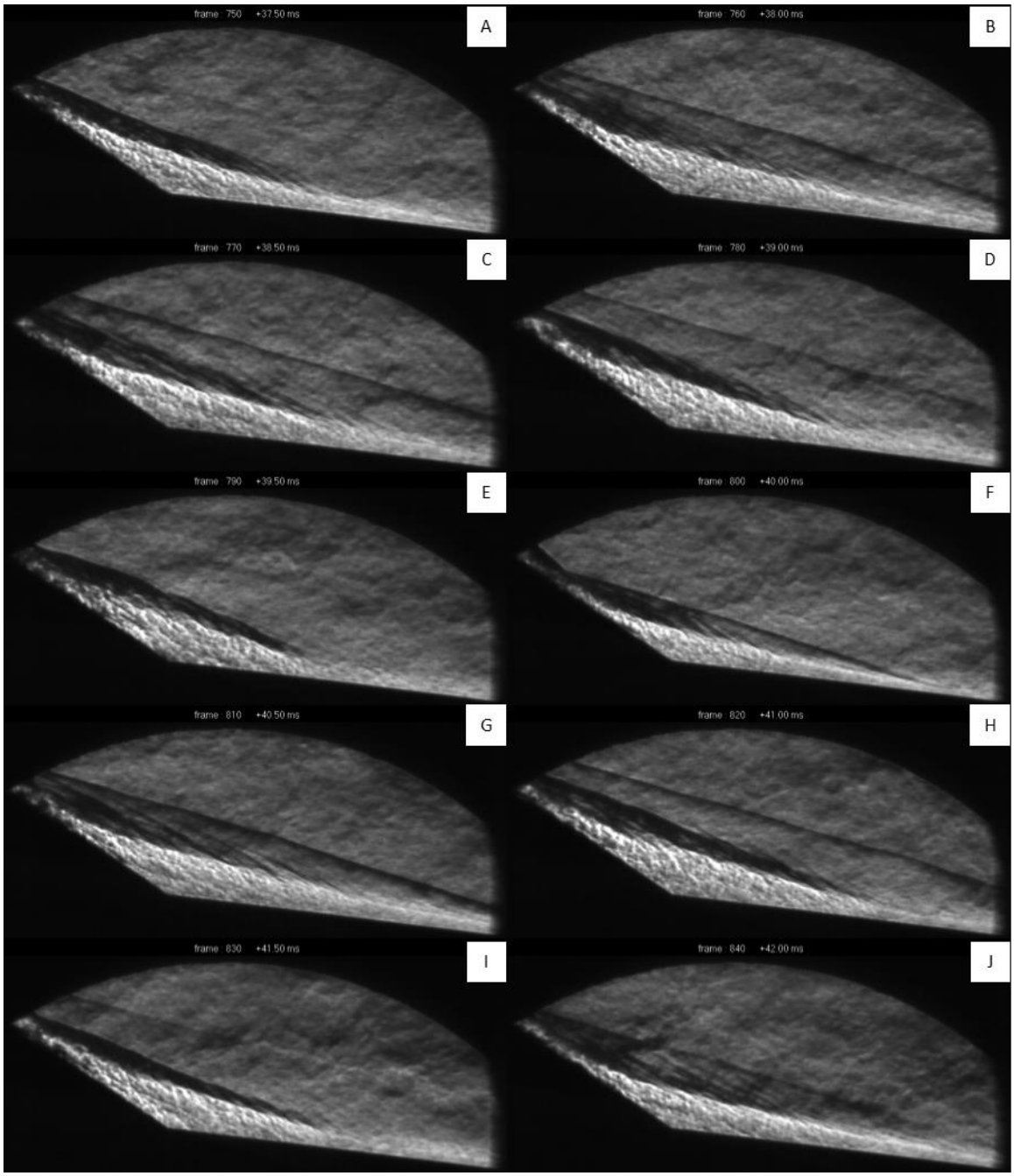

Figure 46. Boundary Layer Motion (10 Frame, 0.5ms Time Steps)

The second method took a quantitative approach by collecting data in ImageJ and processing it in MATLAB. Using ImageJ, a four-pixel by four-pixel area was selected in a region where the separation shocks would reach their maximum radial distance. An example is provided in Figure 47. The ImageJ command 'Plot Z-Axis Profile' was then used to capture frequency data. The command takes the average intensity of the pixels in the selected region and plots the value for each frame in the video. The data was then imported into a MATLAB script and a Fast Fourier Transformation (FFT) was performed. The FFT was intended to highlight dominant frequencies in the intensity plot corresponding to periodic growth and collapse of recirculation regions for blunt-tip runs. Figure 48 shows an example plot of the 'Plot Z-Axis Profile' data output from ImageJ. High and low-intensity spikes should indicate the shock crossing the selected region. However, density variations which take the form of light and dark splotches in the flow add substantial noise to the plot. Figure 49 shows an FFT plot of the data from Figure 48. The data point selected on the figure is the highest peak above 100Hz, indicating it is the dominant frequency in the processed data.

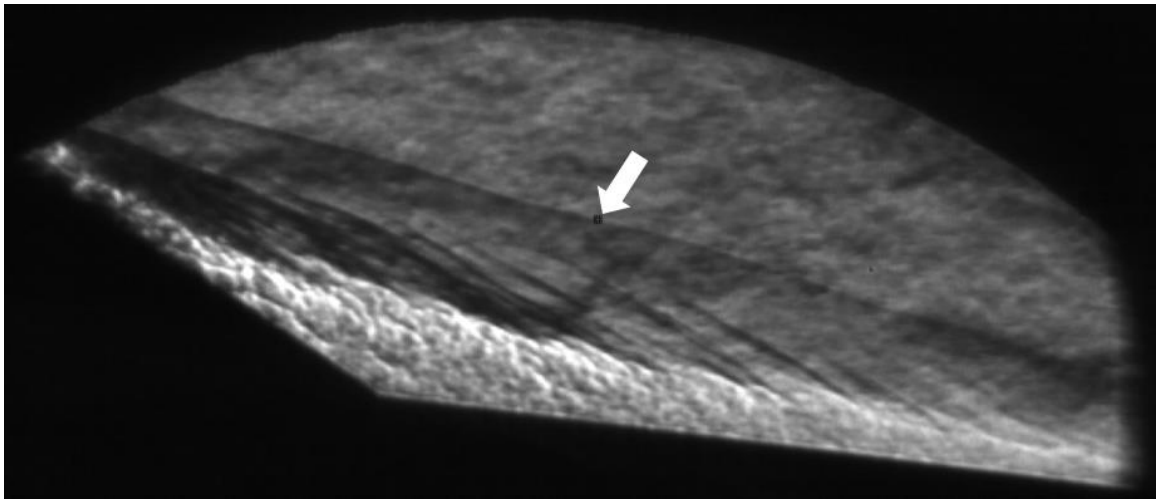

Figure 47. Pixel Area Example

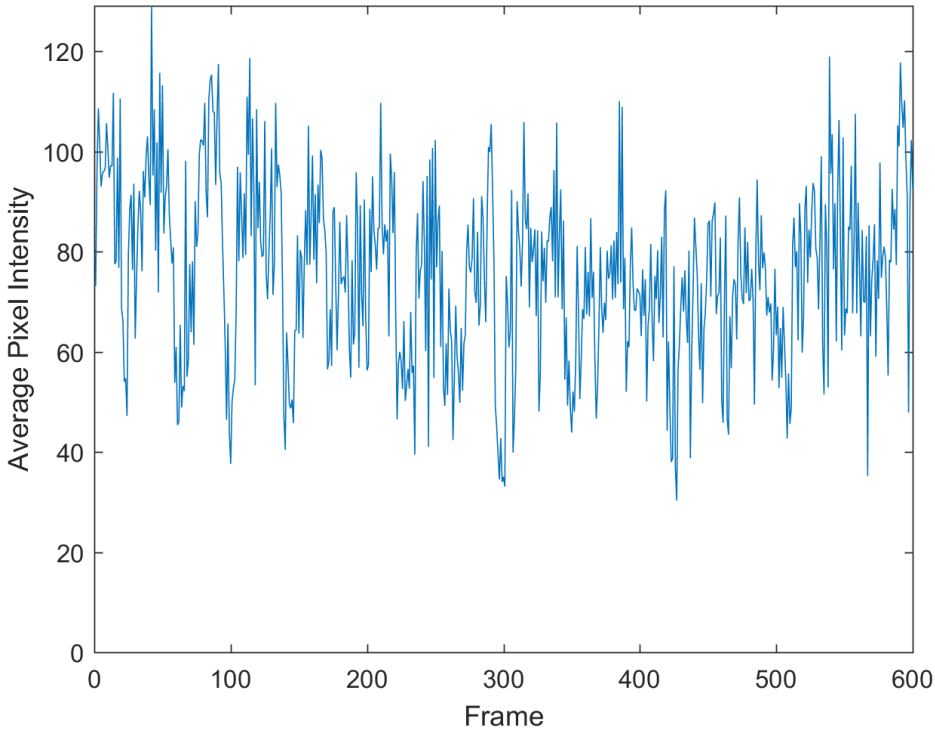

Figure 48. Pixel Intensity Versus Frame Example (34° flare, 10.2mm radius tip)

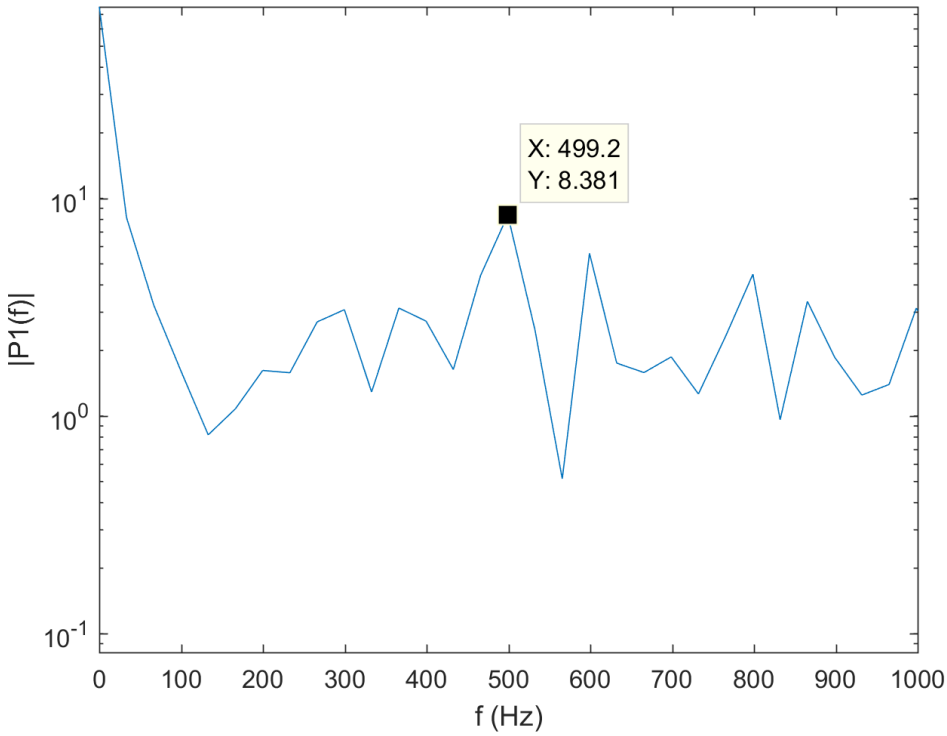

Figure 49. FFT Example (34° flare, 10.2mm radius tip)

Results are presented in Table 6. For both methods and both flare angles, the measured oscillation frequency was higher with the 5.1mm tip than the 10.2mm tip under identical conditions. The intervals from the frame counting method had high standard deviation levels due to a limited number of cycles being visible during the steady portion of each run. Despite the Ludwieg tube supplying 100ms of quasi-steady flow in the first expansion period, the oscillating recirculation region takes some time to develop. This problem of limited runtime also effected the FFT method. As seen in Figure 49, the peak at 499Hz is far from dominant, with multiple other frequencies having similar intensity levels. This problem was present in all four FFTs performed. Despite these shortcomings, there is some agreement in the measured frequencies for both methods, generally ranging between 400Hz and 600Hz. The FFT plots support this trend, as most secondary peaks fall into the 400-600Hz range as well. Agreement between the results helps verify the reliability of each method.

Measurements based solely on high-speed Schlieren imagery have inherent limits. Outfitting the cone/flare model with pressure transducers would provide more fidelity, as pressure data can be used to determine if the local state of the boundary layer is laminar or turbulent. Based on observations of the Schlieren images recorded, the boundary layer transition frequency would likely coincide with the oscillations in the size of the recirculation region. Syncing Schlieren images with surface pressure data would provide a more complete picture of shock and boundary layer behavior on the cone/flare model. With the data gained from this study, it is difficult to determine whether the unstable behavior was a result of laminar boundary layer physics or some instability in the flow from the Ludwieg tube nozzle. Very small vertical movement of the cone tips, though not

detected in the video, as discussed in an earlier section, could have also contributed to the unsteady shock motion. Minor changes in angle of attack would certainly induce minor variations in boundary layer behavior which would be amplified downstream, near the cone/flare junction.

Table 6. Blunt Tip Shock Motion

Flare Angle	Tip Radius (mm)	Average Interval (ms)	Standard Deviation (ms)	Average Frequency (Hz)	FFT Frequency (Hz)
		Via frame counting method			Via FFT method
34°	5.1	1.7	0.4	579	532
	10.2	1.9	0.5	532	499
37°	5.1	1.7	0.5	597	599
	10.2	2.6	1.2	392	465

Summary

This chapter presented results and analysis from the AFRL Ludwieg tube characterization study and Schlieren testing performed on a cone/flare model. Analysis from the Schlieren study included measurements of the bow-shocks from the cone tips and downstream near the cone/flare junction. Measurements of observed recirculation regions at the cone/flare junctions for each run were performed and compared to previous research. Finally, recirculation region instabilities due to laminar boundary layers were analyzed.

V. Conclusions and Recommendations

Chapter Overview

The discussed studies performed in the AFRL Ludwieg tube facility served two purposes. The Pitot survey was an important step in characterizing the test-section flow in the recently-completed facility. High-speed Schlieren imaging of the cone/flare model continued a focus on learning about the fundamental behavior of simple geometries in hypersonic flight conditions and demonstrated the usefulness of the system as a diagnostic tool. This chapter summarizes the results of both studies and the significance of the findings. Recommendations for future testing are discussed as well.

Summary of Results

The tunnel characterization survey was limited in useable data points due to sensor failure. Sufficient measurements were collected for the downstream sting position to generate a Mach number contour plot. Analysis revealed a quasi-steady core flow region of Mach 6.14 with a diameter of about 400mm. Outside of the core flow region, Mach number drastically increased as flow grew more turbulent. With the 43° flare installed, the model blocks roughly 49% of the core flow cross section. This blockage ratio was likely responsible for the unstart observed when testing with the 40° and 43° flares.

Shock and boundary layer behavior generally followed expected patterns based on past experimental and analytical research. Blunt cone tips generated laminar boundary layers which separated earlier (occurred further upstream of the cone/flare junction) than the turbulent boundary layers induced by sharp cone tips. Separation also occurred

further upstream as the intensity of the adverse pressure gradient was amplified by increasing the flare angle. Earlier separation points coincided with later reattachment points (occurring further downstream of the cone/flare junction), resulting in larger overall recirculation regions. These results agreed with findings by Running et al., which served as a direct comparison for this study. [23]

While results and trends related to recirculation location were anticipated, the time-dependent shock motion observed in recirculation region sizes during tests with blunt cone tips were unexpected based on results from the infrared thermography testing. The recirculation regions for the cases with laminar boundary layers and large entropy layers did not maintain consistent size and location over the course of the runs. This behavior has been observed in past research on adverse pressure gradient regions. Qualitative and quantitative methods were employed to determine whether the unsteady shock motion was periodic or random. Loose periodic trends were observed. However, the Schlieren images were not ideal for performing this analysis. It is unclear whether the phenomenon is due to aspects of the laminar boundary layer flow, unsteady flow from the Ludwieg tube, changes in the model's angle of attack, or a combination of factors.

Measurements of the bow-shocks directly behind the cone tips revealed asymmetry which may have been due to the cone/flare model being set at a slightly positive angle of attack. Vertical movement of the cone tip, indicating pitch fluctuation, was also observed. This movement would constitute minor changes in angle of attack of the model during runs. Downstream measurements of the bow shocks, when compared to Taylor-Maccoll predictions, verified Mach 6 to Mach 6.1 flow from the Ludwieg tube nozzle.

Significance of Research

Characterizing flow in the AFRL Ludwieg tube test section was crucial for validating past and future tests in the facility. The diameter of the quasi-steady core flow is a key parameter for setting the maximum size of models that can be reliably tested without suffering from unstart or a turbulent freestream. The survey results included a more accurate average Mach number for the core flow, thereby improving freestream Reynolds number calculations for future testing. Synchronizing Schlieren images with pressure data from the Pitot probes aided in characterization efforts by providing additional insight into transient startup behavior of the Ludwieg tube.

High-speed Schlieren imaging proved to be an effective method for visualizing and diagnosing flow inside the Ludwieg tube test section. The Schlieren system proved to be robust, with no failures experienced during testing. Setup was also straightforward and required no adjustment to the model or the Ludwieg tube test section. Results from the cone/flare testing generally agreed with past research. This agreement serves to validate the experiments described herein along with prior analytical and wind tunnel testing of similar geometry in hypersonic flows. Shock intersection and shock/boundary-layer interactions brought about by adverse pressure gradients are of great concern for research and development as hypersonic vehicle designs are inevitably riddled with adverse pressure regions. An understanding of the behavior will allow designers to lessen the severity and mitigate the thermal and pressure loads associated with these regions. For example, as demonstrated in testing, shallow turning angles resulted in smaller areas of recirculation. The unstable behavior observed with the blunt cone tips is also significant. With an oscillation rate ranging from hundreds to thousands of Hertz, the changing area

effected by a recirculation region would experience accelerated wear and fatigue. Further research into the root causes of this oscillatory feature is therefore warranted.

Recommendations for Future Testing

Further refinement of data collection in the AFRL Ludwieg tube, and additional measurement techniques would improve understanding of the physics involved in the cone/flare model. Incorporating a larger flat mirror on the light source side of the Schlieren system would prevent the outer portion of the beam from being wasted. Utilizing the entire beam would allow for a larger diameter of collimated light, increasing the captured area in the Schlieren frame. The bases of the cone/flare model include set screws for locking the model to the sting arm, preventing rotation if the model must be clocked at a specific position. While the screws were not tightened, as model clocking was irrelevant for Schlieren testing, tightening the set screws may reduce pitch and yaw fluctuations during runs. Incorporating accelerometers and pressure sensors would provide much more insight into the physics of the cone/flare model. Accelerometer data would provide detailed information regarding model vibrations to include pitch and yaw fluctuations. The cone/flare model is predrilled for adding pressure sensors. As discussed in Chapter IV, surface pressure data would provide much greater insight into the local state of the boundary layer at strategic locations on the model. Pressure data would build upon and complete the story started by infrared thermography and high speed Schlieren studies of the cone/flare model.

Appendix

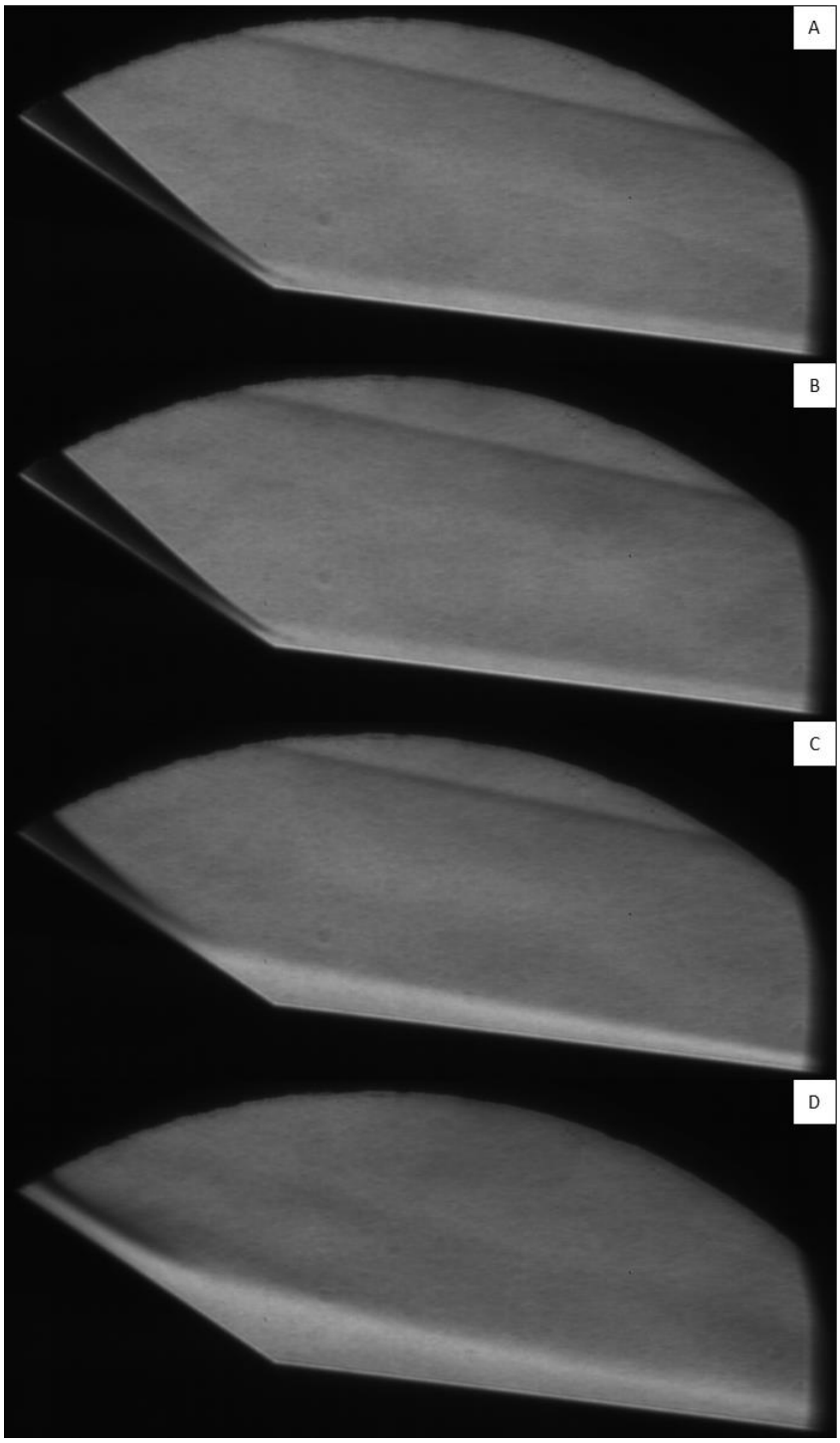

Figure 50. 34° base, 200psi (averaged)

(A): sharp tip (B): 0.5mm tip (C): 5.1mm tip (D): 10.2mm tip

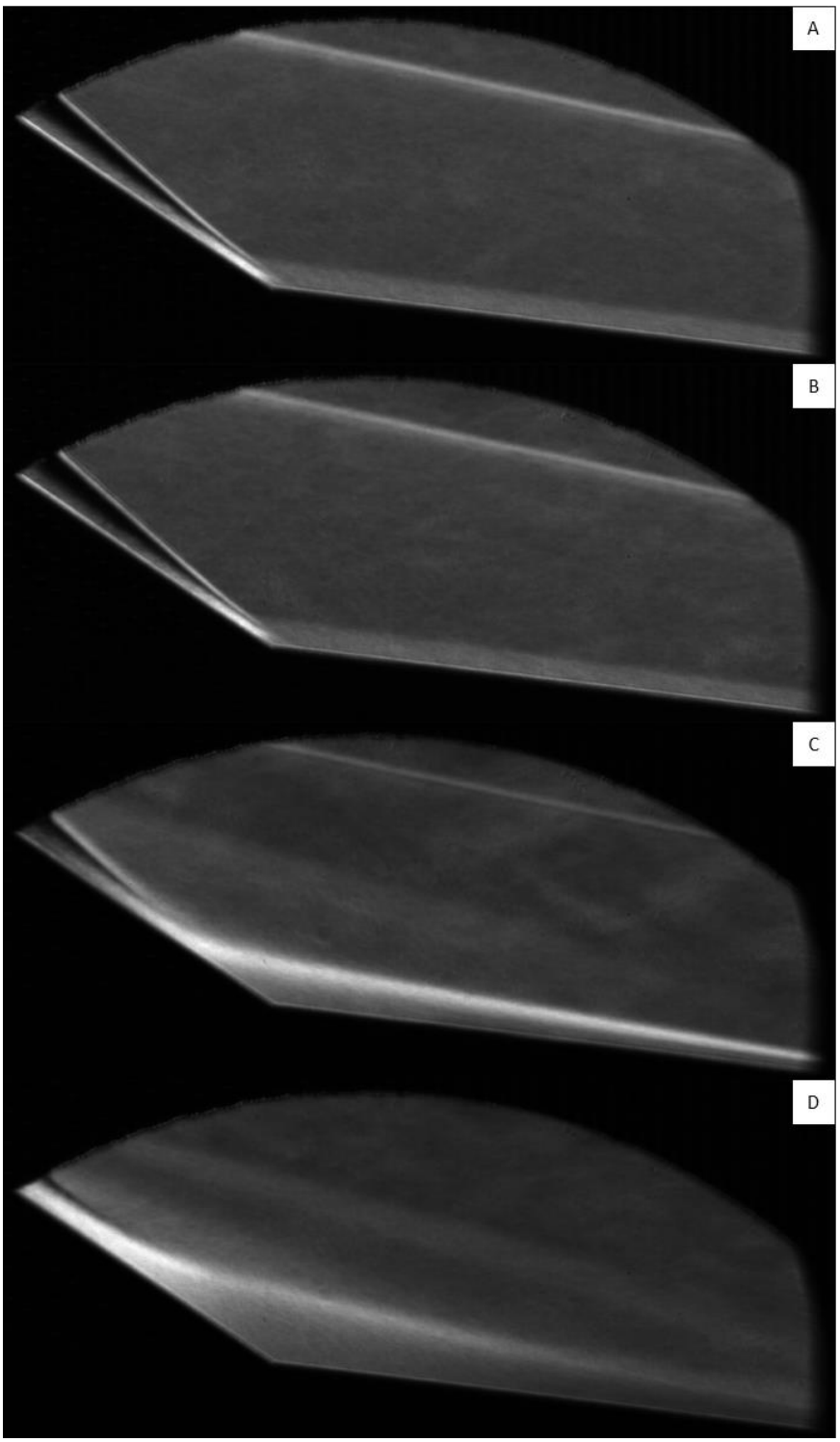

Figure 51. 34° base, 200psi (standard deviation)

(A): sharp tip (B): 0.5mm tip (C): 5.1mm tip (D): 10.2mm tip

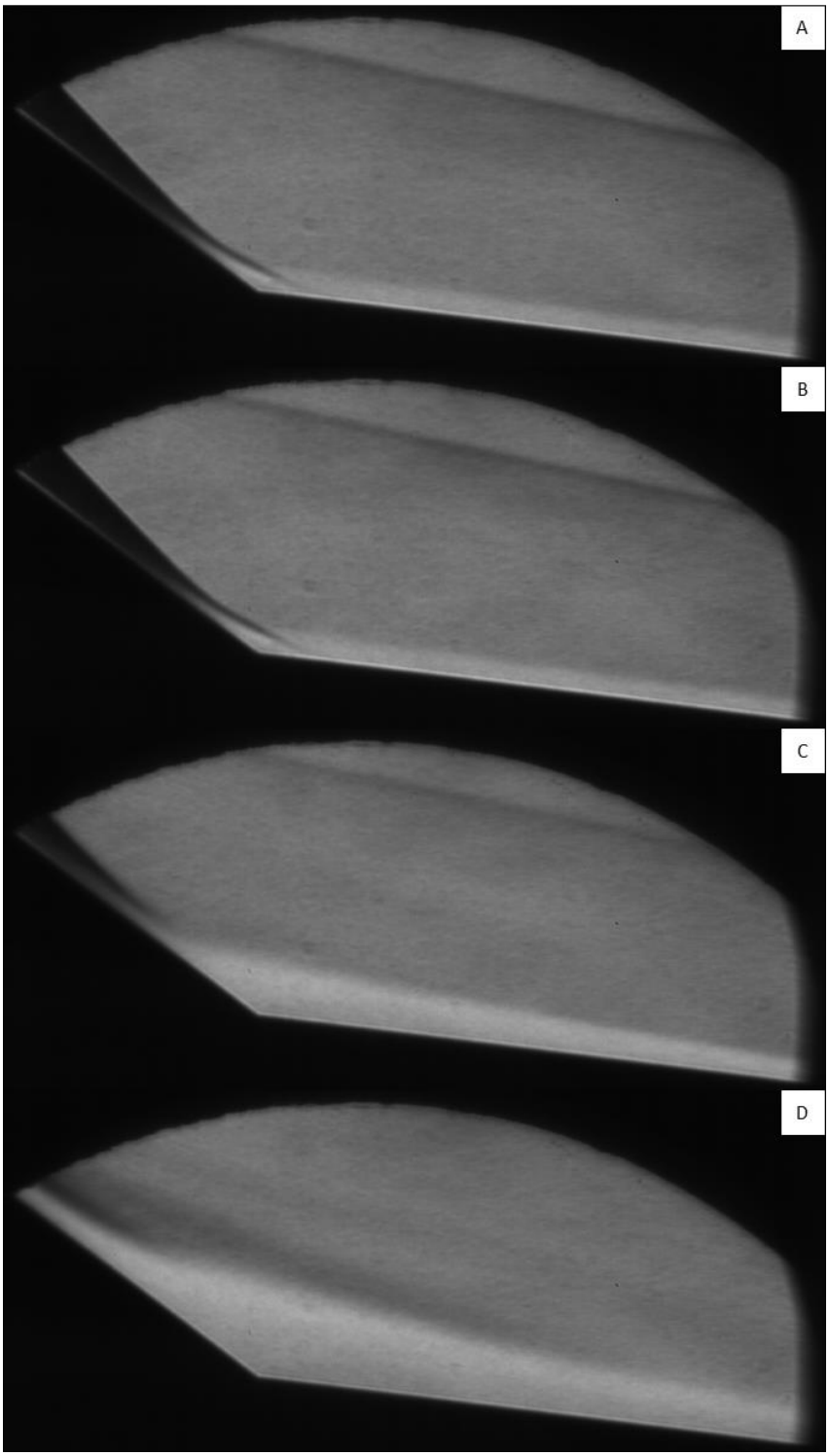

Figure 52. 37° base, 200psi (averaged)

(A): sharp tip (B): 0.5mm tip (C): 5.1mm tip (D): 10.2mm tip

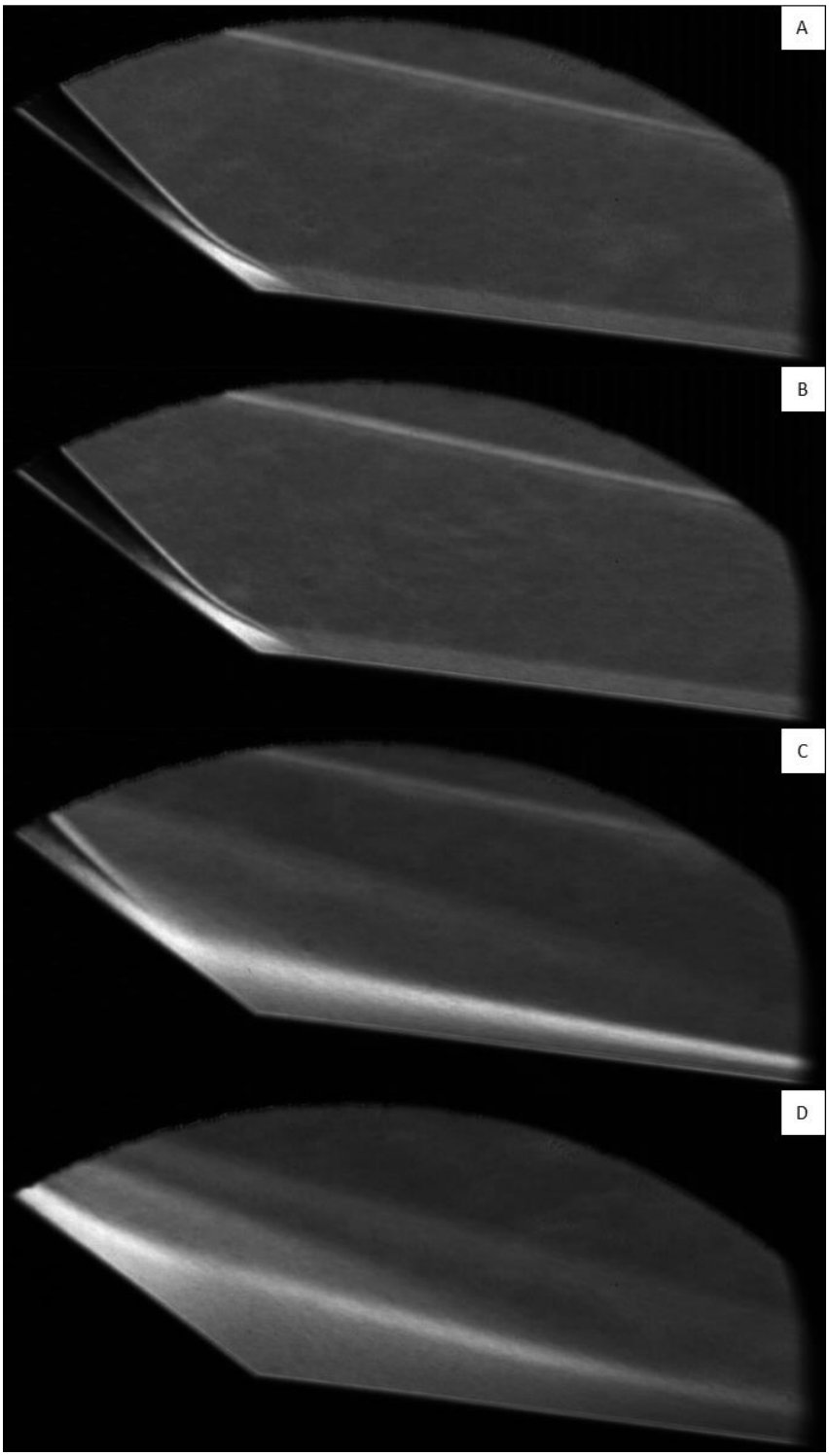

Figure 53. 37° base, 200psi (standard deviation)

(A): sharp tip (B): 0.5mm tip (C): 5.1mm tip (D): 10.2mm tip

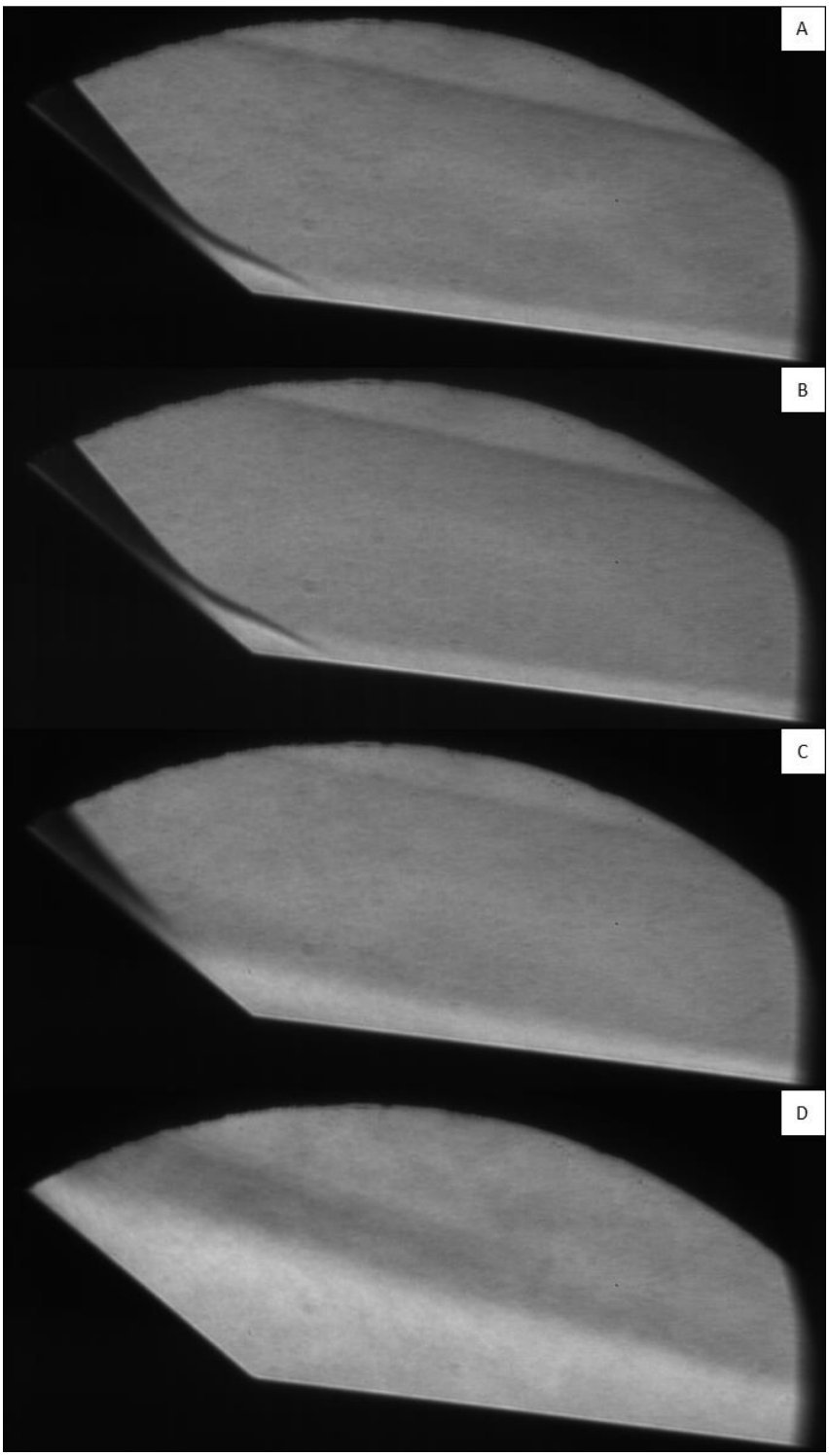

Figure 54. 40° base, 200psi (averaged)

(A): sharp tip (B): 0.5mm tip (C): 5.1mm tip (D): 10.2mm tip

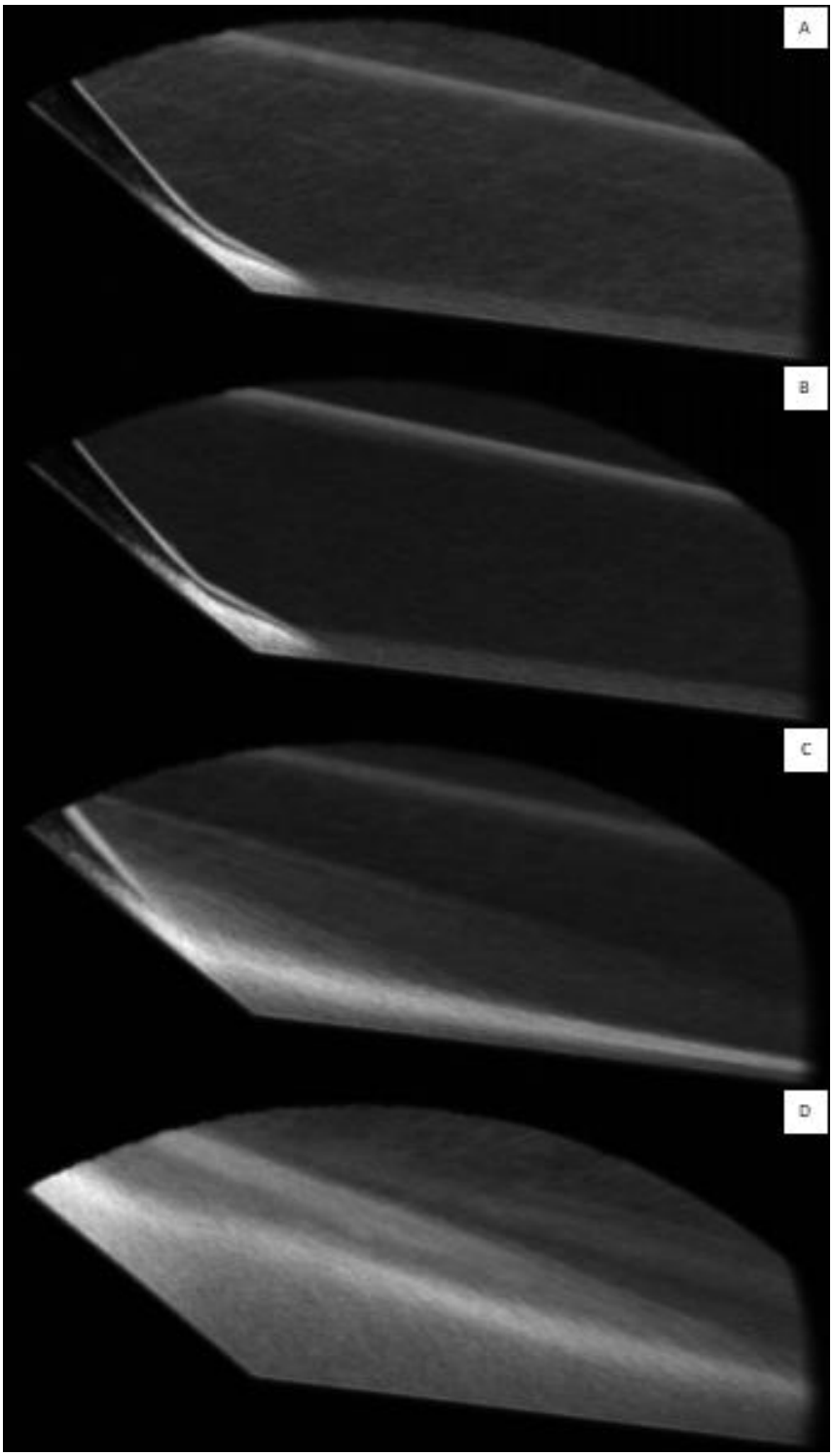

Figure 55. 40° base, 200psi (standard deviation)

(A): sharp tip (B): 0.5mm tip (C): 5.1mm tip (D): 10.2mm tip

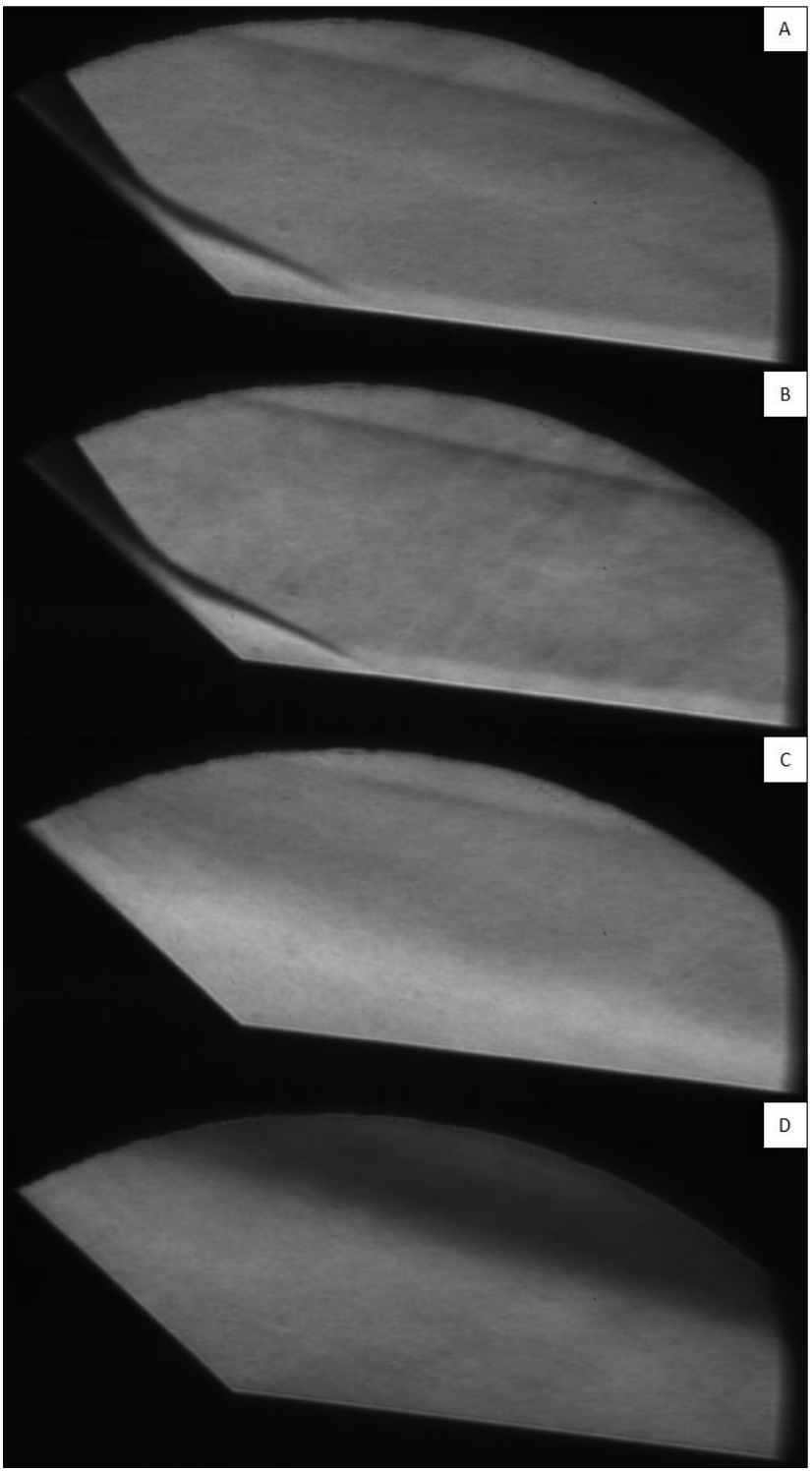

Figure 56. 43° base, 200psi (averaged)

(A): sharp tip (B): 0.5mm tip (C): 5.1mm tip (D): 10.2mm tip

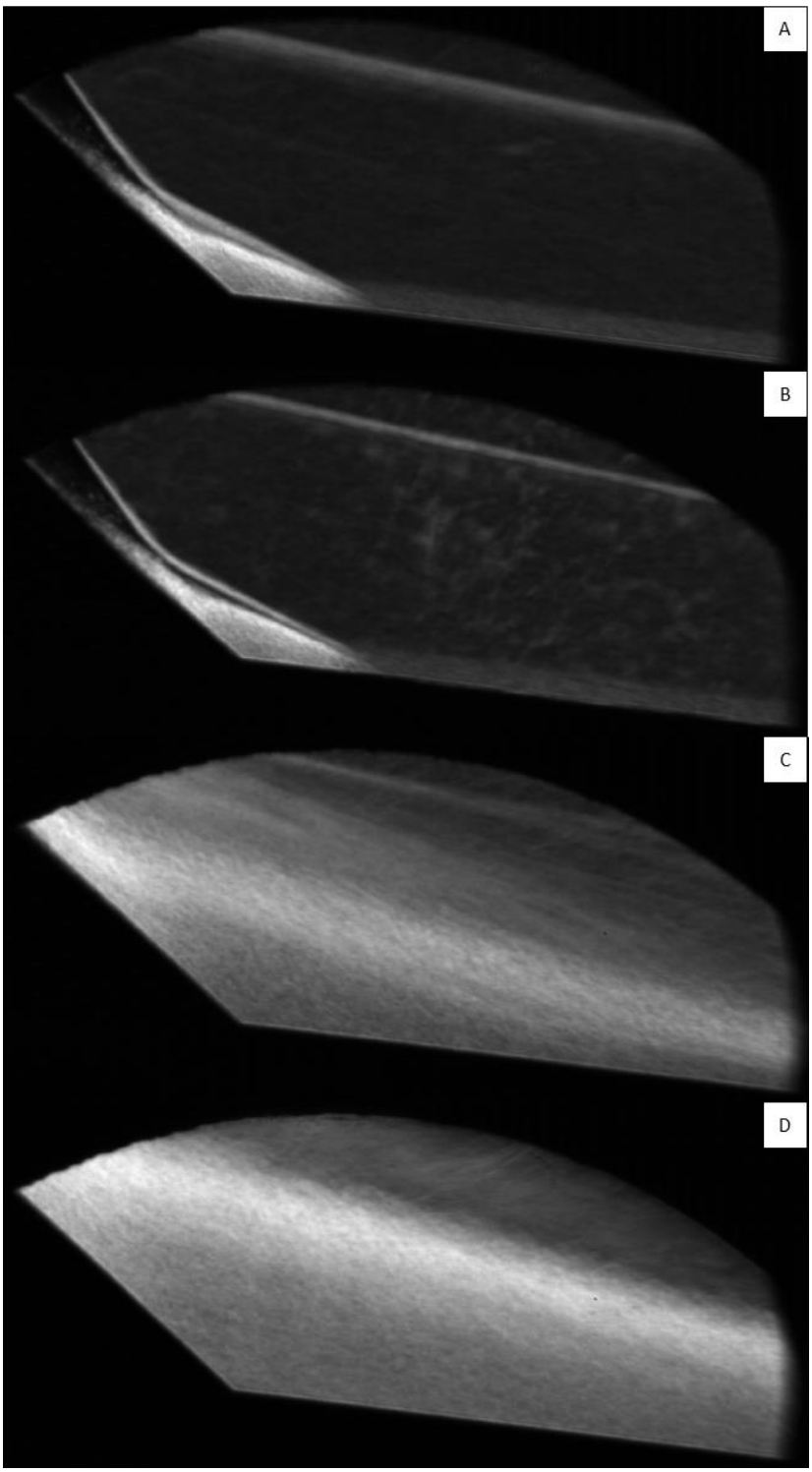

Figure 57. 43° base, 200psi (standard deviation)

(A): sharp tip (B): 0.5mm tip (C): 5.1mm tip (D): 10.2mm tip

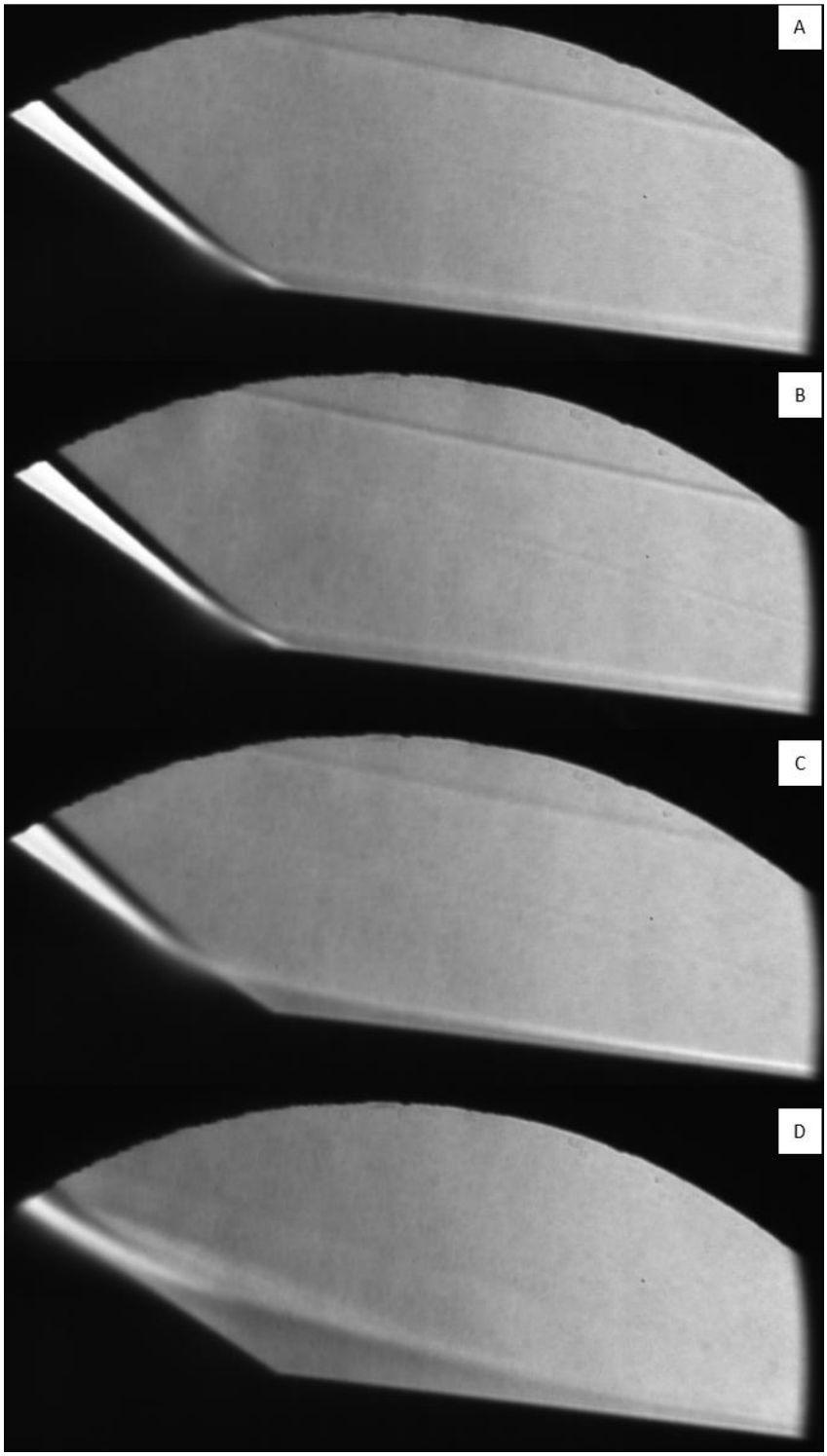

Figure 58. 34° base, 400psi (averaged), horizontal knife edge
(A): sharp tip (B): 0.5mm tip (C): 5.1mm tip (D): 10.2mm tip

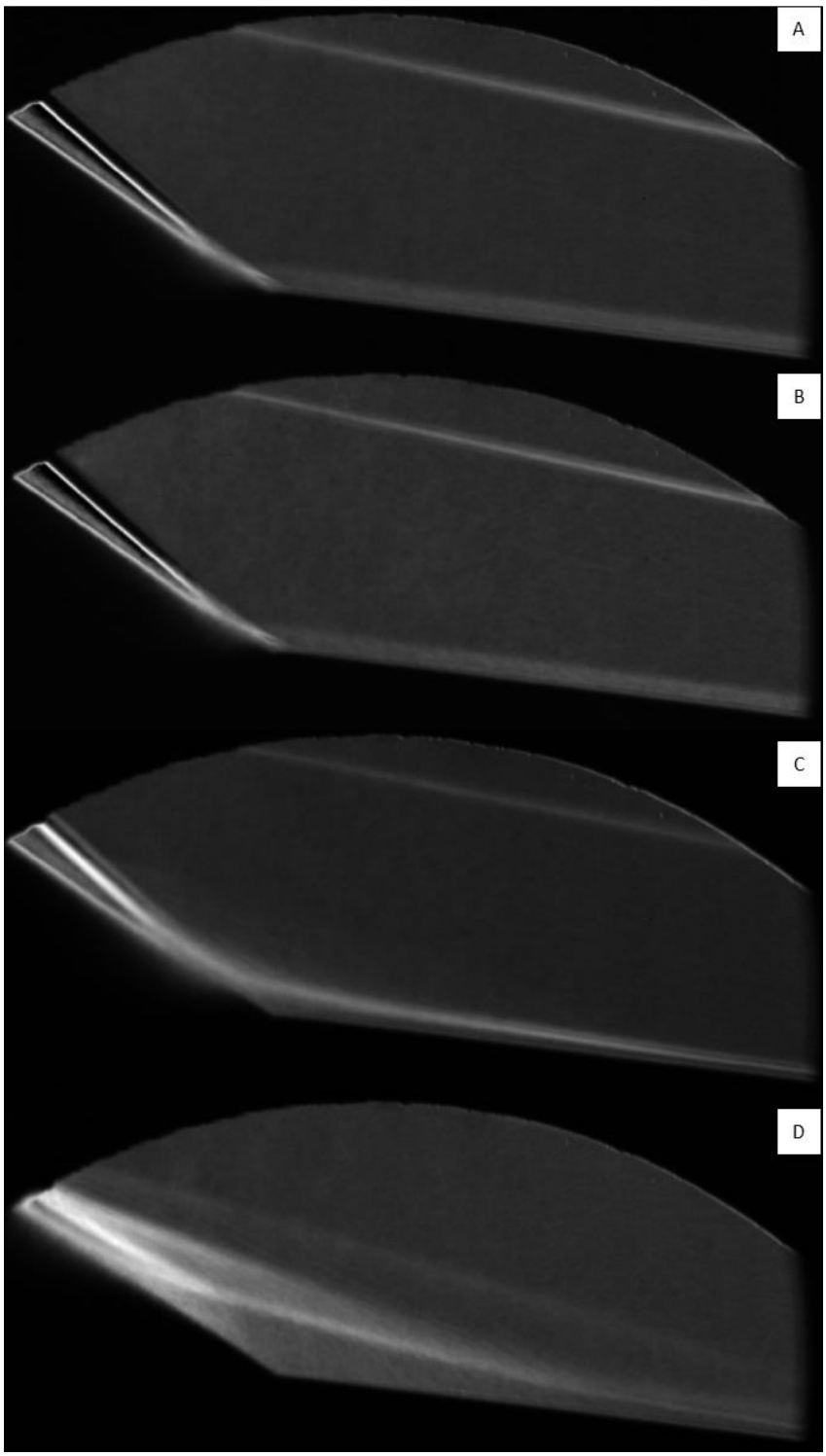

Figure 59. 34° base, 400psi (standard deviation), horizontal knife edge
(A): sharp tip (B): 0.5mm tip (C): 5.1mm tip (D): 10.2mm tip

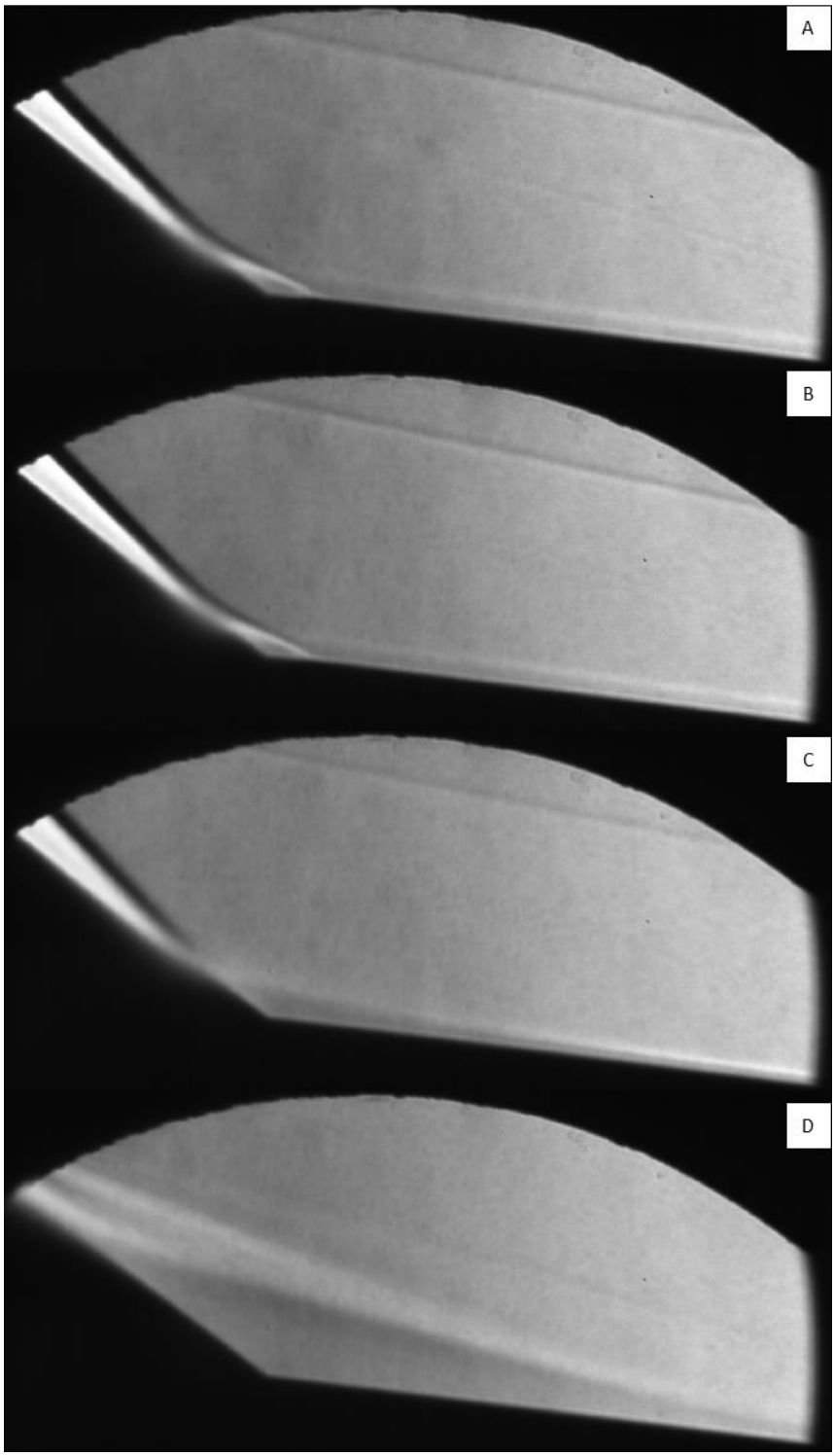

Figure 60. 37° base, 400psi (averaged), horizontal knife edge
(A): sharp tip (B): 0.5mm tip (C): 5.1mm tip (D): 10.2mm tip

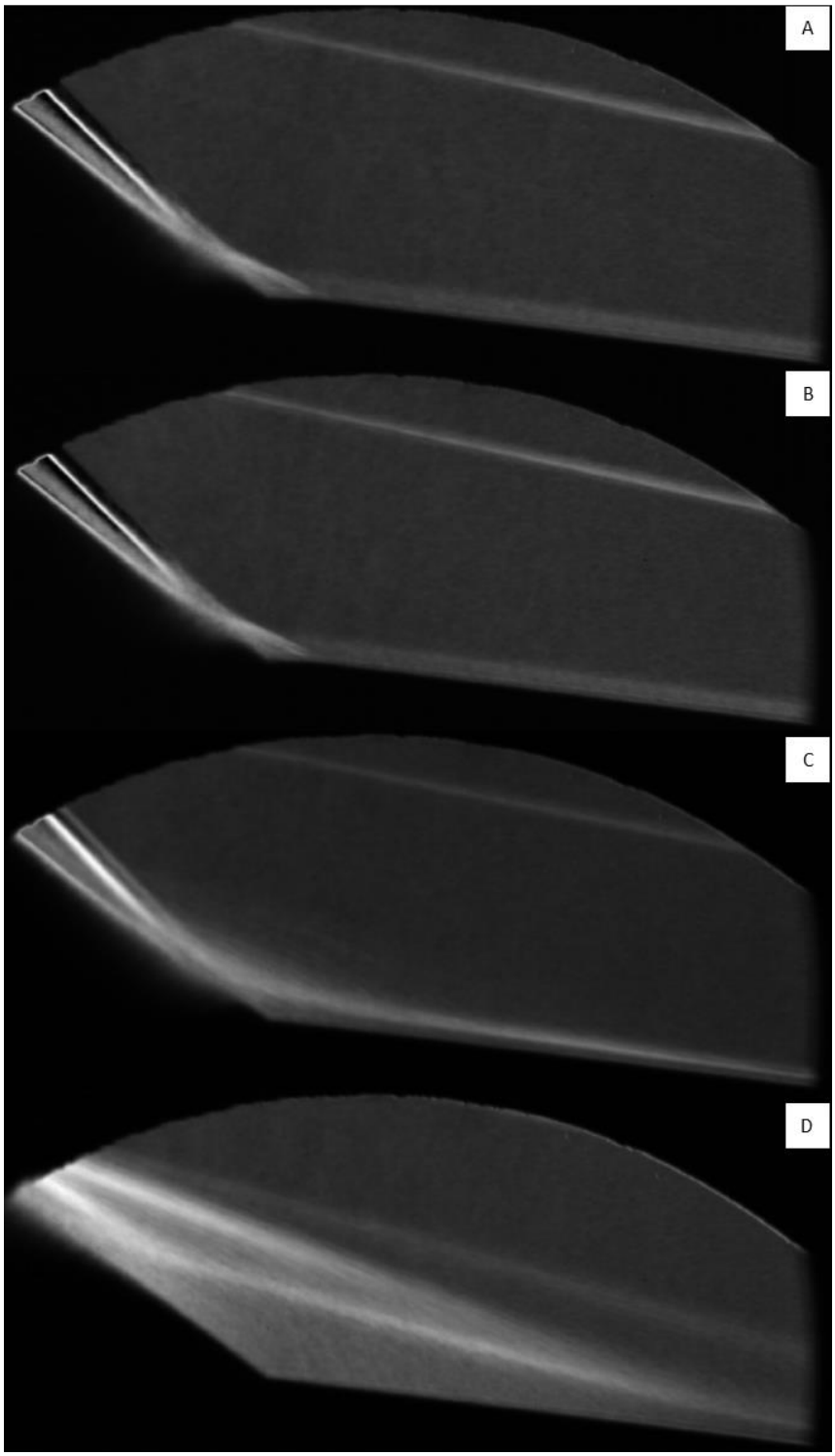

Figure 61. 37° base, 400psi (standard deviation), horizontal knife edge
(A): sharp tip (B): 0.5mm tip (C): 5.1mm tip (D): 10.2mm tip

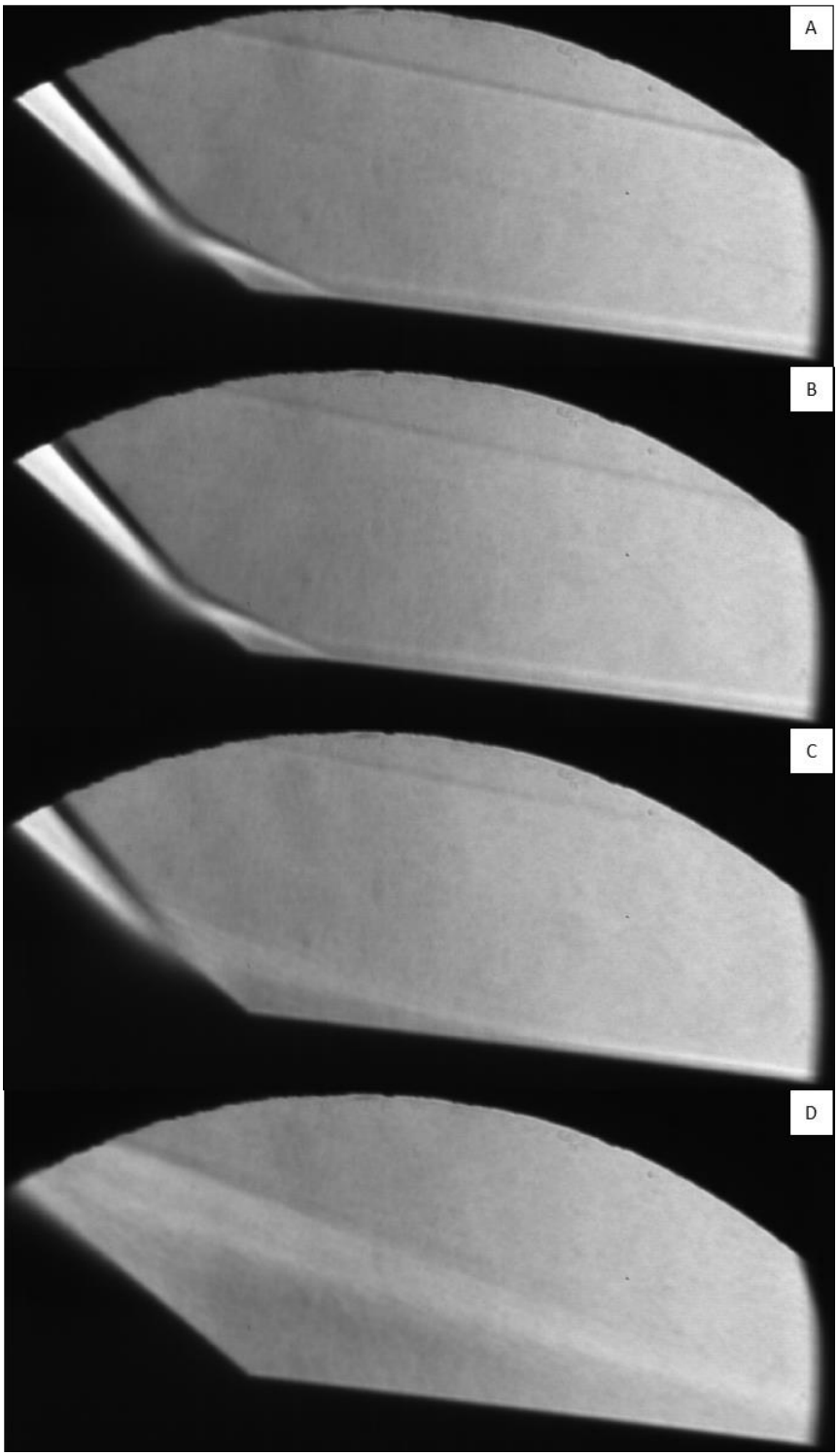

Figure 62. 40° base, 400psi (averaged), horizontal knife edge
(A): sharp tip (B): 0.5mm tip (C): 5.1mm tip (D): 10.2mm tip

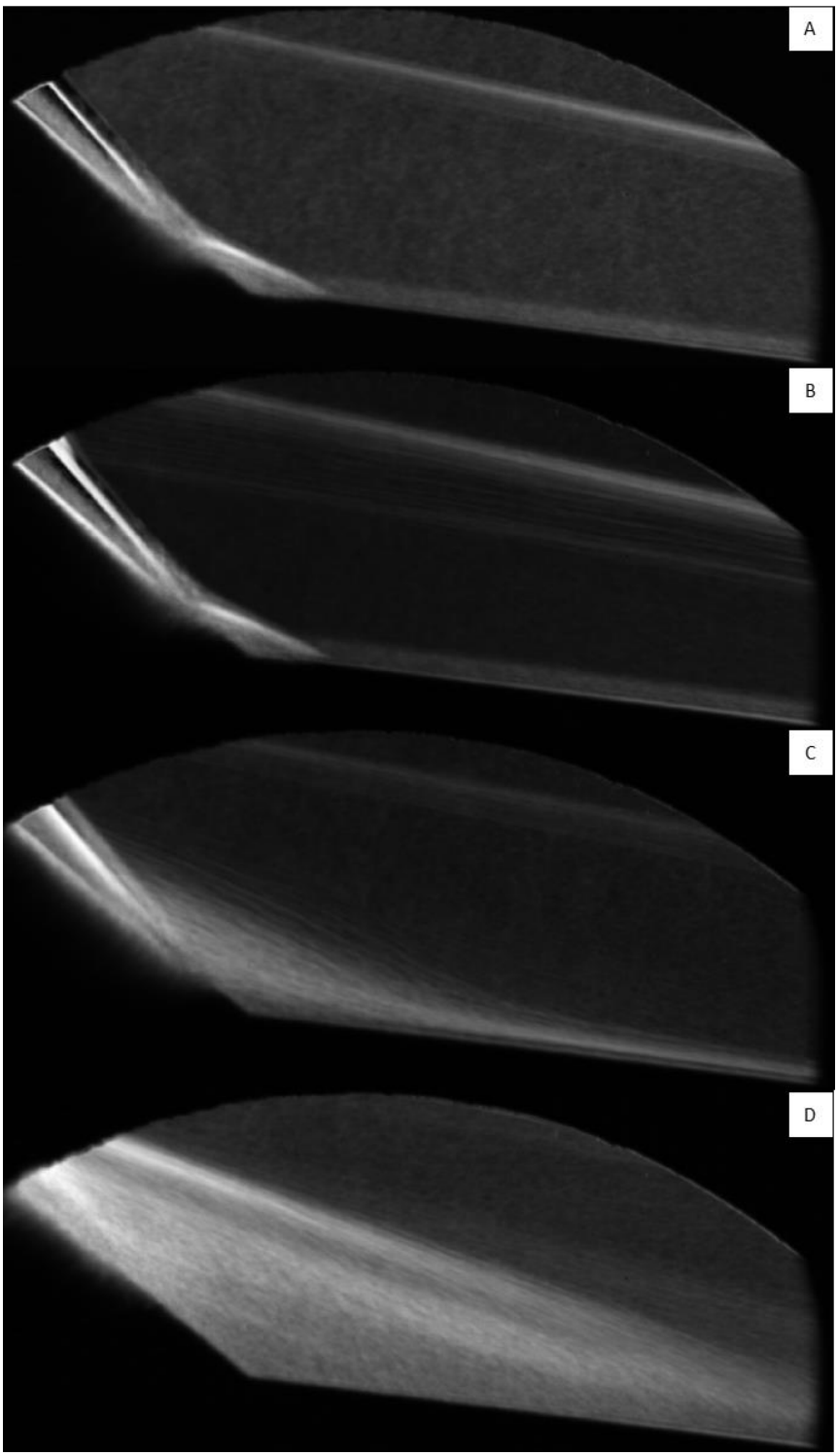

Figure 63. 40° base, 400psi (standard deviation), horizontal knife edge
(A): sharp tip (B): 0.5mm tip (C): 5.1mm tip (D): 10.2mm tip

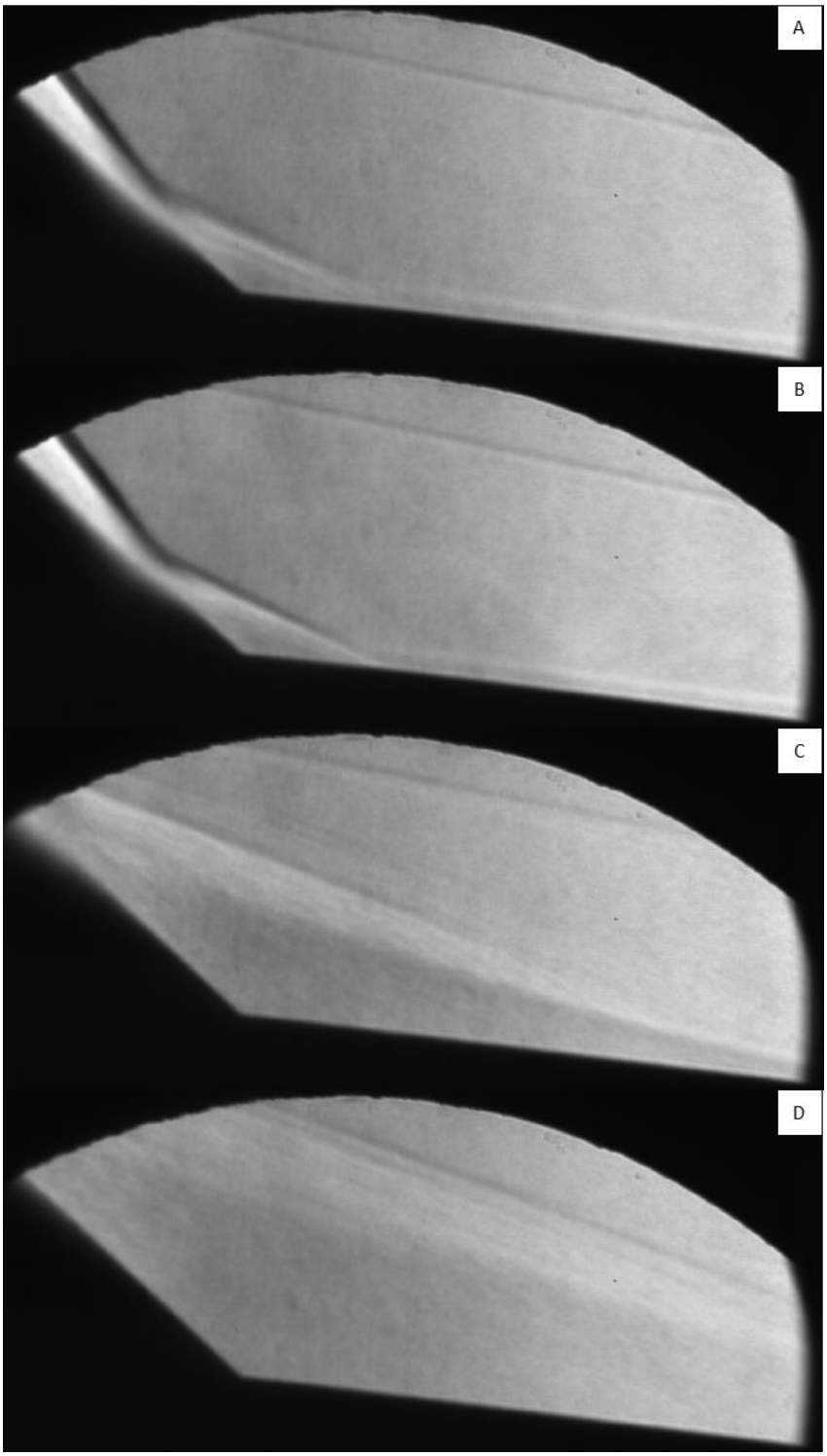

Figure 64. 43° base, 400psi (averaged), horizontal knife edge
(A): sharp tip (B): 0.5mm tip (C): 5.1mm tip (D): 10.2mm tip

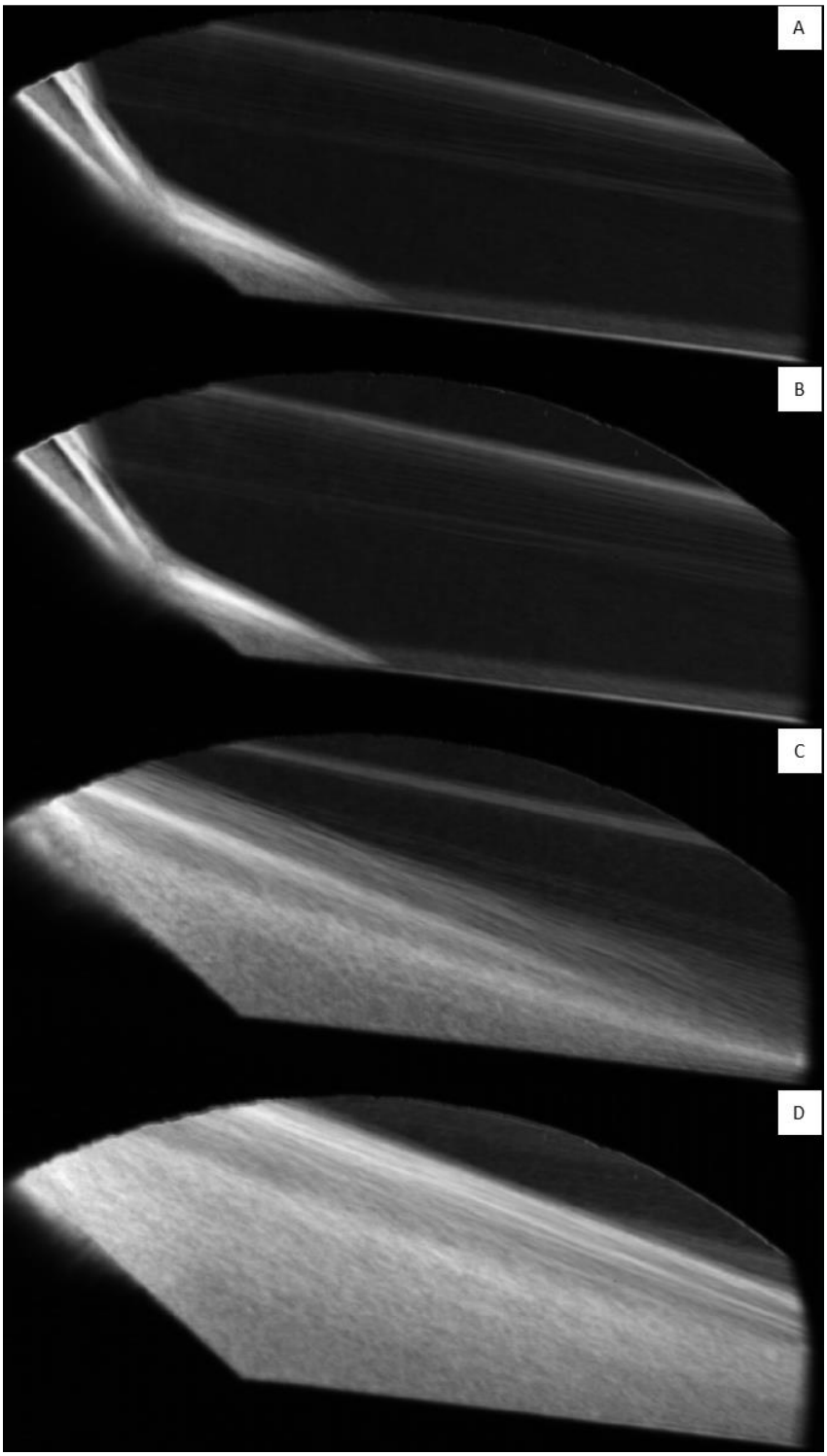

Figure 65. 43° base, 400psi (standard deviation), horizontal knife edge
(A): sharp tip (B): 0.5mm tip (C): 5.1mm tip (D): 10.2mm tip

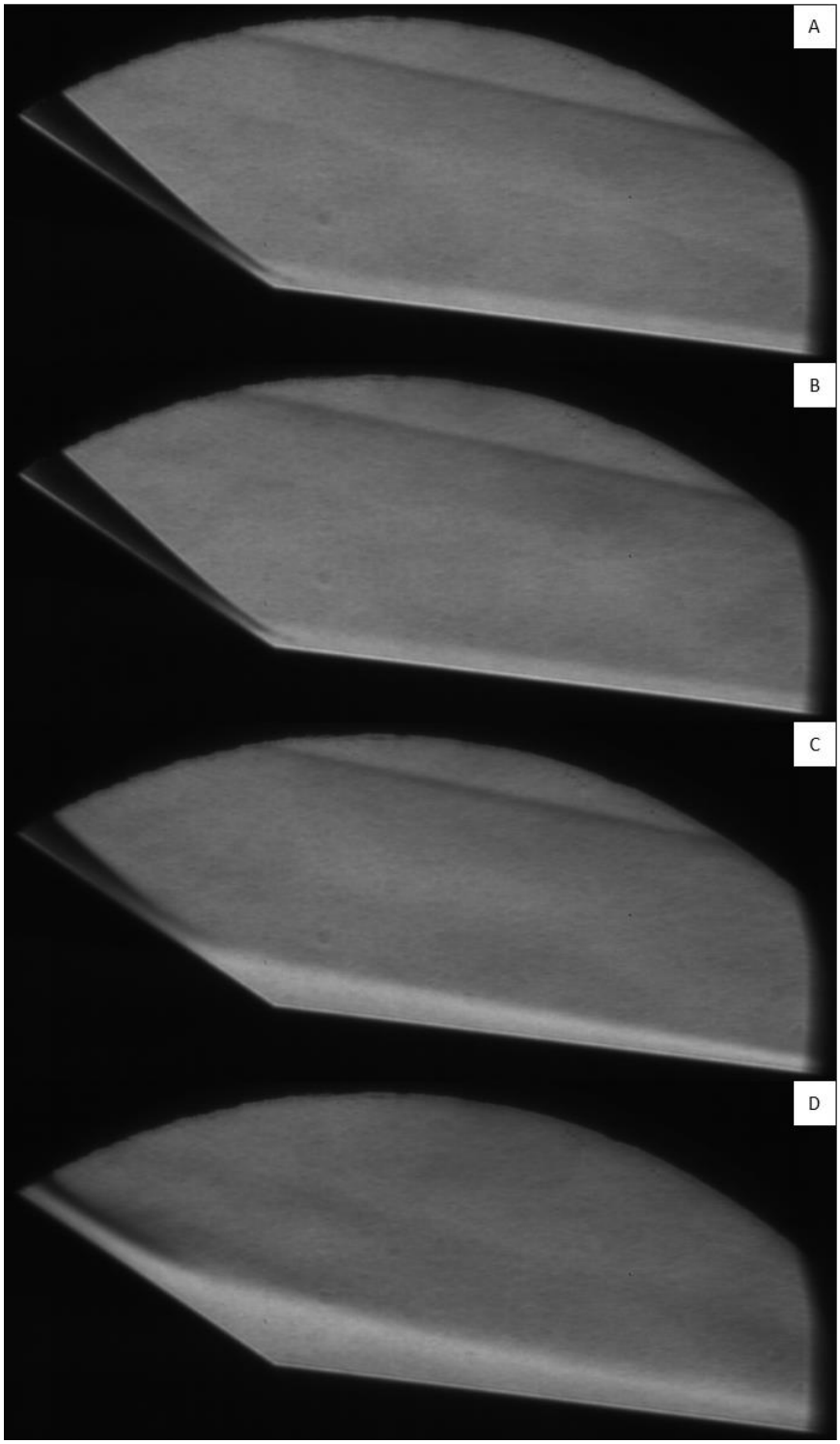

Figure 66. 34° base, 200psi (averaged), horizontal knife edge
(A): sharp tip (B): 0.5mm tip (C): 5.1mm tip (D): 10.2mm tip

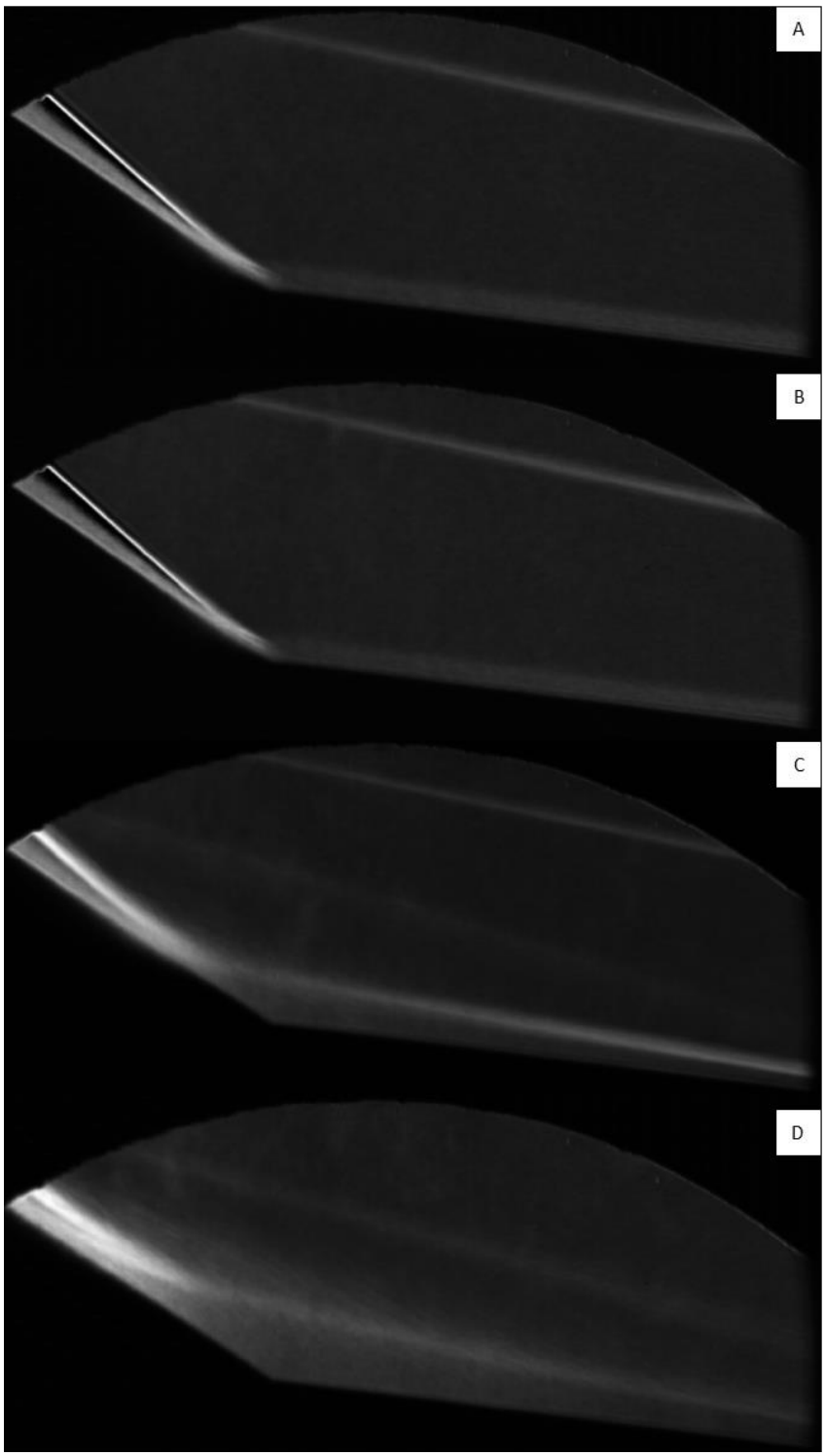

Figure 67. 34° base, 200psi (standard deviation), horizontal knife edge
(A): sharp tip (B): 0.5mm tip (C): 5.1mm tip (D): 10.2mm tip

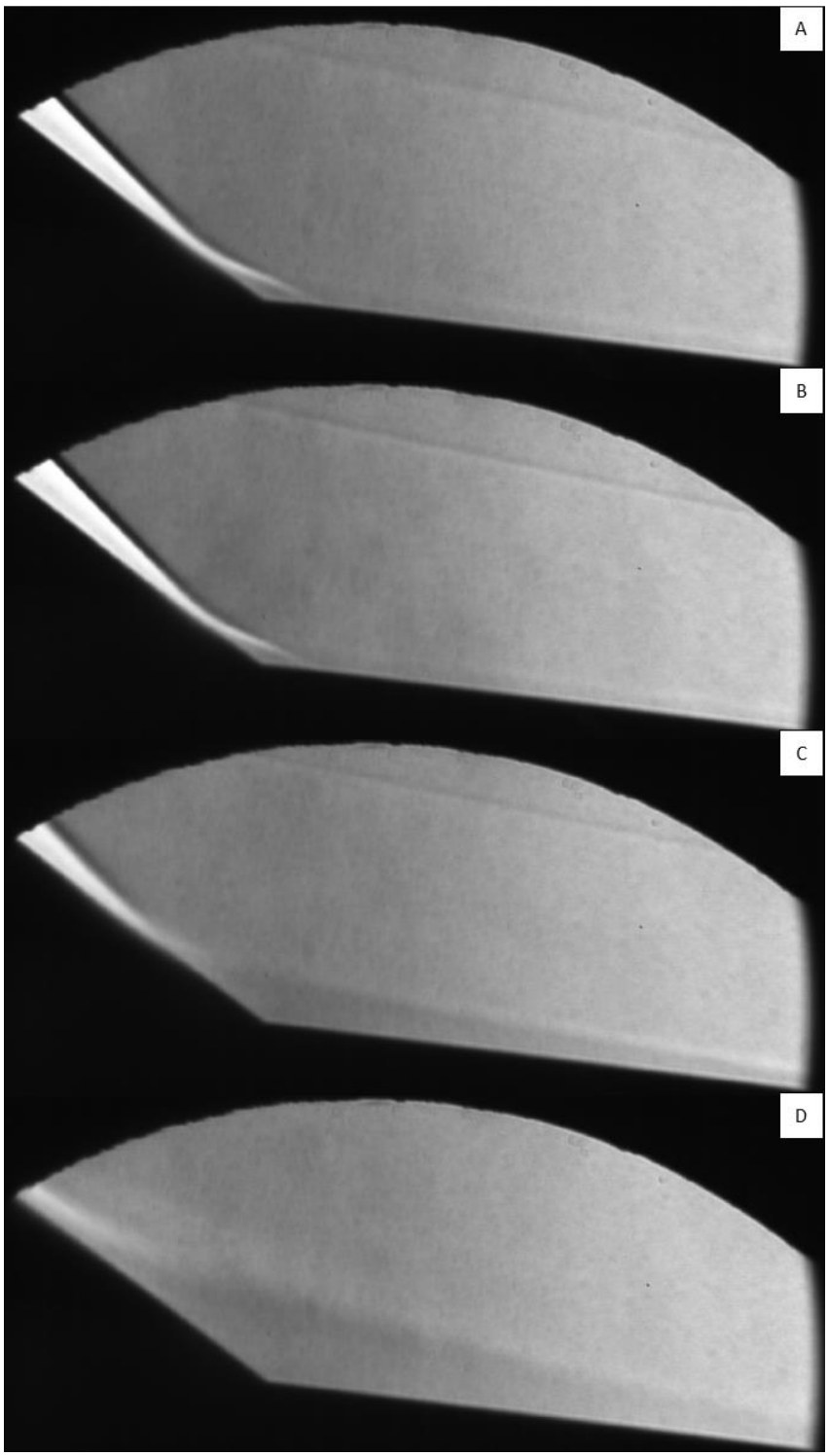

Figure 68. 37° base, 200psi (averaged), horizontal knife edge
(A): sharp tip (B): 0.5mm tip (C): 5.1mm tip (D): 10.2mm tip

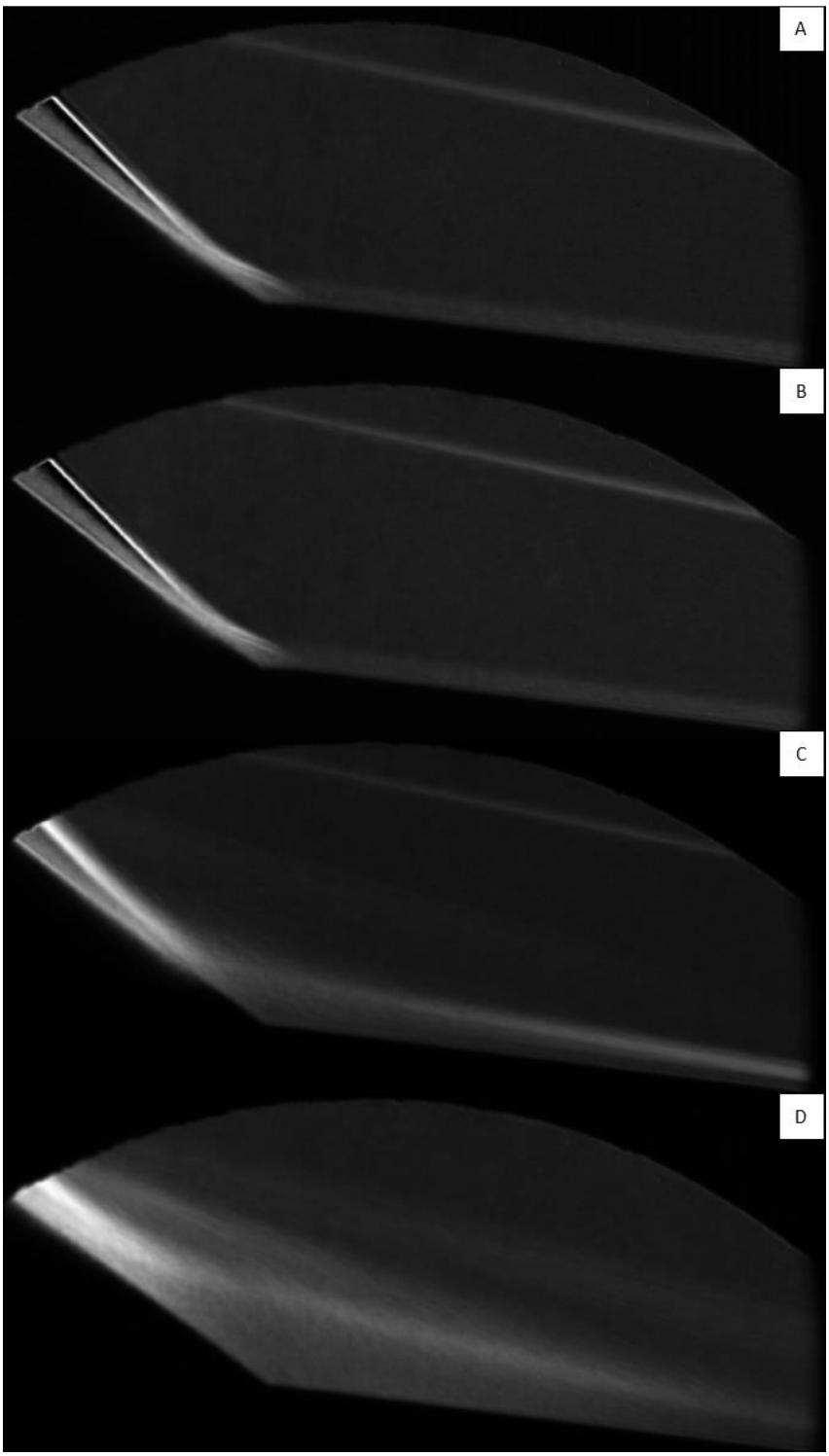

Figure 69. 37° base, 200psi (standard deviation), horizontal knife edge
(A): sharp tip (B): 0.5mm tip (C): 5.1mm tip (D): 10.2mm tip

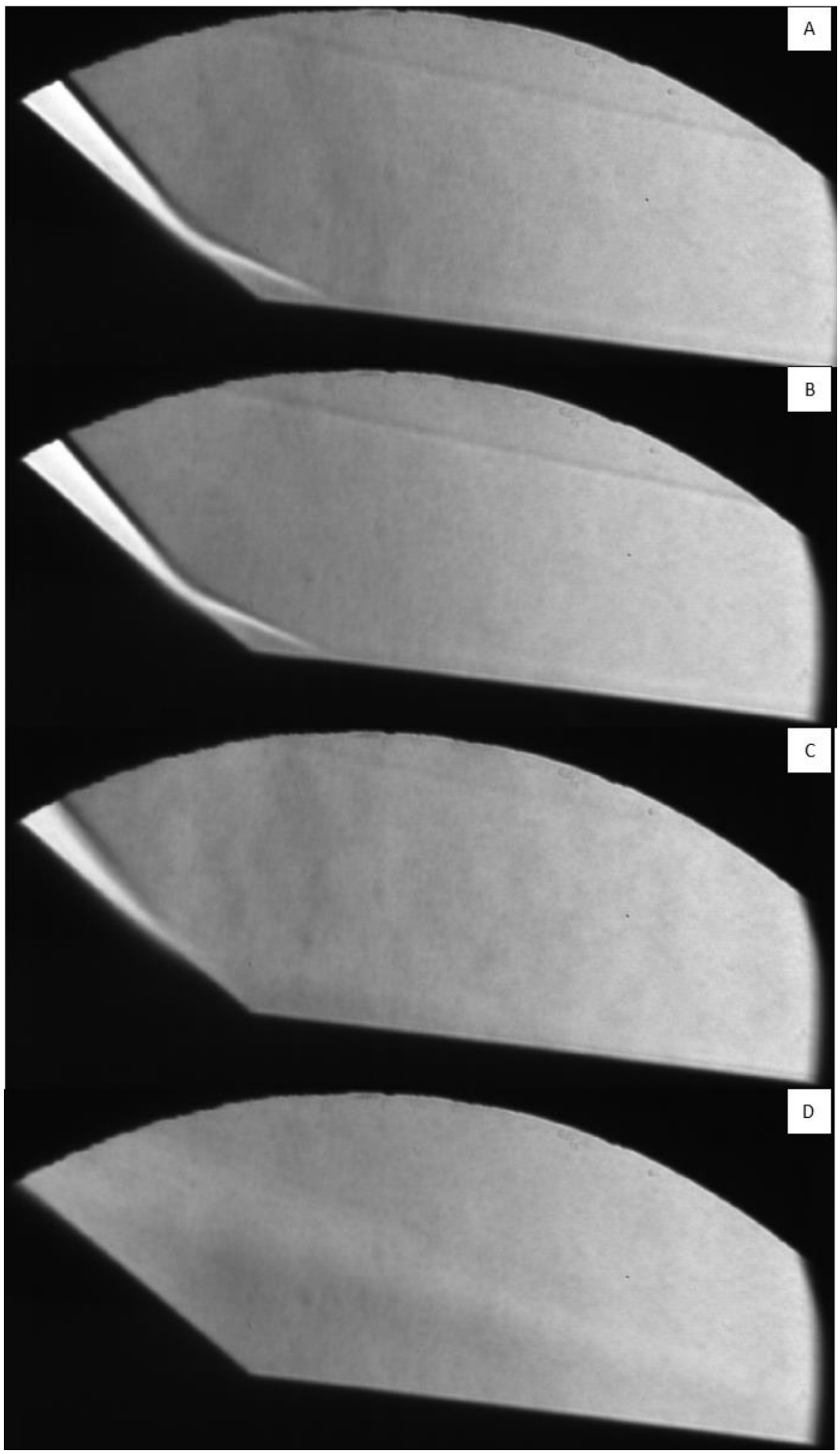

Figure 70. 40° base, 200psi (averaged), horizontal knife edge
(A): sharp tip (B): 0.5mm tip (C): 5.1mm tip (D): 10.2mm tip

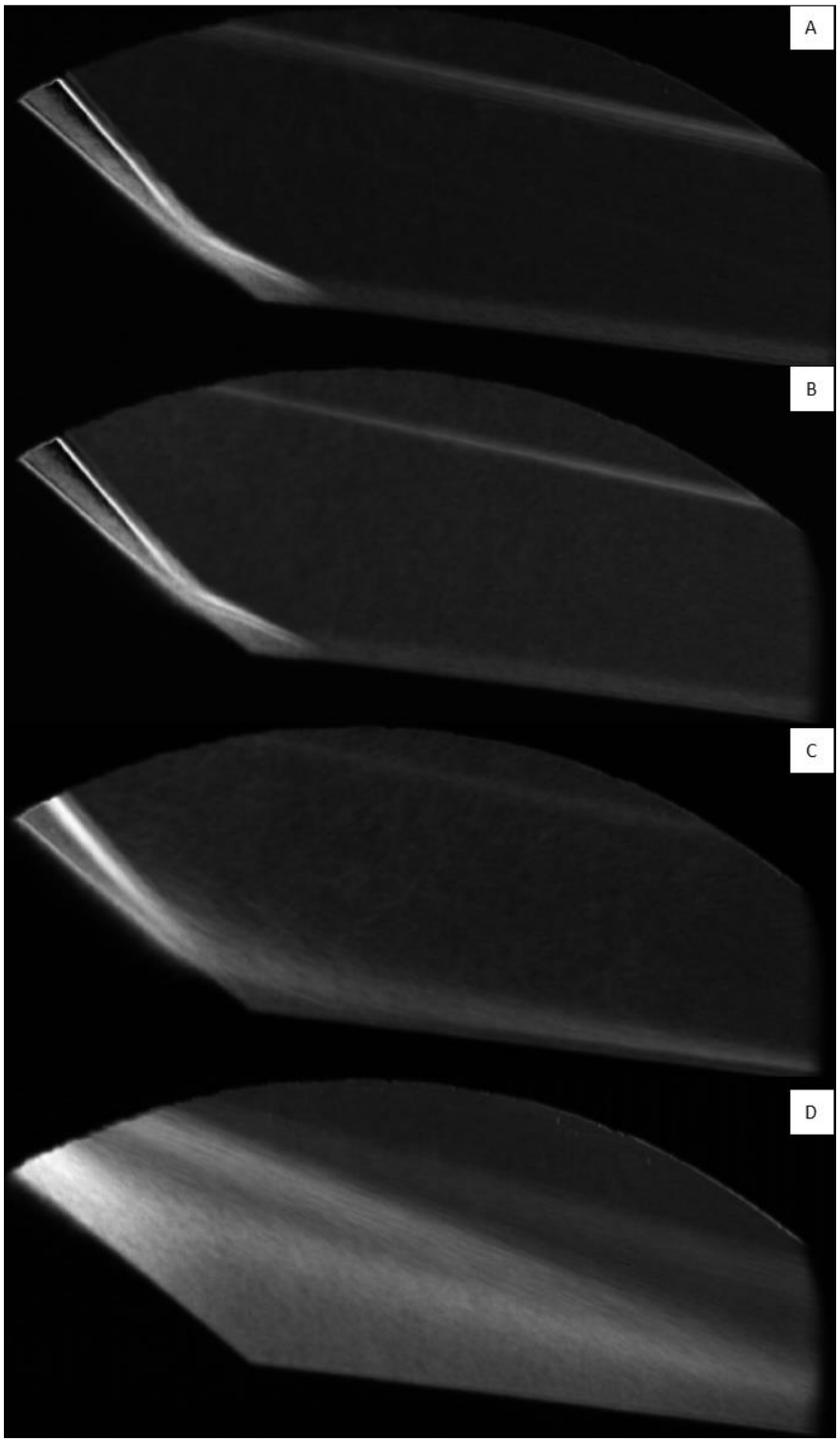

Figure 71. 40° base, 200psi (standard deviation), horizontal knife edge
(A): sharp tip (B): 0.5mm tip (C): 5.1mm tip (D): 10.2mm tip

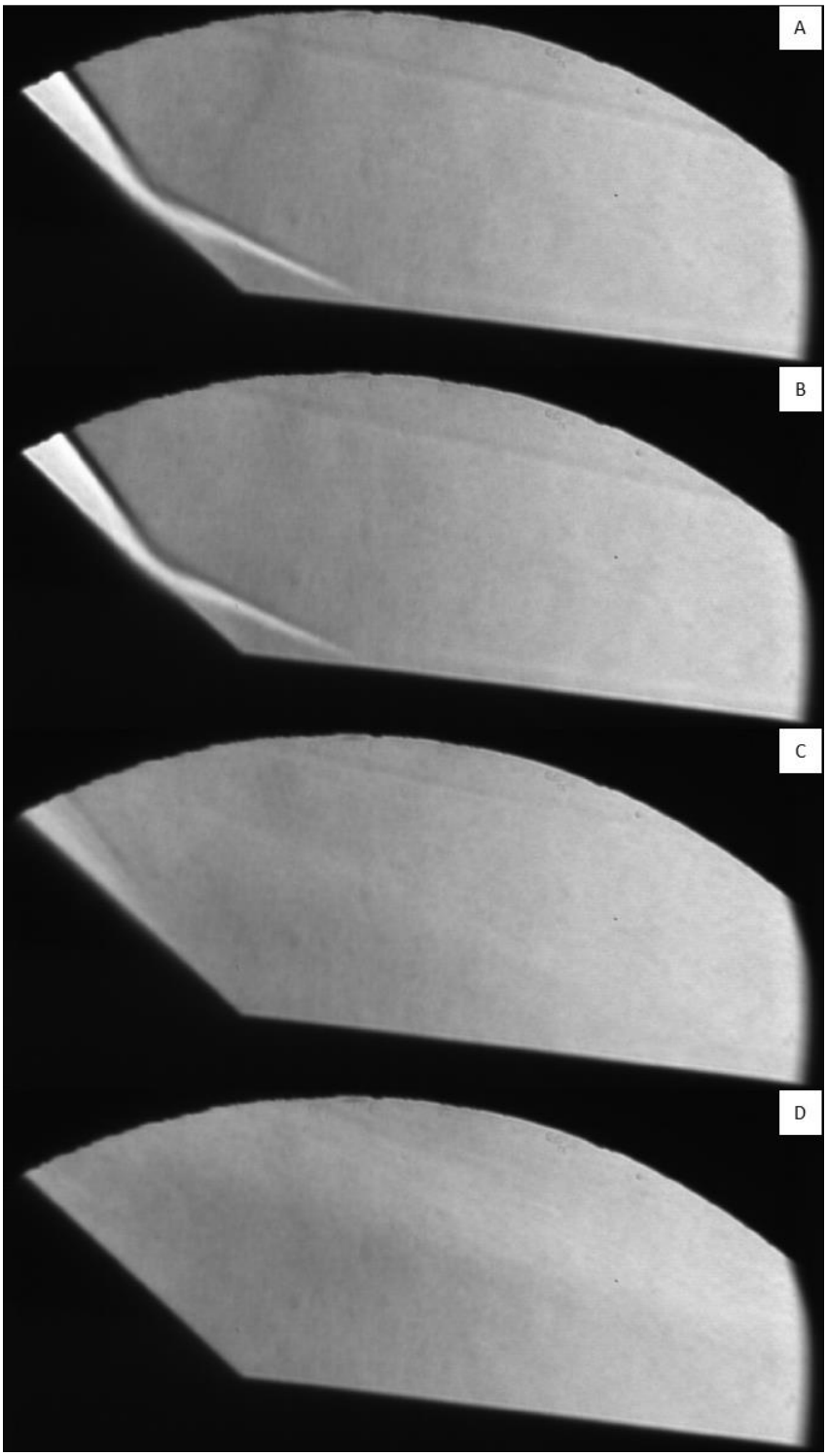

Figure 72. 43° base, 200psi (averaged), horizontal knife edge
(A): sharp tip (B): 0.5mm tip (C): 5.1mm tip (D): 10.2mm tip

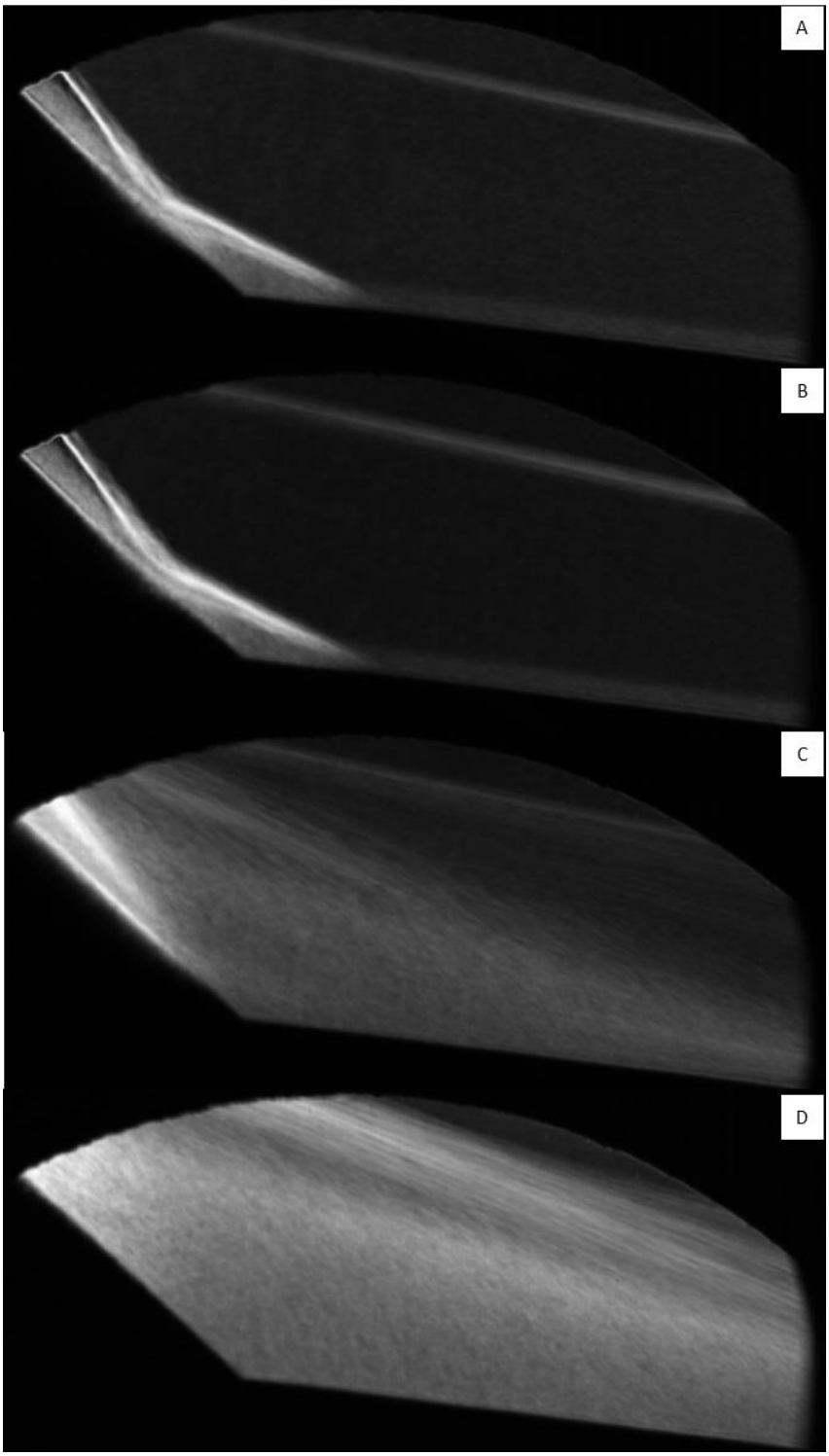

Figure 73. 43° base, 200psi (standard deviation), horizontal knife edge
(A): sharp tip (B): 0.5mm tip (C): 5.1mm tip (D): 10.2mm tip

Bibliography

[1] A. Mehta, "Hypersonics 'highest technical priority' for Pentagon R&D head," DefenseNews, 6 Mar 2018. [Online]. Available: https://www.defensenews.com/pentagon/2018/03/06/hypersonics-highest-technical-priority-for-pentagon-rd-head/.

[2] J. Anderson, Hypersonic and High-Temperature Gas Dynamics, Reston, VA: American Institute of Aeronautics and Astronautics, 2006.

[3] Boeing, "X-15 Research Aircraft," [Online]. Available: https://www.boeing.com/history/products/x-15-research-aircraft.page.

[4] T. Benson, "Scramjet Propulsion," NASA Glenn Research Center, 12 Jun 2014. [Online]. Available: https://www.grc.nasa.gov/www/BGH/scramjet.html.

[5] J. Mattingly and K. Boyer, Elements of Propulsion: Gas Turbines and Rockets, Reston, VA: American Institute of Aeronautics and Astronautics, 2016.

[6] J. Bertin and R. Cummings, "Critical Hypersonic Aerothermodynamic Phenomena," *Annual Review of Fluid Mechanics,* vol. 38, pp. 129-157, 2006.

[7] D. Dolling, "Fifty Years of Shock-Wave/Boundary-Layer Interaction Research: What Next?," *AIAA Journal,* vol. 39, no. 8, 2001.

[8] L. Mack, "Boundary Layer Stability Theory," *Report 709, Special Course on Stability and Transition of Laminar Flow,* pp. 1-81, 1984.

[9] C. Moraru, "Hypersonic Boundary-Layer Transition Measurements at Mach 10 on a Large Seven-Degree Cone at Angle of Attack," Purdue University, West Lafayette, Indiana, 2015.

[10] C. Hader and H. Fasel, "Laminar-Turbulent Transition on a Flared Cone at Mach 6," 46th AIAA Fluid Dynamics Conference, AIAA AVIATION Forum, Washington, D.C., 2016.

[11] P. Nachtsheim and H. Larson, "Crosshatched Ablation Patterns in Teflon," *AIAA Journal*, vol. 9, no. 8, 1971.

[12] R. Brun, "Shock Tubes and Shock Tunnels: Design and Experiments," AIX-MARSEILLE UNIVERSITY, France, 2009.

[13] E. Venere, "'Quiet' Mach 6 wind tunnel at Purdue helps shape future aircraft," Purdue University, 5 Jan 2006. [Online]. Available: https://news.uns.purdue.edu/html4ever/2006/060105.Schneider.tunnel.html.

[14] N. Hall, "Schlieren System," NASA, 5 May 2015. [Online]. Available: https://www.grc.nasa.gov/www/k-12/airplane/tunvschlrn.html.

[15] K. Stetson, E. Thompson, J. Donaldson and L. Siler, "Laminar Boundary Layer Stability Experiments on a Cone at Mach 8," 16th Fluid and Plasmadynamics Conference, Danvers, MA, 1983.

[16] R. Wilson, "Laminar and Turbulent Boundary Layers on Slightly-Blunted Cones at Hypersonic Speeds," *Journal of Spacecraft and Rockets*, vol. 2, no. 4, pp. 490-496, 1965.

[17] C. Zhang, Q. Tang and C. Lee, "Hypersonic Boundary-Layer Transistion on a Flared Cone," Acta Mechanica Sinica, 2013.

[18] F. Li, M. Choudhari, C. Chang and J. White, "Secondary Instability of Second Mode Disturbances in Hypersonic Boundary Layers," NASA Langley Research Center, Hampton, VA, 2012.

[19] M. Holden, T. Wadhams, M. MacLean and A. Dufrene, "Measurements in Regions of Shock Wave/Turbulent Boundary Layer Interaction from Mach 3 to 10 for Open and "Blind" Code Evaluation/Validation," CUBRC, Inc., Buffalo, NY, 2013.

[20] M. Borg and R. Kimmel, "Measurements of Crossflow Instability Modes for HIFiRE-5 at Angle of Attack," 55th AIAA Aerospace Sciences Meeting, AIAA SciTech Forum, Grapevine, TX, 2017.

[21] J. Jewell, C. Huffman and T. Juliano, "Transient Startup Simulations for a Large Mach 6 Quiet Ludwieg Tube," 55th AIAA Aerospace Sciences Meeting, AIAA SciTech Forum, Grapevine, TX, 2017.

[22] R. Kimmel, C. Carter, J. Pickles, V. Narayanaswamy and K. Lam, "High-Speed Schlieren and 10-Hz KR PLIF for the New AFRL Mach 6 Ludwieg Tube Hypersonic Wind Tunnel," Air Force Research Laboratory Aerospace Systems Directorate, Wright-Patterson AFB, OH, 2017.

[23] C. Running, T. Juliano, J. Jewell, M. Borg and R. Kimmel, "Hypersonic Shock-Wave/Boundary-Layer Interactions on a Cone/Flare Model," 2018 Fluid Dynamics Concerence, AIAA AVIATION Forum, Atlanta, GA, 2018.

[24] R. Kimmel, M. Borg, J. Jewell, K. Lam, R. Bowersox, R. Srinivasan, S. Fuchs and T. Mooney, "AFRL Ludwieg Tube Initial Performance," in *AIAA SciTech Forum*, Grapevine, TX, 2017.

[25] J. Huwaldt, "Supersonic Cone version 1.2.2," 11 Jan 2015. [Online]. Available: http://thehuwaldtfamily.org/java/Applications/SupersonicCone/index.html.

[26] J. Anderson, Fundamentals of Aerodynamics, Sixth Edition, New York, NY: McGraw-Hill, 2017, pp. 864-866.

[27] D. M. M. Dolling, "Unsteadiness of the Separation Shock Wave Structure in a Supersonic Compression Ramp Flowfield," *AIAA Journal*, vol. 21, no. 12, pp. 1628-1634, 1983.

REPORT DOCUMENTATION PAGE

Form Approved
OMB No. 074-0188

The public reporting burden for this collection of information is estimated to average 1 hour per response, including the time for reviewing instructions, searching existing data sources, gathering and maintaining the data needed, and completing and reviewing the collection of information. Send comments regarding this burden estimate or any other aspect of the collection of information, including suggestions for reducing this burden to Department of Defense, Washington Headquarters Services, Directorate for Information Operations and Reports (0704-0188), 1215 Jefferson Davis Highway, Suite 1204, Arlington, VA 22202-4302. Respondents should be aware that notwithstanding any other provision of law, no person shall be subject to an penalty for failing to comply with a collection of information if it does not display a currently valid OMB control number.
PLEASE DO NOT RETURN YOUR FORM TO THE ABOVE ADDRESS.

1. REPORT DATE *(DD-MM-YYYY)*	2. REPORT TYPE	3. DATES COVERED *(From – To)*
08-03-2019	Master's Thesis	August 2017 – March 2019

4. TITLE AND SUBTITLE

Schlieren Imaging and Flow Analysis on a Cone/Flare Model in the AFRL Mach 6 Ludwieg Tube Facility

5a. CONTRACT NUMBER

5b. GRANT NUMBER

5c. PROGRAM ELEMENT NUMBER

6. AUTHOR(S)

LaBuda, David A., Second Lieutenant, USAF

5d. PROJECT NUMBER
JON 19Y231

5e. TASK NUMBER

5f. WORK UNIT NUMBER

7. PERFORMING ORGANIZATION NAMES(S) AND ADDRESS(S)

Air Force Institute of Technology
Graduate School of Engineering and Management (AFIT/ENY)
2950 Hobson Way, Building 640
WPAFB OH 45433-8865

8. PERFORMING ORGANIZATION REPORT NUMBER

AFIT-ENY-MS-19-M-226

9. SPONSORING/MONITORING AGENCY NAME(S) AND ADDRESS(ES)

Air Force Research Laboratory
2145 5th Street, Building 24c
Wright-Patterson AFB, OH 45433-7542
(937) 713-6697 matthew.borg.3@us.af.mil
ATTN: Matt Borg

10. SPONSOR/MONITOR'S ACRONYM(S)
AFRL/RQHF

11. SPONSOR/MONITOR'S REPORT NUMBER(S)

12. DISTRIBUTION/AVAILABILITY STATEMENT

DISTRUBTION STATEMENT A: APPROVED FOR PUBLIC RELEASE; DISTRIBUTION UNLIMITED.

13. SUPPLEMENTARY NOTES

This material is declared a work of the U.S. Government and is not subject to copyright protection in the United States.

14. ABSTRACT

High-speed Schlieren photography was utilized to visualize flow over a cone/flare model with variable geometry in the AFRL Mach 6 Ludwieg tube facility. Testing was performed at freestream Reynolds numbers of 10.0E6 and 19.8E6 per meter. The variable-angle flare portion of the model provided a method for adjusting the intensity of the adverse pressure gradient at the cone/flare junction. As expected from existing literature, boundary layer separation along the cone frustum occurred further upstream as adverse pressure gradient intensity increased. Imaging of the four cone tip radii revealed a slightly positive angle of attack for the model. This conclusion was supported by asymmetrical heating contours observed in a prior infrared thermography study on the same model. Measurements of the bow shock angles downstream of the cone tip verified Mach 6 flow from the Ludwieg tube nozzle when analyzed using Taylor-Maccoll theory. Blunt cone tips generated laminar boundary layers along the cone frustum. These laminar boundary layers led to unstable behavior in the recirculation region at the cone/flare junction. Analysis of the instability revealed loosely cyclical behavior. Future hypersonic vehicles will inevitably include numerous adverse pressure gradients. A full understanding of these regions is imperative to successful design and flight testing.

15. SUBJECT TERMS

Ludwieg Tube; Hypersonic; High-Speed Schlieren; Shock-Wave/Boundary-Layer Interaction; Cone/Flare Model; Thesis

16. SECURITY CLASSIFICATION OF:			17. LIMITATION OF ABSTRACT	18. NUMBER OF PAGES	19a. NAME OF RESPONSIBLE PERSON
a. REPORT	b. ABSTRACT	c. THIS PAGE			Dr Mark Reeder, AFIT/ENY
U	U	U	U	120	19b. TELEPHONE NUMBER (937) 255-3636, ext. 4530 (Mark.Reeder@afit.edu)

Standard Form 298 (Rev. 8-98)
Prescribed by ANSI Std. Z39-18